Topics in Energy Release and Particle Acceleration in the Heliosphere

A thesis

submitted in fulfilment

of the requirements for the Degree

of

Doctor of Philosophy

at the

University of Waikato

by

Craig Armstrong

THE UNIVERSITY OF
WAIKATO
Te Whare Wānanga o Waikato

University of Waikato

2014

Preface

This thesis was made possible by the work of various previous authors. Chapters 2 and 5 provide background for the original work in Chapters 3, 4 and 6.

Chapters 3 and 4 made use of the 2D Fortran code "MHD2D", first written by Craig and Watson (1999) and later modified by Heerikhuisen, Craig, and Watson (2000). To this code I added the Braginskii form of the viscosity which, after much grief, was found to need an Alternating Direction Implicit (ADI) solver (written by I.J.D. Craig) for the Poisson equation, in place of the original Fast Fourier Transform method. The work of Chapter 3 has been published in Armstrong, Craig, and Litvinenko (2011), and the Tang vortex results (Chapter 4) appear in Armstrong and Craig (2013) and Armstrong and Craig (2014).

The work of Chapter 6 has been published in Armstrong, Litvinenko, and Craig (2012). The Matlab code used for the numerical results in Chapters 5 and 6 was written by myself.

Matlab was used to create the figures for all of the results in this thesis. XFig was used for the illustrative diagrams. This research has made use of NASA's Astrophysics Data System (ADS).

Abstract

This thesis investigates both the release of energy in solar flares, and the acceleration and transport of particles in various astrophysical situations. While numerical simulations are central to this thesis, these are always motivated by analytical arguments.

A review of flare energy release is given in Chapter 2, with results presented in Chapters 3 and 4. The main goal of the flare work is to investigate the effect of viscosity on energy release rates. Scaling arguments and exact solutions of the magnetohydrodynamic equations are used to interpret the results of two-dimensional numerical simulations of magnetic reconnection. The results support viscous energy dissipation accounting for a significant fraction of flare energy release.

Chapter 5 contains an introduction to astrophysical particle acceleration, using the Fokker-Planck formulation. The theory introduced in this chapter is used to study electron transport in solar flare loops (Section 5.5). A key aspect of the analysis is the expression of the Fokker-Planck equation as a system of stochastic differential equations. A generalisation to the flare loop hard X-ray emission prediction of Conway *et al.* (1998) is obtained, giving a stronger dependence on density for dispersed initial distributions.

Chapter 6 uses the methods of the previous chapter to study the acceleration of cosmic-rays at the heliospheric termination shock. The applicability of the focused acceleration mechanism of Schlickeiser and Shalchi (2008) is examined using numerical simulations, which are interpreted using analytical arguments based on averaging the stochastic equations. The results show significant limitations in assuming a near-isotropic distribution, a requirement for the focused acceleration mechanism. In addition, momentum diffusion provides a significant effect that cannot be neglected. The theory is extended to include focused deceleration and pure momentum diffusion.

Acknowledgements

I wish to thank my supervisors, Professor Ian Craig and Dr Yuri Litvinenko, for their help and guidance through all stages of this thesis.

I would also like to thank the staff of the University of Waikato Mathematics Department for their assistance.

I am grateful to the University of Waikato for providing both a Doctoral Research Scholarship and the Sir Edmund Hillary Scholarship.

I would like to thank my fellow doctoral student Nina Lopez for being an amazing friend who always managed to cheer me up when I needed it.

Special thanks go to my parents, Bill and Estelle, and my brother and sister-in-law, Dean and Deborah, for their unwavering support and belief in me.

I dedicate this thesis to my niece Sophie and my nephew William. I will walk you through this when you get older.

Contents

Chapter 1

Introduction

> "The solar system has no anxiety about its reputation."
>
> *Ralph Waldo Emerson*

The Sun is a massive ball of electrically neutral ionised gas, or plasma, which sustains all life on Earth. It contains around 99.9% of all the mass in our solar system (Woolfson, 2000) and is responsible for a wide range of physical phenomena. The goal of this thesis is to examine some of these phenomena, specifically energy release and particle acceleration in the solar atmosphere. We begin by briefly discussing the structure of the Sun and its atmosphere.

Hydrogen, of which the Sun primarily consists, is fused by the enormous temperature and gravitational pressure at the Sun's core to produce helium and incredible amounts of energy - around 3×10^{33} erg every second (NASA, 2013b). This energy is transported outwards through the Sun's various layers (see Figure 1.1).

Initially, due to the high temperature ($\sim 10^7$ K in the core) and density (up to $10^{26}\,\mathrm{cm}^{-3}$) of the inner Sun, thermal radiation is the mode of energy transport. At a radius of about $0.7R_\odot$ (the solar radius $R_\odot$ is approximately 10^6 km), a thin region known as the tachocline signifies the transition between the radiative and the convective regions. Above the tachocline the pressure is low enough to allow convection of the plasma - thermal cells of plasma cycle through a process of heating and expanding, rising to the surface, cooling and

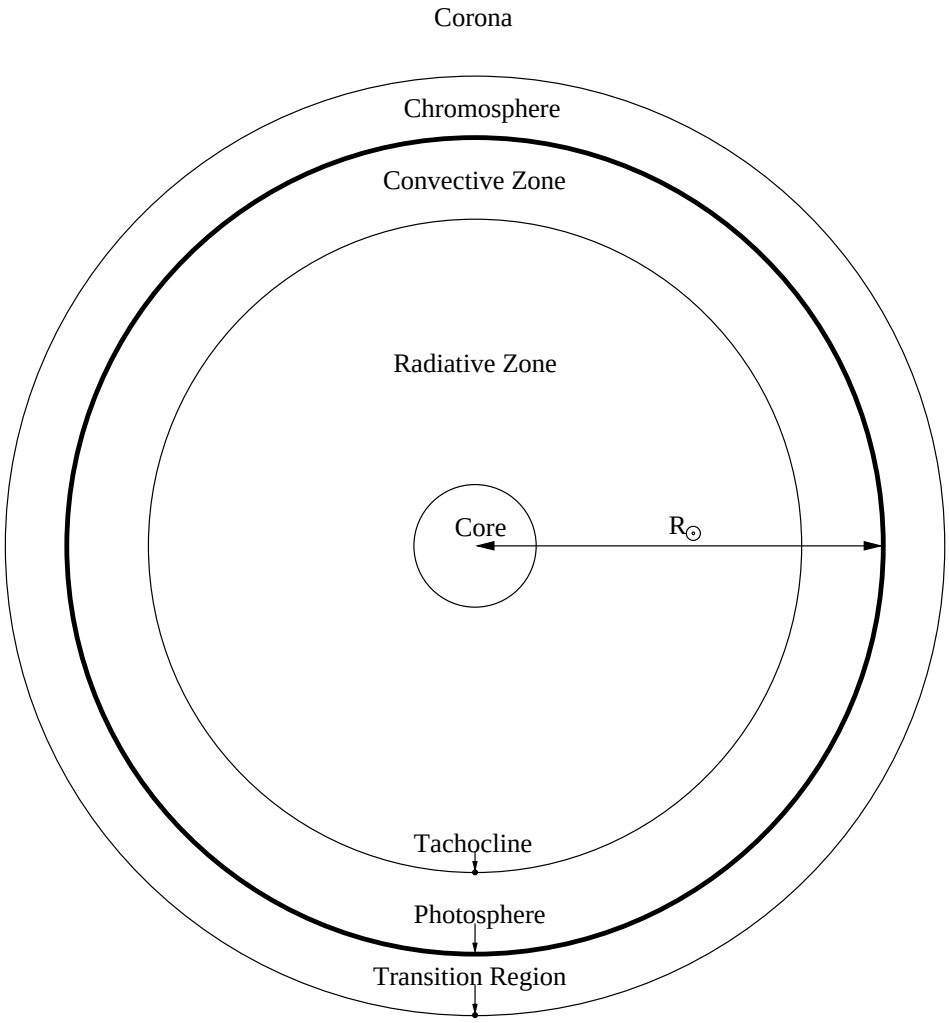

Figure 1.1: A cross-section representation showing the various layers of the Sun. The heliosphere is not pictured as it starts at around $20R_{\odot}$ from the Sun's surface.

dropping back down. The movements of the plasma in the convective region create constantly varying strong magnetic fields, which are the source of many of the extraordinary events witnessed throughout the Sun's atmosphere.

The surface of the sun is known as the photosphere, and is where some of the Sun's energy manifests as visible light. The temperature of the photosphere (5×10^3 K) is significantly lower than the core. Counter-intuitively, however, the temperature does not initially keep decreasing as the distance from the Sun increases - the atmospheric plasma actually becomes hotter by several orders of magnitude.

The chromosphere is the lowest layer of the atmosphere. Visible at the

beginning and end of a solar eclipse as a reddish flash, it is a very low density thin ($\sim 10^3$ km) region whose temperature varies from $\sim 5 \times 10^3$ K at its base to $\sim 3 \times 10^4$ K at its top. Observable solar phenomena from this layer include filaments - sporadic large gaseous plumes that can extend beyond the chromosphere - and spicules (fibrils/mottles) - numerous short-lived thin tubes of plasma that rise to the top of the chromosphere before dissipating.

A narrow transition region separates the optically thick chromosphere from the optically thin corona. Here the temperature jumps to around 10^6 K in a distance of just 100 km. The corona, predominantly consisting of ionised hydrogen, extends far into the solar system and can reach temperatures in excess of 10^7 K. The reasons for these high temperatures are not well understood, but they may be related to the most spectacular of the Sun's phenomena: the solar flare. A solar flare is a massive explosive event - a modest flare can release as much energy as one million of the largest nuclear bombs. These events may be accompanied by a coronal mass ejection (CME), where a large volume of coronal plasma is thrown out with the blast.

Another prominent phenomenon originating in the corona is the solar wind - a constant stream of particles, following "open" field lines, that are blown out from the corona. The final layer of the Sun's atmosphere, the heliosphere, begins where these particles become supersonic and ends where they meet the enveloping interstellar medium - the matter that fills the void between stars. In and around this region, named the heliosheath, particles are accelerated to great energies due to the turbulent environment.

1.1 Solar flares and energy release

Observations of the low corona (for example see Priest and Forbes (2000) or the SOHO satellite website (NASA, 2013a)) show massive magnetic energy release events, with energies ranging between $\sim 10^{27}$–10^{32} ergs, occurring in a matter of minutes. These explosions are known as solar flares.

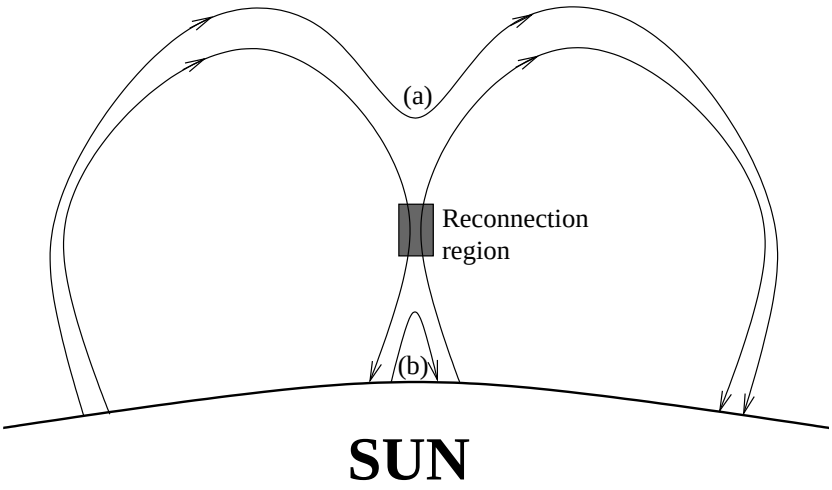

Figure 1.2: Representation of magnetic reconnection occurring in the corona. The oppositely directed magnetic field lines of coronal loops are forced together in the (shaded) reconnection region. Here they break and reconnect into the configurations of lines (a) and (b).

Solar flares are not simply a curiosity for us. Flare activity has been found, for example, to disrupt telecommunications on Earth, and represent a significant hazard to astronauts outside the shelter of the atmosphere (Schwenn, 2006). As an extreme example, on the 13th of March 1989, a solar flare caused the collapse of the Hydro-Québec power network in Canada, knocking out power to approximately six million people for nine hours (Kappenman, 2004).

A key process in the release of energy in the solar atmosphere is thought to be magnetic reconnection. Figure 1.2 shows how the energy stored in the Sun's magnetic field may be released via reconnection. Volatile magnetic loops, created by the convective motions of the plasma within the Sun's convective region, extend out into the corona. When oppositely directed field lines are forced together they can break and reconnect, which changes the topology of the field and leads to energy release. The equations that govern magnetic reconnection are known as the magnetohydrodynamic (MHD) equations.

Early models of reconnection focused solely on resistive energy release resulting from the large electric currents generated by reconnection. However this was found to be insufficient - for one thing the smallness of the resistivity in the corona means that massive field gradients are required to achieve the

observed energy dissipation rates. Furthermore, consider the magnetic energy stored in a typical active region with field strength 100 Gauss. For a large flare ($\sim 10^{32}$ ergs), if resistive energy release was the only mechanism, we would need all the energy in an expansive $10^{13.5}\,\mathrm{km}^3$ volume to be released.

These reasons have motivated the inclusion of other physical processes to explain the observed rapid flare energy release. These include the Hall effect (e.g. Biskamp *et al.*, 1995; Knoll and Chacón, 2006), turbulence (e.g. Kowal *et al.*, 2009) and viscous damping (e.g. Hollweg, 1986; Craig *et al.*, 2005). Of interest to us in this thesis is the effect of viscosity. As we shall see, the inclusion of viscosity in reconnective models is important for understanding effective energy release in solar flares.

1.2 Particle acceleration

Energy release in the Sun's atmosphere can have a number of effects. The most obvious effect is heating - flare events lead to plasma temperatures in excess of 10^7 K (Priest and Forbes, 2000). Analogous to fluid waves, magnetohydrodynamic waves can be produced, as can a full spectrum of electromagnetic radiation. Furthermore, particles can be accelerated to very high energies and transported across the solar system. It is the last of these effects, particle acceleration and transport, which will be a focus for this thesis.

In general, accelerated particle distributions are common throughout the universe (Burbidge, 1956; Parker, 1958). As mentioned previously, accelerated particles present a serious health risk to astronauts outside the safety of the Earth's atmosphere. Satellites can be damaged and their orbits degraded by collisions with high energy cosmic-rays (Pickel and Blandford, 1980). Furthermore, the solar wind's interaction with the Earth's magnetic field cause the aurora borealis and the aurora australis.

We will take a Fokker-Planck approach to modelling particle acceleration, which describes motion due to the effects of advection and diffusion. In par-

ticular we shall exploit the equivalence of the Fokker-Planck equation with a system of stochastic differential equations. This will be seen to provide both numerical and analytical advantages over the original Fokker-Planck equation.

One phenomenon that we shall explore in detail will be the production of cosmic-rays at the heliospheric termination shock. These ultra-high energy particles are accelerated to high energies ($10-100\,\mathrm{MeV}$, Kallenrode, 2004) due to interactions with turbulent magnetohydrodynamic waves and large scale variations in the magnetic field (Schlickeiser and Shalchi, 2008).

1.3 Thesis overview

This thesis covers two different but related areas of solar research, magnetic reconnection and particle acceleration. Throughout, we work in Gaussian centimetre-gram-second (cgs) units.

The chapters are laid out as follows. Chapter 2 describes the MHD equations and simplifies them to a planar incompressible formulation. We outline some early reconnection models and the more recent, inviscid, exact MHD solution of Craig and Henton (1995), while discussing the implications for resistive energy release.

We begin Chapter 3 by introducing scaling arguments and exact solutions of the MHD equations that include viscosity. A series of numerical calculations, in a simple "head-on" configuration, are performed to study the properties of a symmetrical reconnection region. Energy release rates and properties of the reconnection region are calculated and compared with the predictions of the analytical results.

In Chapter 4 we generalise our simulations by using a less restrictive initial condition - a modified Orszag and Tang (1979) vortex. Resistive and viscous energy dissipation rates are calculated. We discuss the implications for viscosity as an effective energy release mechanism.

Chapter 5 gives a description of the Fokker-Planck equation for modelling

particle acceleration and transport. We adapt the equation for use in the case of charged particles and discuss its equivalence to a system of stochastic equations. Numerical and analytical techniques are outlined by applying these results to a couple of physically motivated examples.

In Chapter 6 we use the results of Chapter 5 to model cosmic-ray particle acceleration at the heliospheric termination shock. We present analytical solutions for various physical cases and compare them with numerical simulations.

The discussion and conclusions of this thesis are contained in Chapter 7.

Chapter 2

MHD equations and early reconnection models

2.1 Introduction

In this chapter we introduce the system that we use to study magnetic reconnection in coronal plasmas, as well as outlining some early models of reconnection. Our objective is to lay the mathematical ground work for the reconnection studies of this thesis.

We take the equations of magnetohydrodynamics (MHD) to be the governing system for our work on magnetic reconnection. This approach, which treats the plasma as a fluid, differs from others such as kinetic type particle-in-cell (where individual particles are tracked) or particle distribution function (for example see Chapters 5 and 6) methods. While describing the plasma using MHD means that some plasma phenomena, such as wave-particle interactions (Landau, 1946) or double layers (parallel plasma layers with opposite electric charge), are not modelled, MHD is generally accepted to be accurate in a large number of astrophysical situations (Priest and Forbes, 2000).

In Section 2.2.1 we sketch a derivation of the general three-dimensional equations of MHD by combining Maxwell's equations of electromagnetism and the equations of fluid dynamics. These are non-dimensionalised in Section

2.2.2 using typical coronal values, and we discuss resistive and viscous energy dissipation mechanisms in Section 2.2.3. To complete our formulation of the MHD system we simplify to planar geometry, and adopt the incompressible approximation, in Section 2.3.

Having laid the mathematical groundwork we move on to discussing some basic models of reconnection in Section 2.4. The Sweet-Parker (Section 2.4.1) and Petschek (Section 2.4.2) models are discussed, before examining inviscid 2D (Craig and Henton, 1995) and 3D (Craig and Fabling, 1996) reconnection solutions in Sections 2.4.3 and 2.4.4. Section 2.5 contains our summary.

2.2 Magnetohydrodynamic system

The MHD equations are derived from Maxwell's equations of electromagnetism, supplemented by Ohm's Law, the Navier-Stokes equations of fluid dynamics, and the laws of conservation of mass and energy (see Priest and Forbes (2000) for a detailed review). The plasma is treated as a non-relativistic collisional conductive fluid (Maxwell-Boltzmann ideal gas (Priest, 1982)), where magnetic fields can induce velocity fields in the plasma and vice-versa. We begin by outlining the derivation of the MHD equations.

2.2.1 Derivation of the MHD equations

Maxwell's equations of electromagnetism (in Gaussian cgs units) are

$$\frac{\partial \mathbf{E}}{\partial t} = c\nabla \times \mathbf{B} - 4\pi \mathbf{J}, \tag{2.1}$$

$$\frac{\partial \mathbf{B}}{\partial t} = -c\nabla \times \mathbf{E}, \tag{2.2}$$

$$\nabla \cdot \mathbf{E} = 4\pi \bar{q}, \tag{2.3}$$

$$\nabla \cdot \mathbf{B} = 0. \tag{2.4}$$

They describe the interactions of an electric field $\mathbf{E}$ and a magnetic field $\mathbf{B}$. Here $\bar{q}$ and $\mathbf{J}$ are the charge and current densities and $c = 2.998 \times 10^{10}\,\mathrm{cm\,s^{-1}}$

is the speed of light. A non-relativistic plasma must also obey Ohm's Law

$$\mathbf{J} = \sigma \left(\mathbf{E} + \frac{1}{c} \mathbf{v} \times \mathbf{B} \right), \tag{2.5}$$

where σ is the electric conductivity. For a fully ionized coronal plasma of temperature $T = 10^6 K$, the conductivity is $\sigma \simeq 10^7 T^{3/2}\,\mathrm{s}^{-1} \simeq 10^{16}\,\mathrm{s}^{-1}$ (Priest, 1982).

The displacement current ($\partial \mathbf{E}/\partial t$) can be neglected due to the plasma being non-relativistic. Following Priest (1982), a dimensional analysis of equation (2.2) gives $E_0 \approx l_0 B_0/(ct_0)$, where E_0, l_0, B_0 and t_0 are typical electric field, length, magnetic field and time values respectively. The displacement current magnitude is

$$\frac{\partial E}{\partial t} \approx \frac{E_0}{t_0} \approx \frac{l_0 B_0}{c t_0^2} \approx \frac{v_0^2}{c} |\nabla \times \mathbf{B}|$$

where $v_0 = l_0/t_0$ is a typical velocity. Clearly, since $v_0 \ll c$, the displacement is small compared to the first term on the right of (2.1). We can therefore write Ampere's Law in the form

$$\mathbf{J} = \frac{c}{4\pi} \nabla \times \mathbf{B}. \tag{2.6}$$

Combining Ampere's and Ohm's Laws, and taking the curl, gives

$$-c \nabla \times \mathbf{E} = \nabla \times (\mathbf{v} \times \mathbf{B}) - \frac{c^2}{4\pi\sigma} \nabla \times (\nabla \times \mathbf{B}).$$

Substituting equation (2.2) and using $\nabla \times (\nabla \times \mathbf{B}) = -\nabla^2 \mathbf{B}$ (where we made use of equation (2.4)) gives the induction equation

$$\frac{\partial \mathbf{B}}{\partial t} = \nabla \times (\mathbf{v} \times \mathbf{B}) + \bar{\eta} \nabla^2 \mathbf{B}, \tag{2.7}$$

where we define the resistivity

$$\bar{\eta} = \frac{c^2}{4\pi\sigma}.$$

The first term on the right of the induction equation (2.7) accounts for advection due to the Lorentz force, and the second represents diffusion via resistive effects.

Modelling a plasma as a fluid requires the plasma be collisional, in other words the length scales of the system must be much greater than typical internal length scales of particle motions (Lifshitz and Pitaevskii, 1981). One such length scale is the gyro-radius, being the radius of the circular path a charged particle of mass m and speed v would make in a magnetic field of strength B. It is (Huba *et al.*, 2009)

$$r = \frac{cmv}{eZB} = \frac{1.099 \times 10^4}{ZB} \left(\frac{mT}{m_u}\right)^{1/2} \text{cm}. \tag{2.8}$$

Here $m_u = 1.661 \times 10^{-24}\,\text{g}$ is the unit atomic mass and $Z = |q/e|$, where q is the particle charge and $e = 4.803 \times 10^{-10}$ statC is the fundamental charge unit. Coronal plasma predominantly consists of fully ionised hydrogen (Priest, 1982). Therefore considering a hydrogen plasma with temperature of $T = 10^6\,K$ and average field strength of $B = 10^2\,\text{G}$, both being typical of coronal active regions, gives gyro-radii of $r_e \simeq 10^3\,\text{cm}$ and $r_p \simeq 10^5\,\text{cm}$ for electrons ($m_e = 9.109 \times 10^{-28}\,\text{g}$) and protons ($m_p = 1.673 \times 10^{-24}\,\text{g}$) respectively.

Another internal length scale can be found by considering collisional particle interactions. The mean free path x of a plasma particle when experiencing collisions with particles of the same type, in a Maxwell-Boltzmann plasma, is (Spitzer, 1962)

$$x = 11.4 \left(\frac{3k_B}{m_u}\right)^{1/2} \frac{T^2}{nZ^4\lambda} = 1.47 \times 10^5 \frac{T^2}{nZ^4\lambda}\,\text{cm}. \tag{2.9}$$

Here $k_B = 1.3803 \times 10^{-16}\,\text{erg}\,\text{deg}^{-1}$ is the Boltzmann constant, the Coulomb logarithm λ generally varies between 5 and 25 in the corona (Priest, 1982), and n is the particle number density. For a $T = 10^6\,K$ plasma with density $n = 10^9\,\text{cm}^{-3}$, the mean free paths for electrons and protons are $x_e = x_p \simeq 10^7\text{cm}$.

Global coronal length scales (a typical coronal active-region loop length is $\sim 10^{9.5}\,\text{cm}$ (Priest, 1982)) can be at least an order of magnitude greater than the larger mean free path scales mentioned above, meaning we might expect to be able to treat the plasma as collisional and apply the equations of fluid mechanics to our system. We note that smaller structural length scales, such as

current sheet widths, can cast doubt on the validity of taking an MHD model. However, within such structures, internal plasma scales may also be smaller. For instance a current sheet would have higher local magnetic fields leading to smaller gyro-radii. Furthermore, MHD-like equations can describe particle interactions perpendicular to magnetic field lines (Chew *et al.*, 1956) and wave particle interactions impede charged particle motion (Priest and Forbes, 2000). More generally, MHD encapsulates momentum, mass and energy conservation principles (Parker, 1996) and has proven to be successful in describing a wide variety of plasma phenomena.

The equation of mass conservation is

$$\frac{\partial \rho}{\partial t} + \nabla \cdot (\rho \mathbf{v}) = 0, \tag{2.10}$$

where ρ is the plasma density, and the Navier-Stokes (momentum) equations are

$$\rho \left(\frac{\partial \mathbf{v}}{\partial t} + (\mathbf{v} \cdot \nabla)\mathbf{v} \right) = \frac{1}{c} (\mathbf{J} \times \mathbf{B}) - \nabla p + \nabla \cdot \mathcal{S}. \tag{2.11}$$

The Navier-Stokes equations describe the motion of a fluid element due to the forces acting on it. The terms on the right of equation (2.11) represent the Lorentz force due to the magnetic field, the plasma pressure (p) gradient, and the force due to viscosity, where $\mathcal{S}$ is the viscous stress tensor. We have neglected the electric force due to it being proportional to $(v_0/c)^2 \ll 1$ (Roberts, 1967). The energy per unit volume ξ of a plasma is the sum of the kinetic, internal and magnetic energy densities

$$\xi = \frac{\rho v^2}{2} + \rho\varepsilon + \frac{B^2}{8\pi},$$

where

$$\varepsilon = \frac{p}{(\gamma - 1)\rho}$$

is the internal energy density per unit mass, with the ratio of specific heats $\gamma = 5/3$ for fully ionised hydrogen (Priest, 1982). By combining the induction (2.7), mass continuity (2.10) and momentum (2.11) equations we can write the

equation of energy conservation in the form

$$\begin{aligned}\frac{\partial \xi}{\partial t} &= -\nabla\cdot\left[\left(\frac{\rho v^2}{2}+p\right)\mathbf{v}+\frac{1}{4\pi}\mathbf{B}\times(\mathbf{v}\times\mathbf{B})-\frac{\bar{\eta}}{c}(\mathbf{J}\times\mathbf{B})-\mathcal{S}\cdot\mathbf{v}\right]\\ &\quad +p\nabla\cdot\mathbf{v}+\frac{\partial}{\partial t}(\rho\varepsilon)-\frac{4\pi\bar{\eta}}{c^2}J^2-\mathcal{S}_{ij}\frac{\partial v_i}{\partial x_j},\end{aligned} \tag{2.12}$$

where $(\mathcal{S}\cdot\mathbf{v})_j \equiv \mathcal{S}_{ij}v_i$ and x_j are the spatial coordinates. As usual, summation over repeated indices is assumed.

The MHD system is not fully specified unless an equation of state, relating pressure, density and internal energy ($p = p(\rho, \varepsilon)$), is given. As this could take a number of different forms we leave further discussion of this relation until Section 2.3, where we introduce the incompressible assumption. To simplify our analysis, and for consistency with the literature, we non-dimensionalise the MHD equations: Gauss's law for magnetism (2.4) and the induction (2.7), mass conservation (2.10), momentum (2.11), and energy conservation (2.12) equations.

2.2.2 Non-dimensionalisation

As we will be looking at coronal applications of the MHD equations it makes sense to non-dimensionalise them using typical coronal parameters: magnetic field strength $B_c = 10^2\,\mathrm{G}$, length scale $l_c = 10^{9.5}\,\mathrm{cm}$, and number density $n_c = 10^9\,\mathrm{cm}^{-3}$ (mass density $\rho_c = m_p n_c \simeq 10^{-15}\,\mathrm{g\ cm}^{-3}$). Velocities are expressed in units of the Alfvén speed

$$v_A = \frac{B}{(4\pi\rho)^{1/2}}, \tag{2.13}$$

where we have $v_A \simeq 10^9\,\mathrm{cm\ s}^{-1}$ for the above coronal values. Time is expressed in units of the Alfvén time $t_A = l_c/v_A \simeq 3\mathrm{s}$. Under these normalisations the MHD equations become

$$\rho\left(\frac{\partial \mathbf{v}}{\partial t}+(\mathbf{v}\cdot\nabla)\mathbf{v}\right) = \mathbf{J}\times\mathbf{B}-\frac{1}{2}\nabla p+\nabla\cdot\mathcal{S}, \tag{2.14}$$

$$\frac{\partial \mathbf{B}}{\partial t} = \nabla\times(\mathbf{v}\times\mathbf{B})+\eta\nabla^2\mathbf{B}, \tag{2.15}$$

$$\frac{\partial \rho}{\partial t}+\nabla\cdot(\rho\mathbf{v}) = 0, \tag{2.16}$$

$$\nabla\cdot\mathbf{B} = 0, \tag{2.17}$$

with the energy equation expressed as (Craig and Litvinenko, 2009)

$$\frac{\partial \xi}{\partial t} = -\nabla \cdot \mathbf{P} + \frac{p}{2}\nabla \cdot \mathbf{v} + \frac{\partial}{\partial t}(\rho\varepsilon) - \eta J^2 - \mathcal{S}_{ij}\frac{\partial v_i}{\partial x_j}, \tag{2.18}$$

where

$$\mathbf{P} = \frac{1}{2}\left(\rho v^2 + p\right)\mathbf{v} + \mathbf{B} \times (\mathbf{v} \times \mathbf{B}) - \eta \mathbf{J} \times \mathbf{B} - \mathcal{S} \cdot \mathbf{v}$$

is the Poynting vector and $\mathbf{J} = \nabla \times \mathbf{B}$ is the non-dimensional current density. Here the plasma pressure p has been normalised with respect to the background magnetic energy density ($B_c^2/8\pi$) and the stress tensor normalised by a factor of $\rho_c v_c^2$. The non-dimensional resistivity is an inverse Lundquist number given by

$$\eta = \frac{\bar{\eta}}{l_c v_A} \simeq 10^{-5.5} T_c^{-3/2}$$

(Spitzer, 1962), which is $\eta \simeq 10^{-14.5}$ for a $T_c = 10^6\,\mathrm{K}$ coronal plasma. The smallness of this value means that steep gradients in the magnetic field must be present for effective diffusion of flux. As we shall see, this presents a problem when trying to explain the observed energy release.

It may seem that the MHD system is over-determined, as there are 12 equations (equations (2.14-2.18) and $\mathbf{J} = \nabla \times \mathbf{B}$) for 11 variables ($\mathbf{v}$, $\mathbf{B}$, $\mathbf{J}$, p, ρ). However, taking the divergence of the induction equation (2.15) results in $\nabla \cdot \mathbf{B}$ being constant - Gauss's law (2.17) actually serves as an initial condition (Priest and Forbes, 2000).

2.2.3 Energy dissipation

To calculate global energy release rates we can integrate the energy equation (2.18) over a volume V. We define two resulting measures of energy dissipation: resistive (Ohmic) and viscous dissipation.

Energy dissipation via resistive effects has been considered to be the main mechanism for energy release in flares. The resistive dissipation is defined as

$$W_\eta = \int \eta J^2 \,\mathrm{d}V. \tag{2.19}$$

Reconnection solutions are classified according to how the resistive dissipation scales with the resistivity, $W_\eta \sim \eta^k : \ k \in \mathbb{R}$. Due to the smallness of the typical values of resistivity (recall $\eta \simeq 10^{-14.5}$ in the corona), a solution with $k \leq 0$ is known as "fast" reconnection, as it corresponds to a high resistive energy dissipation rate. Care must be taken when interpreting such solutions, however, as the dissipation tends to infinity for very small values of resistivity; Craig and Watson (2000) discuss how the dissipation could be limited by the current sheet magnetic field only building up to a level comparable with the external pressure. On the other hand "slow" reconnection solutions, for which $k > 0$, result in insufficient dissipation to explain flare energy release.

These issues have motivated the inclusion of other physical effects to help explain the observed dissipation rates. The primary focus for the reconnection work contained in this thesis is the inclusion of viscosity. Several studies (e.g. Hollweg, 1986; Craig and Litvinenko, 2009) have pointed out that viscous dissipation has the potential to dominate resistive dissipation in a variety of astrophysical situations. At the very least, reconnection is unlikely to be greatly affected by the inclusion of viscosity (Fabling and Craig, 1996). The dissipation due to viscous effects is given by

$$W_\nu = \int \mathcal{S}_{ij} \frac{\partial v_i}{\partial x_j} \, \mathrm{d}V. \tag{2.20}$$

Both the above and equation (2.19) are scaled using $W_c = v_A B_c^2 V_c/(4\pi l_c)$. Taking a normalising volume of a unit cube ($V_c = l_c^3$) results in a dissipation rate of $W_c \simeq 8 \times 10^{30} \, \mathrm{erg \, s^{-1}}$. Considering that a typical flare releases around $10^{30} \, \mathrm{erg}$ over a period of about 100 s, we would need an energy dissipation rate of approximately 10^{-3} in our non-dimensional units.

We shall make use of two alternate forms of the viscosity tensor $\mathcal{S}_{ij}$. Viscous effects in a hydrogen plasma are primarily due to proton-proton interactions (Hollweg, 1985). Classical isotropic viscosity

$$\mathcal{S}_{ij} = \nu \left(\frac{\partial v_i}{\partial x_j} + \frac{\partial v_j}{\partial x_i} - \frac{2}{3} \frac{\partial v_k}{\partial x_k} \delta_{ij} \right), \tag{2.21}$$

while being commonly employed (e.g. Park *et al.*, 1984, Heerikhuisen *et al.*,

2000), becomes inaccurate in the presence of strong magnetic fields (such as those present in the corona).

A better physical representation is the Braginskii (1965) ion parallel viscosity

$$\mathcal{S}_{ij} = \nu \left(3\frac{B_i B_j}{B^2} - \delta_{ij} \right) \left(\frac{B_k B_l}{B^2} \frac{\partial v_k}{\partial x_l} - \frac{1}{3} \frac{\partial v_k}{\partial x_k} \right). \tag{2.22}$$

This form accounts for anisotropy introduced by the magnetic field. Particles travelling along a magnetic field line have length scales of the same order as the collisional proton mean-free path (2.9). However, for particle motion perpendicular to the field, length scales are of the same order as the proton gyro-radius (2.8). If the proton gyro-radius is exceeded by the mean-free path then isotropy breaks down and equation (2.22) is applicable (Hollweg, 1986; Craig, 2008). Furthermore, due to the smaller length scale, the viscous force perpendicular to the magnetic field is greatly suppressed (Braginskii, 1965).

Using the typical coronal values of Section 2.2.1 leads to $x_p/r_p \simeq 10^2 \gg 1$; in other words the Braginskii viscosity (2.22) should be used in the majority of coronal applications. We note that the Braginskii viscosity tensor (2.22) cannot be applied in regions of weak magnetic fields, as there the proton gyro-radius would exceed the mean-free path. In practice a form that interpolates between the Braginskii and classical viscosities is required (see equation (2.33)).

The viscosity coefficient (Spitzer, 1962)

$$\nu \simeq 10^{-19.5} T_c^{5/2}, \tag{2.23}$$

which is non-dimensionalised using $\rho_c v_A l_c \simeq 10^{3.5}\,\mathrm{g\,cm^{-1}\,s^{-1}}$, is an inverse Reynolds number defined in terms of the Alfvén speed. In active region plasmas where the temperature can vary appreciably ($2 \times 10^6\,\mathrm{K} \leq T_c \leq 10^7\mathrm{K}$), the viscous coefficient can vary between $10^{-4} \leq \nu \leq 10^{-2}$ (e.g. Priest, 1982). Clearly $\nu \gg \eta$ (recall $\eta \sim 10^{-14}$ in our non-dimensional units), so we might naturally expect viscous dissipation to dominate resistive dissipation in the corona. We will explore this idea in detail in Chapters 3 and 4.

2.3 Incompressible planar MHD equations

If we wish to analytically and numerically describe viscous reconnection we need to make some physically motivated simplifying assumptions. We begin by restricting ourselves to the simplest possible geometry under which reconnection can occur, planar (2D) Cartesian geometry. This has the advantage of being both relatively computationally accessible and well described, for certain cases, in the literature (see Section 2.4). Under this assumption we can write the velocity and magnetic fields in terms of stream (ϕ) and flux (ψ) functions

$$\mathbf{v} = \nabla\phi(x,y) \times \hat{\mathbf{z}}, \tag{2.24}$$

$$\mathbf{B} = \nabla\psi(x,y) \times \hat{\mathbf{z}}. \tag{2.25}$$

Note that Gauss's law for magnetism (2.17) is now satisfied identically.

We assume that the plasma is incompressible. In this approximation the density is taken to be a normalised constant ($\rho \to 1$) and thermodynamic properties of the plasma (e.g. temperature) are not modelled. Inclusion of finite compressibility will give rise to phenomena not represented in an incompressible formulation, including density inhomogeneities and compressional MHD waves that travel perpendicular to the magnetic field (Biskamp, 1986). However, both analytical and numerical results (Rickard and Craig, 1993; Craig and Litvinenko, 2007) indicate that any effects on the current sheet scalings arising from compressibility will be relatively minor. That is, the overall energy dissipation scalings are expected to remain robust (Litvinenko and Craig, 2003).

The MHD equations (2.14-2.18) reduce to the momentum, induction and energy equations in the form

$$\frac{\partial}{\partial t}\left(\nabla^2\phi\right) + [\nabla^2\phi,\, \phi] = [\nabla^2\psi,\, \psi] + G, \tag{2.26}$$

$$\frac{\partial\psi}{\partial t} + [\psi,\, \phi] = \eta\nabla^2\psi, \tag{2.27}$$

$$\frac{\partial\mathcal{E}}{\partial t} = -(W_\eta + W_\nu) - \int \mathbf{P}\cdot \mathrm{d}\mathbf{S}, \tag{2.28}$$

where we made use of the curled form of equation (2.14) and we have used the

divergence theorem to express the Poynting flux term as a surface integral (S being the surface of the volume V). The global energy is

$$\mathcal{E} = \int \left(\frac{v^2}{2} + \frac{B^2}{2} \right) \mathrm{d}V. \tag{2.29}$$

The above Poisson bracket notation is typified by

$$[\psi,\, \phi] = \frac{\partial \psi}{\partial x}\frac{\partial \phi}{\partial y} - \frac{\partial \psi}{\partial y}\frac{\partial \phi}{\partial x},$$

viscous effects are represented by

$$G = -\left(\nabla \times \nabla \cdot \mathcal{S}\right) \cdot \hat{\mathbf{z}}, \tag{2.30}$$

and the classical and Braginskii viscosity tensors are

$$\mathcal{S}_{ij} = \nu \left(\frac{\partial v_i}{\partial x_j} + \frac{\partial v_j}{\partial x_i} \right), \tag{2.31}$$

and

$$\mathcal{S}_{ij} = \nu \left(3\frac{B_i B_j}{B^2} - \delta_{ij} \right) \left(\frac{B_k B_l}{B^2} \frac{\partial v_k}{\partial x_l} \right) \tag{2.32}$$

respectively. We recall that the Braginskii viscosity tensor (2.32) is not applicable in the region of fields that are very weak. Furthermore, small values of B^2 in the above equation would cause numerical difficulties. Since reconnection simulations generally involve null points, it is convenient to use a form that effectively interpolates between the classical and Braginskii viscosities (Hosking and Marinoff, 1973). For our simulations we adopt the form

$$\mathcal{S}_{ij} = \nu \left(\frac{\frac{\partial v_i}{\partial x_j} + \frac{\partial v_j}{\partial x_i} + \theta^4 \left(3B_iB_j - B^2\delta_{ij}\right) B_m B_k \frac{\partial v_m}{\partial x_k}}{1 + \theta^4 B^4} \right), \tag{2.33}$$

where θ is a parameter that determines the relative weighting of the viscosities. Equations (2.26-2.33) form the system on which all our analytical and numerical work will be based. In practice, for a given viscosity tensor, we solve equations (2.26) and (2.27) for ϕ and ψ, allowing $\mathbf{v}$ and $\mathbf{B}$ to be calculated. It is then straightforward to calculate energy dissipation via equations (2.19) and (2.20).

2.4 Early reconnection models

In this section we review some early models of reconnection. While this is by no means a complete list of early work, the models presented here introduce some basic concepts relevant to our present study. We start with Sweet-Parker merging, whose predictions and order of magnitude style arguments have been at the core of reconnection theory for decades.

2.4.1 Sweet-Parker merging

The first major contribution to the theory of reconnection was the Sweet-Parker model. Consider the situation shown in Figure 2.1. Oppositely directed magnetic field lines in an inviscid ($\mathcal{S} = 0$) incompressible ($\rho \to 1$) plasma are washed in with speed v_{in} to a region of high current density (shaded box, length l, width x_s) known as a current sheet. Here, around the central neutral point, the topology of the field lines can change through magnetic reconnection, giving large velocity gradients within the sheet and allowing rapid expulsion (with speed v_{out}) of plasma. This steady state configuration is the basis for the Sweet-Parker model (Parker, 1957, 1963; Sweet, 1958). While this is not an exact solution of the MHD equations, an order of magnitude analysis leads to scalings for quantities such as the current sheet thickness and resistive dissipation rate, which became central to the development of reconnection theory. Note that these scalings are preserved if the incompressible assumption is relaxed (Parker, 1963); we take $\rho \to 1$ for simplicity.

To derive scalings for the properties of the sheet we need to consider some basic physical relations. To begin with, mass conservation requires plasma flow in to and out of the sheet to be balanced

$$v_{in} l = v_{out} x_s. \tag{2.34}$$

Secondly we assume the inflow speed v_{in} is small compared to the magnetic field strength B_{in}, the validity of which will be checked later. Integrating the

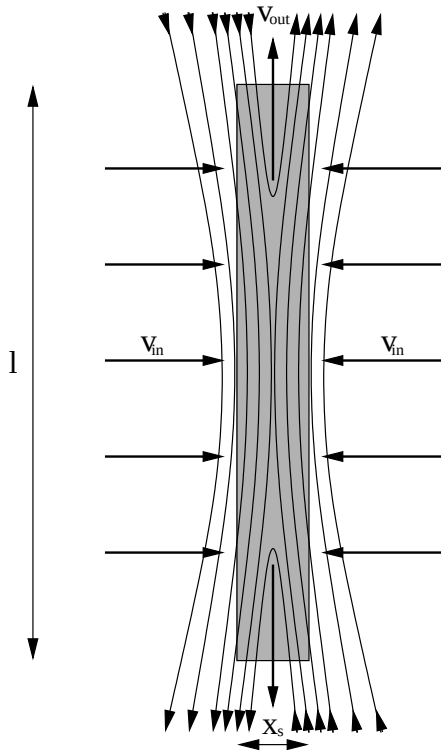

Figure 2.1: Reconnection via the Sweet-Parker mechanism. Oppositely directed field lines are washed in at speed v_{in} and reconnect in a current sheet of width x_s and length l (shaded region). The plasma is ejected in a jet with speed v_{out}.

momentum equation (2.14) along the inflow axis gives

$$p_s \simeq \frac{B_{in}^2}{2}, \tag{2.35}$$

where p_s is the current sheet pressure and we neglect the pressure outside the sheet. Conversely along the outflow axis the magnetic field is negligible and the sheet pressure is

$$p_s \simeq \frac{v_{out}^2}{2}, \tag{2.36}$$

which, when equated with equation (2.35), gives the relation

$$v_{out} \simeq B_{in}. \tag{2.37}$$

Obviously from equation (2.34) $v_{in} \ll v_{out}$, so our earlier assumption of $v_{in} \ll B_s$ is valid. Finally energy balance in the sheet is given by equation (2.28). Integrating this and using equations (2.19) and (2.37) we find

$$\eta \frac{B_{in}^2}{x_s} l \sim v_{in} l B_{in}^2, \tag{2.38}$$

where we approximate current density via $J \sim B_{in}/x_s$. Substituting the flow balance equation (2.34) gives

$$x_s^2 \sim \frac{\eta l}{v_{out}}.$$

Due to the uniformity of the inward flow profile we can keep the length scale l and the magnetic field B_{in} fixed, giving

$$x_s \sim \eta^{1/2} \tag{2.39}$$

as the scaling for sheet thickness. Using equation (2.19) the resistive dissipation scaling is

$$W_\eta \simeq \frac{\eta B_{in}^2}{x_s^2} x_s \, l \sim \eta^{1/2}. \tag{2.40}$$

This corresponds to "slow" reconnection (following the classification of Section 2.2.3) and, due to the very small coronal resistivity, the Sweet-Parker model does not result in sufficient energy release rates for flares. It does, however, provide a baseline against which other models are measured. In addition the order of magnitude arguments given here can be adapted to more complex situations, including those where viscosity is considered (see Section 3.2.1).

2.4.2 The Petschek mechanism

The Petschek (1964) mechanism (Figure 2.2) employs a similar argument to Sweet-Parker, but assumes that the length of the current sheet is significantly smaller than the global length scale, and of the same order as the sheet width ($l \simeq x_s$). One of the key features of this system is the four Alfvénic discontinuities (dashed lines) that act as "separatrices". The obvious advantages of this mechanism is its X-point nature - allowing a large angle over which to expel plasma from the reconnection region.

While the Petschek mechanism can lead to "fast" reconnection, specifically $W_\eta \sim \eta^0$, the majority of numerical simulations to date result in long, Sweet-Parker style, current sheets. Exceptions to this (e.g. Heyn and Semenov, 1996) invoke localised enhancement of the resistivity and require very specific boundary conditions, so it seems unlikely that the Petschek model is a realistic

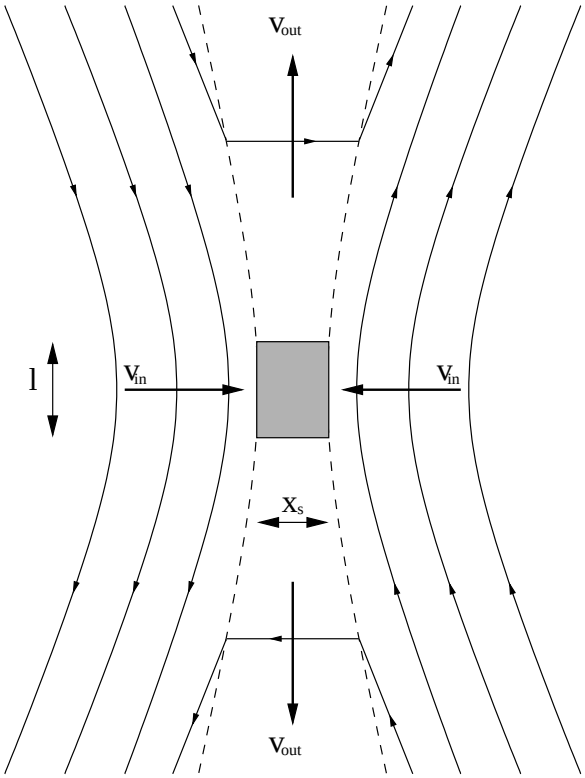

Figure 2.2: Reconnection via the Petschek (1964) mechanism, where the length of the reconnection region is of the same order as the width. Here the dashed lines indicate Alfvénic discontinuities.

mechanism for reconnection. We have included it here as it was one of the first models to examine the reconnection of curved field lines in an X-point configuration.

2.4.3 Craig and Henton reconnection solution

In the steady state, the planar equations (2.26–2.27) become

$$[\nabla^2\phi,\, \phi] = [\nabla^2\psi,\, \psi] + G, \tag{2.41}$$

$$E + [\psi,\, \phi] = \eta\nabla^2\psi, \tag{2.42}$$

where $E = \partial\psi/\partial t$ is the magnitude of the uniform electric field aligned to the negative z axis and $G = 0$ in the absence of viscosity.

Craig and Henton (1995) considered a solution of equations (2.41) and (2.42) in the inviscid case. Taking the stream and flux functions in the form

$$\begin{aligned}\phi(x,y) &= f(x) + \alpha H(x,y),\\ \psi(x,y) &= g(x) + \beta H(x,y),\end{aligned}$$

where H is a harmonic function, gives

$$E + (\alpha g' - \beta f')\frac{\partial H}{\partial y} = \eta g'', \tag{2.43}$$

$$\alpha f''' = \beta g'''. \tag{2.44}$$

Equation (2.44) has the solution

$$f(x) = \frac{\beta}{\alpha} g(x) + q(x),$$

where $q(x)$ is an arbitrary quadratic function which we can neglect as it only contributes a linear component to the flow field. Equation (2.43) implies $\partial_y H$ is a function of x only. Remembering that H is harmonic and again neglecting linear contributions, we get $H \sim xy$. Choosing $H = -xy$ for convenience (we shall show below that this corresponds to inflow along the x axis) results in the induction equation in the form

$$g'' + \frac{\mu^2}{2} x g' = \frac{E}{\eta},$$

where we define

$$\mu^2 = \frac{\alpha^2 - \beta^2}{2\alpha\eta}. \tag{2.45}$$

Solving via an integrating factor gives

$$\begin{aligned} g'(x) &= \frac{E}{\eta}\int_0^x e^{\mu^2(t^2-x^2)}\,\mathrm{d}t,\\ &= \frac{E}{\eta}\mathrm{daw}(\mu x), \end{aligned} \tag{2.46}$$

where the Dawson function is defined

$$\mathrm{daw}(s) = \int_0^s e^{\lambda^2 - s^2}\,\mathrm{d}\lambda. \tag{2.47}$$

Integrating the result with respect to x gives

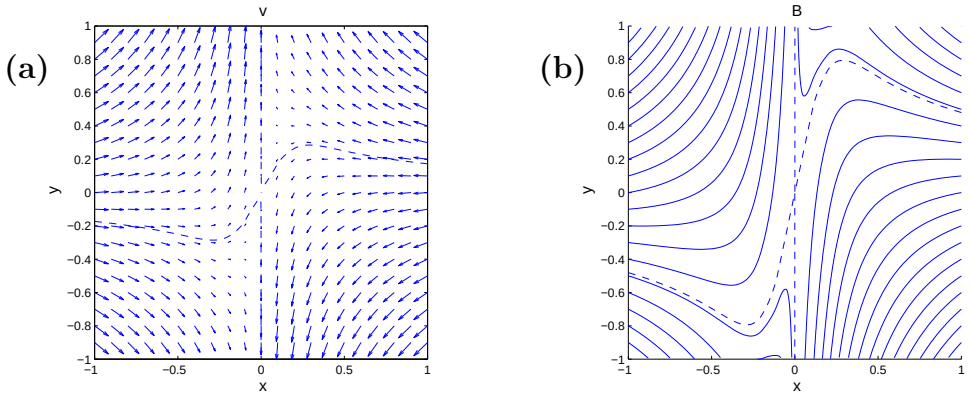

Figure 2.3: Velocity (a) and magnetic (b) fields for the Craig and Henton solution using parameters $\alpha = 1$, $\eta = 10^{-2}$ and $E = 0.07$. Here, by setting the shearing parameter $\beta = 0.6$, we have an X-point reconnection configuration. The dashed lines indicate the separatrices.

$$\psi(x) = \frac{E}{\eta}\frac{x^2}{2}{}_2F_2\left(1,\, 1,\, \frac{3}{2},\, 2,\, -\mu^2 x^2\right), \tag{2.48}$$

where ${}_2F_2$ is a hyper-geometric function (Olver *et al.*, 2010). We therefore write the stream and flux functions in the form

$$\begin{aligned} \phi(x,y) &= -\alpha x y + \frac{\beta}{\alpha} g(x), \\ \psi(x,y) &= -\beta x y + g(x), \end{aligned}$$

and the velocity and magnetic fields are given by

$$\mathbf{v} = -\alpha x \hat{\mathbf{x}} + \left(\alpha y + \frac{\beta E}{\alpha \mu \eta}\mathrm{daw}(\mu x)\right)\hat{\mathbf{y}}, \tag{2.49}$$

$$\mathbf{B} = -\beta x \hat{\mathbf{x}} + \left(\beta y + \frac{E}{\mu \eta}\mathrm{daw}(\mu x)\right)\hat{\mathbf{y}}. \tag{2.50}$$

Equations (2.49) and (2.50) comprise the inviscid, steady state, incompressible Craig and Henton (1995) solution. Equation (2.49), in contrast to the Sweet-Parker model, gives a non-uniform divergent flow with a stagnation point at the origin. The parameter α determines the amplitude of the velocity field and β controls the level of magnetic shear in the reconnection. Figure 2.3 shows the solution for sample parameters $\alpha = 1$, $\beta = 0.6$, $\eta = 10^{-2}$ and $E = 0.07$. In this case the non-zero shearing parameter gives X-point reconnection. Setting $\beta = 0$ corresponds to a head-on "annihilation" solution (Sonnerup and Priest,

1975) – field lines cancel on the y axis rather than reconnecting (see Section 3.2.2).

The above solution has been extended to both 2.5D (Fabling and Craig, 1996) and 3D (Craig and Fabling, 1996). We consider the 3D solution below.

2.4.4 Spine and Fan solutions

For completeness we briefly describe how the the solution of Craig and Henton (1995) is extended to three dimensions. The 3D, steady-state, incompressible MHD equations are

$$(\mathbf{v}\cdot\nabla)\boldsymbol{\Omega} - (\boldsymbol{\Omega}\cdot\nabla)\mathbf{v} - (\mathbf{B}\cdot\nabla)\mathbf{J} + (\mathbf{J}\cdot\nabla)\mathbf{B} = \nabla\times(\nabla\cdot\mathcal{S}), \quad (2.51)$$

$$\nabla\times(\mathbf{v}\times\mathbf{B}) + \eta\nabla^2\mathbf{B} = 0, \quad (2.52)$$

$$\nabla\cdot\mathbf{B} = \nabla\cdot\mathbf{v} = 0, \quad (2.53)$$

where $\boldsymbol{\Omega} = \nabla\times\mathbf{v}$ is the vorticity and we made use of the curled form of equation (2.14). A reconnection solution in the inviscid case can be found by taking magnetic and velocity fields of the form (Craig and Fabling, 1996)

$$\mathbf{B} = \frac{\beta}{\alpha}\mathbf{P} + \mathbf{Q}, \qquad \mathbf{v} = \mathbf{P} + \frac{\beta}{\alpha}\mathbf{Q}, \quad (2.54)$$

where $\mathbf{P}$ and $\mathbf{Q}$ are flow and magnetic disturbance fields respectively.

A generalisation of stagnation point flow profiles is given by the field

$$\mathbf{P} = \alpha(-x,\ \kappa y,\ (1-\kappa)z), \quad (2.55)$$

where isotropy is controlled by $0 \le \kappa \le 1$. As shown in Figure 2.4, plasma streams inward in a "spine" formation along the x axis to a "fan" plane at $x = 0$. Taking $\kappa = 1$ corresponds to the planar stagnation point flows of the previous Section 2.4.3.

Given this flow field, we find two forms of magnetic disturbance that satisfy the momentum equation. Fan solutions (Craig *et al.*, 1995) have planar current sheet structures formed around the magnetic null. They are derived assuming a disturbance field

$$\mathbf{Q} = (0,\ Y(x),\ Z(x))$$

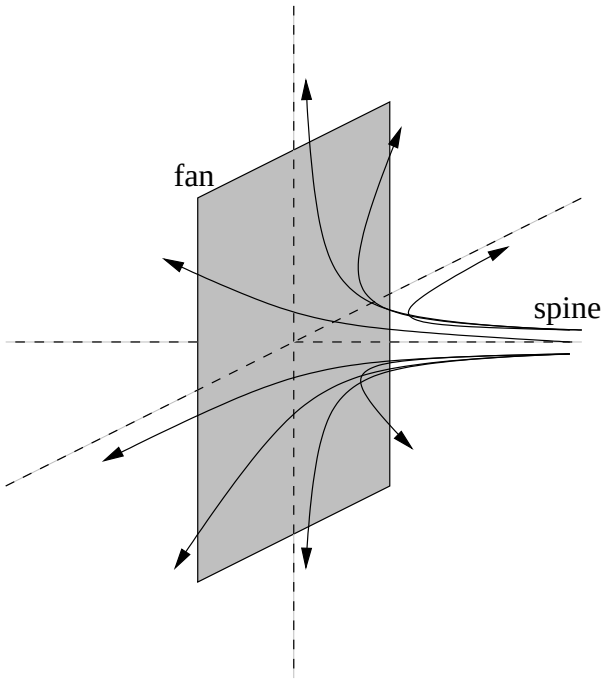

Figure 2.4: Representation of the three dimensional spine and fan flow field of equation (2.55).

that gives a current sheet in the $x = 0$ plane (the "fan").

Closely related to these are "spine" solutions (Craig and Fabling, 1996), which are derived with the form

$$\mathbf{Q} = X(y,\, z)\,\hat{\mathbf{x}}.$$

Currents are localised in quasi–cylindrical current tubes ("spines") about the x-axis.

Scaling laws for both classes of solution have been found by Craig and Watson (2000). We simply state the results here; a derivation for planar viscous solutions is presented in Sections 3.2.2 and 3.2.3. For "fan" solutions the maximum resistive dissipation rate is

$$W_\eta \simeq \eta^{1/2} B_s^{5/2},$$

where B_s is the current sheet magnetic field strength. Note that, as we will show in the next chapter, this scaling holds when viscous solutions are considered. "Spine" solutions, however, have a less effective scaling

$$W_\eta \simeq \eta B_s^2.$$

The lower dissipation rate is due to the dissipation region for the "spine" solution being much smaller than "fan"; a thin cylindrical current structure around the axis rather than a plane of current surrounding the null point.

2.5 Summary

In this chapter we have presented the equations of MHD that will form the basis of the analysis of the next two chapters. We have discussed energy release via resistive and viscous dissipation, and have given both the classical and Braginskii forms of the viscosity tensor.

In Section 2.4.1 we discussed Sweet-Parker reconnection, a fundamental model that assumes a uniform flow profile and predicts the resistive dissipation scaling $W_\eta \sim \eta^{1/2}$. The Petschek model was briefly presented in Section 2.4.2. This gave an example of an X-point reconnection configuration and results in fast energy dissipation; however it appears unlikely to be a physically realistic mechanism.

We examined exact, steady-state solutions of the inviscid MHD equations in 2D (Section 2.4.3) and 3D (Section 2.4.4). The 2D solutions arise from a stagnation point flow profile and include a flux pile-up factor B_s that allows for greater resistive dissipation $W_\eta \sim \eta^{1/2} B_s^{5/2}$ when compared to the traditional Sweet-Parker model. 3D solutions generalise the stagnation point flow concept while providing spine and fan reconnection configurations.

Having presented the MHD equations and discussed inviscid models of reconnection, we now turn to studying the effects of viscosity and what they mean for general flare energy release. In the next chapter we discuss reconnection models that include viscosity, and perform a numerical simulation designed to give a well defined reconnecting current layer.

Chapter 3

Viscous effects in time-dependent planar reconnection

3.1 Introduction

In the previous chapter we presented some simple models of resistive reconnection as a background to our work. Our present purpose is to examine and develop models that include viscosity. In this chapter we are going to present viscous analytical scaling arguments, along with exact solutions of the viscous MHD equations, and compare them with detailed numerical simulations of a simple current layer. Specifically we analyse the current sheet thickness (x_s) and inflow (v_{in}) and outflow (v_{out}) speeds, along with calculating resistive (W_η) and viscous (W_ν) dissipation rates.

Both exact solutions (Sonnerup and Priest, 1975; Litvinenko, 2005) and scaling arguments (Craig and Litvinenko, 2010) for viscous stagnation point flows predict the scalings for the current sheet properties: thickness $x_s \simeq \eta^{1/2} B_s^{-1/2}$, inflow speed $v_{in} \simeq \eta^{1/2}$ and outflow speed $v_{out} \simeq \eta^0$. More importantly the ratio of viscous to resistive dissipation scales as

$$\frac{W_\nu}{W_\eta} \simeq \frac{\nu}{B_s^{1/2} \eta^{1/2}}, \tag{3.1}$$

which predicts viscous dissipation dominance for $\nu > \eta^{1/2}$. As this inequality holds for coronal values of the parameters (see Section 2.2.3), we might expect relation (3.1) to apply in various astrophysical situations. These scalings have been found in recent exploratory simulations of viscous "head-on" reconnection (Craig, 2010) and relaxation simulations (Craig and Litvinenko, 2012).

However, a different visco-resistive scale is predicted when considering a Sweet-Parker style uniform flow profile in the presence of classical viscosity. The scalings for the current sheet properties are $x_s \simeq (\eta\nu)^{1/4} B_s^{-1/2}$, $v_{in} \simeq \eta^{3/4}\nu^{-1/4}$ and $v_{out} \simeq \eta^{1/2}\nu^{-1/2}$ (Park *et al.*, 1984). Most significantly the dissipation rates are significantly slower (Craig and Litvinenko, 2010)

$$W_\eta \simeq W_\nu \simeq \eta^{3/4}\nu^{-1/4} B_s^{5/2}. \tag{3.2}$$

The visco-resistive scaling has emerged in an analytical model of X-point reconnection (Titov and Priest, 1997) as well as various numerical models (e.g. Hassam and Lambert, 1996; Craig *et al.*, 2005; Craig, 2010). In addition, the study of Craig (2008) suggests it may hold in the presence of Braginskii viscosity.

The contradictory results of the steady analytical models motivate us to investigate the structure of a symmetric head-on reconnection region in an incompressible visco-resistive plasma, using time-dependent numerical simulations. Accordingly we investigate reconnection in a two-dimensional, doubly periodic reconnection region. Initial conditions are chosen to generate a well defined current layer in a form as similar to the models of the previous chapter as possible. Current sheet thickness, inflow and outflow speeds and viscous and resistive dissipation rates are then able to be easily calculated, and we use the scaling arguments above to interpret our numerical results.

We begin by discussing viscous reconnection models in Section 3.2, deriving the scaling arguments given above. In a manner similar to the Sweet-Parker model (Section 2.4.1), scaling law arguments that include viscosity are presented in Section 3.2.1. We then touch on the Sonnerup and Priest (1975) annihilation solution in Section 3.2.2, before discussing the Litvinenko (2005)

Braginskii viscosity solution in Section 3.2.3.

We describe our numerical model in Section 3.3. We use the numerical results to obtain scalings for both the current sheet parameters and the global rates of resistive and viscous dissipation in Section 3.4. We specifically compare the effects of the classical viscosity and the Braginskii viscosity. An exploratory analysis of the case of strongly sheared reconnecting fields is presented in Section 3.5. In Section 3.6 we give our conclusions.

3.2 Viscous reconnection models

The purpose of this section is to describe existing models for viscous reconnection. We present Sweet-Parker style scaling arguments before discussing exact solutions that are valid for classical (Section 3.2.2) and Braginskii (Section 3.2.3) viscosity.

3.2.1 Viscous Sweet-Parker style scalings

Several studies have looked to include viscous effects in a Sweet-Parker style scaling argument, most notably Park *et al.* (1984) for classical viscosity and Craig and Litvinenko (2010) for Braginskii viscosity. The resulting energy dissipation scalings depend on the assumed flow profile, as we now discuss. Similar to Sweet-Parker, the argument is based on mass continuity (2.34), steady flux transfer (2.38) and pressure balance (2.35-2.36). However the pressure balance relation is modified by inclusion of viscous effects,

$$\frac{v_{out}^2}{2} \simeq \frac{B_s^2}{2} - \frac{l}{2}\nabla \cdot \mathcal{S}, \tag{3.3}$$

where l is a global length scale. We consider two different flow profiles. On the one hand is the uniform flow profile of Sweet-Parker (Figure 2.1), where velocity gradients are only significant within the current layer. On the other hand, guided by the forms of recent exact solutions (e.g. Section 2.4.3), the stagnation point flow of Figure 3.1 has velocity gradients on a global scale.

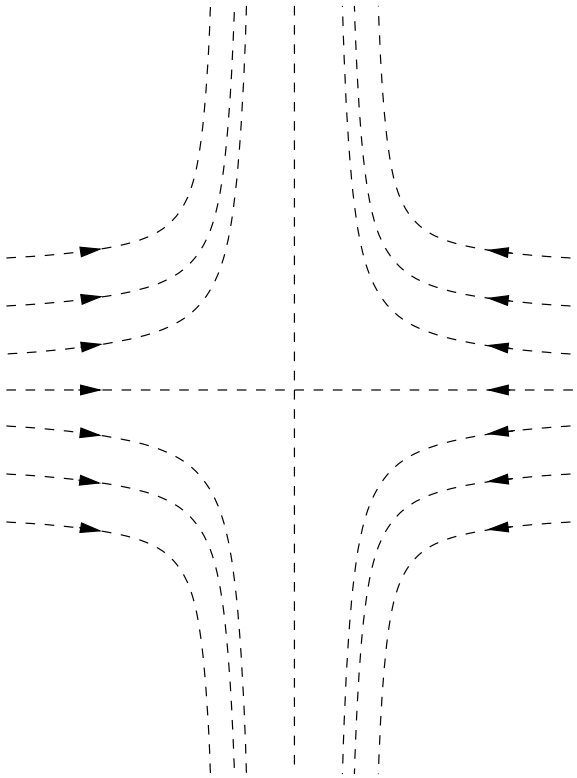

Figure 3.1: Schematic representation of a stagnation point flow.

Consider first the stagnation point flow of Figure 3.1. Regardless whether classical (2.31) or Braginskii (2.32) viscosity is considered, the viscous force can be approximated by $\nabla\cdot\mathcal{S} \simeq \nu(v_{out}/2)/(l/2)^2$. Substituting this and eliminating v_{out} and l in favour of x_s and B_s gives a quadratic equation in terms of x_s^2 (Craig and Litvinenko, 2010)

$$\eta^2 + 2\nu\eta x_s^2 = B_s^2 x_s^4.$$

Solving for x_s and taking the physically based assumption that $\eta \ll \nu < 1$ results in the scalings

$$x_s \simeq \left(\frac{\eta}{B_s}\right)^{1/2}, \tag{3.4}$$

$v_{in} \simeq \eta^{1/2}$ and $v_{out} \simeq \eta^0$. Equation (3.4) is of the same general form as the Sweet-Parker scaling (2.39); however, in contrast to a Sweet-Parker style flow where the magnetic field strength is constant in the inflow region, the stagnation point flow causes magnetic flux to pile-up at the sheet. The dissipation scalings (2.19-2.20) become

$$W_\eta \simeq \eta^{1/2} B_s^{5/2}, \qquad W_\nu \simeq \nu B_s^2. \tag{3.5}$$

Note here that the viscous dissipation scales independently of resistivity ($W_\nu \sim \eta^0$). An important consequence of this is that, for magnetic field amplitudes of order unity, we would expect viscous effects to dominate resistive effects for $\nu > \eta^{1/2}$.

Now consider a Sweet-Parker flow profile with classical viscosity, where the viscous force is given by $\nabla \cdot \mathcal{S} \simeq -\nu v_{out}/x_s^2$. Substituting this in (3.3) and again eliminating v_{out} and l gives

$$\eta^2 + 2\nu\eta = B_s^2 x_s^4.$$

In this case the second term will dominate, giving the visco-resistive scale

$$x_s \simeq (\eta\nu)^{1/4} B_s^{-1/2}, \tag{3.6}$$

$v_{in} \simeq \eta^{3/4}\nu^{-1/4}$, and $v_{out} \simeq \eta^{1/2}\nu^{-1/2}$ (Park *et al.*, 1984). The dissipation scalings (correcting a misprint in equation (20) of Craig and Litvinenko, 2010) are

$$W_\eta \simeq W_\nu \simeq \eta^{3/4}\nu^{-1/4} B_s^{5/2}. \tag{3.7}$$

Note that, due to the anisotropy of the magnetic field within the current layer, a Sweet-Parker flow profile with Braginskii viscosity would result in greatly reduced viscous dissipation (Braginskii, 1965). Obviously the dissipation would be significantly affected by the visco-resistive scale; specifically these scalings would suggest thicker current sheets and lower dissipation rates. Some studies, namely an analytical model of slow magnetic reconnection at a two-dimensional X-point (Titov and Priest, 1997) and numerical studies of X-point collapse for both classical and Braginskii viscosities (Hassam and Lambert, 1996; Craig *et al.*, 2005; Craig, 2008), have obtained this visco-resistive scale.

Two salient points have arisen from these scaling arguments. The first is the possible visco-resistive scale for Sweet-Parker style flows with classical viscosity. The second is that, for stagnation point flows, the scaling of viscous dissipation is insensitive to resistivity, and therefore likely to dominate resistive dissipation in coronal plasmas. This would suggest non-uniform plasma flows lead to viscous effects playing a significant role in solar flare energy release.

With these two points in mind, we will now discuss some of the recent exact models of steady-state viscous reconnection. We will examine their predictions for the visco-resistive scale and energy dissipation rates, with a goal of having a solid analytical base with which to compare our numerical results.

3.2.2 Sonnerup and Priest solution

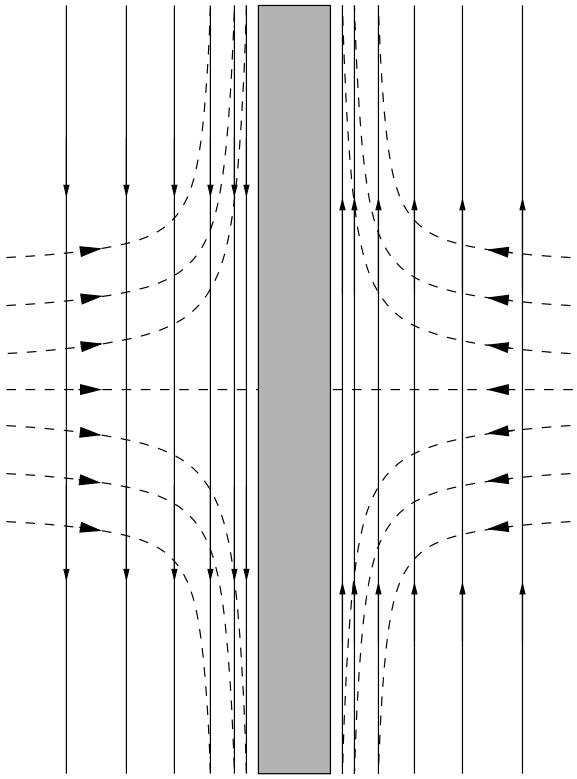

Figure 3.2: Schematic representation of the Sonnerup and Priest (1975) solution. The solid lines are the magnetic field and the dashed lines are the velocity (flow) field. Note the pile-up of the magnetic field on the edge of the current sheet.

The simplest form of the Craig and Henton (1995) solution is that in which the magnetic shear parameter $\beta = 0$, resulting in the equations of Sonnerup and Priest (1975) (see also Besser *et al.* (1990) and Jardine *et al.* (1992) for shear and vortical flow generalisations). The interesting property of the Sonnerup and Priest solution is that it holds in the presence of both classical and Braginskii viscosity (Hollweg, 1985).

A stagnation point flow advects straight field lines towards a current layer

centred on $x = 0$, as shown in Figure 3.2. The velocity profile corresponds to inwards flow along the x-axis,

$$\mathbf{v} = -\alpha x\hat{\mathbf{x}} + \alpha y\hat{\mathbf{y}}, \tag{3.8}$$

and the uni-directional magnetic field is given by

$$\mathbf{B} = \frac{E}{\eta\mu}\,\mathrm{daw}\,(\mu x)\;\hat{\mathbf{y}}. \tag{3.9}$$

We can obtain a scaling for the thickness of the current layer by considering two properties of the Dawson function (2.47). Firstly, for small s, $\mathrm{daw}(s) \simeq s$. Secondly, the Dawson function satisfies the Dawson integral

$$\frac{\mathrm{d}}{\mathrm{d}s}\left(\mathrm{daw}(s)\right) + 2s\,\mathrm{daw}(s) = 1.$$

By considering that the magnetic field maximum occurs around the edge of the current sheet we obtain $2\mu^2 x_s^2 \simeq 1$, or

$$x_s \simeq \left(\frac{\eta}{\alpha}\right)^{1/2}, \tag{3.10}$$

as the thickness of the current layer. This result implies that the inflow and outflow speeds associated with the current sheet are $v_{in} \simeq \sqrt{\alpha\eta}$ and $v_{out} \simeq \alpha$. Using equations (2.20) and (2.31) the classical viscous dissipation rate in a volume V is given by

$$W_\nu = \int \mathcal{S}_{ij}\frac{\partial v_i}{\partial x_j}\,\mathrm{d}V = 4\nu\alpha^2\,V. \tag{3.11}$$

Note that considering Braginskii viscosity (2.32) does not change the form of (3.11) beyond a factor of two reduction.

The resistive dissipation is easy to estimate if the thinness of the sheet is exploited. The current density is related to the sheet properties via $J \simeq B_s/x_s$, and we have from equation (2.19) that

$$W_\eta = \int \eta J^2\,\mathrm{d}V \simeq (\alpha\eta)^{1/2}B_s^2\,V. \tag{3.12}$$

The key aspect of these results is the presence of a single small scale x_s determined by the resistivity. Although viscous losses do occur, these arise from

maintaining the global velocity field that drives the merging. By comparing equations (3.11) and (3.12) and treating α and B_s as parameters of order unity, we see that viscous dissipation should dominate when $\nu \gg \eta^{1/2}$. More physically, if we assume (as in Sweet-Parker merging) that exhaust speeds are related to the strength of the current layer, it follows that $\alpha \simeq B_s$ (Litvinenko and Craig, 2000), and so

$$\frac{W_\nu}{W_\eta} \simeq \frac{4}{B_s^{1/2}} \frac{\nu}{\eta^{1/2}}, \tag{3.13}$$

We note that, as predicted by the stagnation point flow scaling arguments of Section 3.2.1, there is no visco-resistive scale present. Nor does it emerge in the more recent solutions for classical viscosity with non-zero β described by Craig and Litvinenko (2012).

Recently exact solutions for different flow profiles have been found for Braginskii viscosity in both two and three dimensions - we discuss them next.

3.2.3 Litvinenko Braginskii viscosity solution

Analogous to Craig and Henton (1995), Litvinenko (2005) looked for a solution, in the case of the Braginskii viscosity tensor (2.32), of the form $\mathbf{B} = B(x)\,\hat{\mathbf{y}}$, where $B(x) = -\psi'(x)$. As E is a constant and the right hand side of (2.42) is a function of x only, we have that the Poisson bracket

$$[\psi,\, \phi] = \psi' \frac{\partial \phi}{\partial y},$$

must be a function of x, and therefore $\partial_y \phi = f(x)$. This gives

$$\phi = y f(x) + g(x), \tag{3.14}$$

where $g(x)$ is a function to be determined. Substituting equations (2.42) and (3.14) into equation (2.41) results in both terms on the right being zero. We are left with

$$[\nabla^2 \phi,\, \phi] = (f^{(3)} y + g^{(3)}) f - f''(f' y + g') = 0,$$

which results in two equations

$$fg^{(3)} - f''g' = 0, \tag{3.15}$$

$$ff^{(3)} - f'f'' = 0. \tag{3.16}$$

Equation (3.16) can be simplified to

$$f'' = \pm\omega^2 f,$$

where ω is constant. If we assume that no plasma crosses the y-axis ($\partial_y\phi|_{x=0} = 0$) then the only possible forms of f are (see also Craig and Henton, 1995):

$$f = Ax, \quad f = A\sin(\omega x), \quad f = A\sinh(\omega x), \tag{3.17}$$

where A is a constant of integration. Solving equation (3.15) for each of these forms gives

$$g = \frac{\gamma x^2}{2}, \quad g = \gamma\cos(\omega x), \quad g = \gamma\cosh(\omega x), \tag{3.18}$$

respectively.

Once ϕ is specified via a particular choice of f and g, the induction equation (2.42) can be solved and the magnetic field can be expressed as a quadrature. We shall examine a simple case in which we assume no plasma crosses the x-axis ($\partial_x\phi|_{y=0} = 0$), allowing us to neglect g. Obviously choosing $f = Ax$ recovers the Sonnerup and Priest (1975) solution. If we choose the second form for f with $A = \alpha/\sin(\omega)$ then we can write the velocity as

$$\mathbf{v} = -\frac{\alpha\sin(\omega x)}{\sin(\omega)}\,\hat{\mathbf{x}} + \frac{\alpha\omega y\cos(\omega x)}{\sin(\omega)}\,\hat{\mathbf{y}}. \tag{3.19}$$

Here the parameter $0 \leq \omega < \pi$ determines the velocity gradient on the inflow boundary. Note that, as $\omega \to 0$, the stagnation-point flow of Sonnerup and Priest (1975) is recovered. Substituting our flow field in the induction equation (2.42) and solving the first order ODE via an integrating factor results in

$$\mathbf{B} = \frac{E}{\eta}\exp\left(\frac{\alpha\cos(\omega x)}{\eta\omega\sin(\omega)}\right)\int_0^x \exp\left(-\frac{\alpha\cos(\omega s)}{\eta\omega\sin(\omega)}\right)\,\mathrm{d}s\,\hat{\mathbf{y}}, \tag{3.20}$$

as the form for the magnetic field.

Provided that ω does not approach π, the parameters of the current layer (namely its thickness x_s and the inflow v_{in} and outflow v_{out} speeds) and resistive dissipation are all found to scale as those in the Sonnerup and Priest (1975) solution. The viscous dissipation rate, however, follows from equations (2.19) and (2.32):

$$W_\nu = 3\nu\alpha^2 \left(\frac{2\omega^2 + \omega \sin 2\omega}{4 \sin^2 \omega} \right) V, \tag{3.21}$$

which reduces to $3\nu\alpha^2 V$ as $\omega \to 0$. Once again, assuming that $\alpha \simeq B_s$, we recover equation (3.13) within factors of order unity.

It is important to consider what happens in the case of magnetic fields perpendicular to the flow. Taking a general planar flow profile $\mathbf{v} = (X(x,y,z), Y(x,y,z), 0)$ and an axial magnetic field $\mathbf{B} = B(x,\, y,\, z)\,\hat{\mathbf{z}}$ results in a zero Braginskii viscosity tensor (2.32). This means that, unlike for classical viscosity, axial fields in the presence of Braginskii viscosity result in no viscous dissipation (Craig and Litvinenko, 2009). However, realistic merging is unlikely to be limited to a purely planar flow with axial fields. To consider this point more thoroughly, we note that a Braginskii viscosity solution has been derived in three dimensions by Craig and Litvinenko (2009). A sinusoidal velocity field of the form

$$\begin{aligned} \mathbf{v} \;=\; & \left(-\frac{\alpha \sin(\omega x)}{\sin(\omega)},\; \frac{\alpha\omega}{2\sin(\omega)} (y\cos(\omega x) + z\sin(\omega x)), \right. \\ & \left. \frac{\alpha\omega}{2\sin(\omega)} (z\cos(\omega x) - y\sin(\omega x)) \right), \end{aligned} \tag{3.22}$$

and a fan magnetic field of the form

$$\mathbf{B} = (0,\; Y(x),\; Z(x)), \tag{3.23}$$

satisfy equations (2.51-2.53) in the case of Braginskii viscosity, where Y and Z obey the conditions

$$\eta Y'' + \frac{\alpha \sin(\omega x)}{\sin(\omega)} Y' + \frac{\alpha\omega}{2\sin\omega} \left(\cos(\omega x) Y + \sin(\omega x) Z \right) \;=\; 0, \tag{3.24}$$

$$\eta Z'' + \frac{\alpha \sin(\omega x)}{\sin(\omega)} Z' + \frac{\alpha\omega}{2\sin\omega} \left(\cos(\omega x) Z - \sin(\omega x) Y \right) \;=\; 0. \tag{3.25}$$

Perhaps unsurprisingly, the dissipation scalings arising from this solution also give the relation of (3.13). We reiterate that no visco-resistive scale is evident

from this fully 3D solution of the MHD equations. This result is reinforced by the recent study of Craig and Lopez (2013) for "spine" reconnection, which found no evidence for a visco-resistive scale and likewise supports viscous dissipation dominance for realistic coronal parameter values ($W_\nu/W_\eta \simeq \nu/\eta$).

The common feature of all exact solutions we have described thus far is a stagnation point flow. As we have stated, stagnation point flows predict relation (3.1), that is viscous dissipation dominating resistive dissipation for $\nu > \eta^{1/2}$. However a different visco-resistive scale is predicted when considering a uniform Sweet-Parker style flow profile with classical viscosity. To begin to explore this issue we will now consider a simple, head-on, numerical model.

3.3 Visco-resistive simulations of magnetic reconnection

In this section we describe numerical, flow-driven, reconnection experiments using the Braginskii and classical viscosities. Typically the viscous coefficient ν will be fixed at some representative value and scalings are derived by systematically reducing the resistivity $\eta \ll \nu$. To provide a further check on the results we also will perform a "control" resistive simulation, based on the common numerical expedient of setting $\nu = \eta$. That is we would like to compare the visco-resistive reconnection scalings with those in the case $\nu = 0$ but, due to the stabilising effect of viscosity, setting $\nu = 0$ is susceptible to numerical difficulties (Von Neumann and Richtmyer, 1950; Smith, 1985). Accordingly we set $\nu = \eta$ to approximate the purely resistive case (Biskamp, 1994; Craig and Litvinenko, 2010).

The results are obtained by numerically solving equations (2.26) and (2.27), using a version of the doubly periodic code of Craig and Watson (1999), over the region $-1 \leq x,\, y \leq 1$. The use of doubly periodic geometry (where, for a function $f(x,\, y)$ on the region $-1 \leq x,\, y \leq 1$, $f(-1,\, y) = f(1,\, y),\ f(x,\, -1) = f(x,\, 1)$) removes the need for restrictive boundary conditions; simulations per-

formed using this formulation are effective at describing open geometry models of reconnection (Craig and Watson, 1999; Heerikhuisen *et al.*, 2000). Initial conditions are derived by assuming a vortical flow velocity field (clockwise in the first quadrant) given by

$$\phi(x, y, 0) = -\frac{\alpha_0}{\pi} \sin(\pi x) \sin(\pi y), \tag{3.26}$$

where $\alpha_0 > 0$ sets the amplitude of the initial flow. We assume an initial magnetic disturbance of the form

$$\psi(x, y, 0) = \frac{\beta_0}{\pi} \sin(\pi x) \sin(\pi y) + \frac{g_0}{\pi} \cos(\pi x), \tag{3.27}$$

where $g_0 > 0$ sets the amplitude of the magnetic disturbance and $\beta_0 \geq 0$ controls the level of magnetic shear in the merging. In the simplest case of head-on ($\beta_0 = 0$) reconnection, initially straight field lines, washed together by the inflow, rapidly evolve and form a well defined current layer centred on the origin. This approach is designed to give a well behaved sheet from which we can easily calculate sheet properties, such as thickness and inflow and outflow speeds. Realistic plasmas in coronal active regions are not likely to be so simple - we examine some less restrictive initial conditions in Chapter 4.

To obtain visco-resistive scalings, the parameters α_0, β_0 and ν are held fixed while η and g_0 are systematically reduced. Note that simply reducing η while keeping g_0 fixed would lead to high pressure, flux pile-up current sheets that would feed back on the flow and stall it (Rickard and Craig, 1993; Heerikhuisen *et al.*, 2000; Craig and Watson, 2000). Accordingly, g_0 is adjusted (roughly as $\eta^{1/2}$) to ensure that peak fields B_s in the reconnecting current layers have magnitudes of order unity. This allows us to obtain scalings at resistivities that are limited only by numerical resolution in the computation (the lowest values of resistivity considered here require mesh sizes $\lesssim 10^{-3}$). In practice we take $\alpha_0 = 1$ and $\nu = 0.004$ (corresponding to an active-region plasma of 6×10^6 K) and allow resistivities in the range $10^{-4.5} \leq \eta \leq 10^{-2}$. Most of

our simulations apply to head-on reconnection, $\beta_0 = 0$, but some preliminary results for sheared reconnection are given in Section 3.5.

As a final point we recall that the Braginskii viscosity tensor (2.32) cannot be applied to fields that are very weak. We therefore employ the Hosking and Marinoff (1973) form of equation (2.33) and take $\theta = 5$, corresponding to classical viscosity becoming significant for $B \lesssim 0.2$.

3.3.1 The reconnecting current sheet

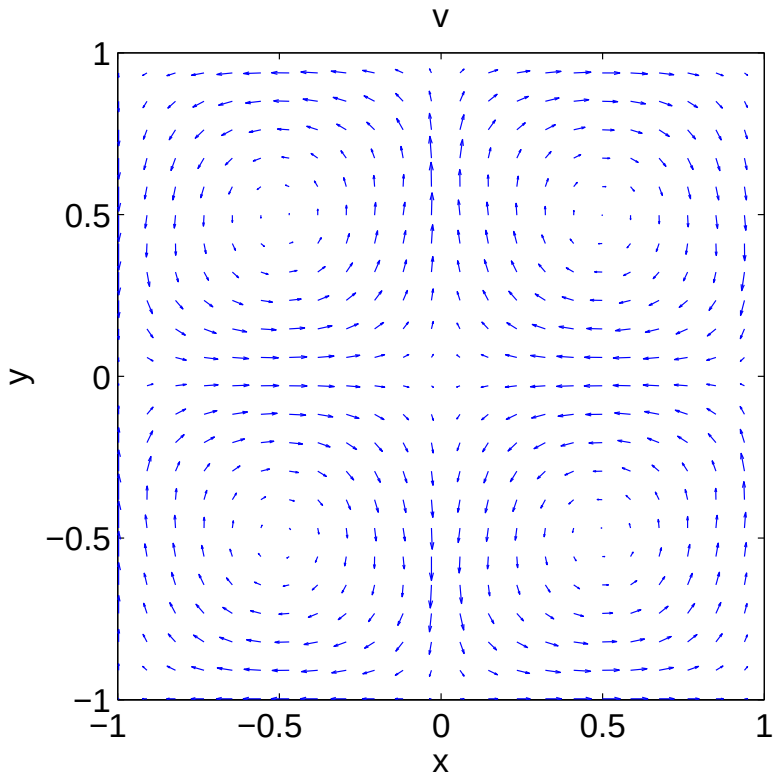

Figure 3.3: Arrow plot of **v** taken at the time of maximum current density at the origin. The parameters are $\alpha_0 = 1$, $\beta_0 = 0$ and $\eta = \nu = 0.004$. For visual clarity only some selected velocity vectors are displayed.

As an illustrative example of a typical simulation we consider a head-on Braginskii viscosity simulation with parameters $\alpha_0 = 1$, $\beta_0 = 0$ and $\eta = \nu = 0.004$. The initial velocity field of equation (3.26) creates global vortical flows (Figure 3.3) that push magnetic flux towards the origin along the x axis. The initially weak current density, as given by equation (3.27), builds up to a strong

current sheet aligned to the y axis (Figure 3.4) after approximately one Alfvén time in the present simulation.

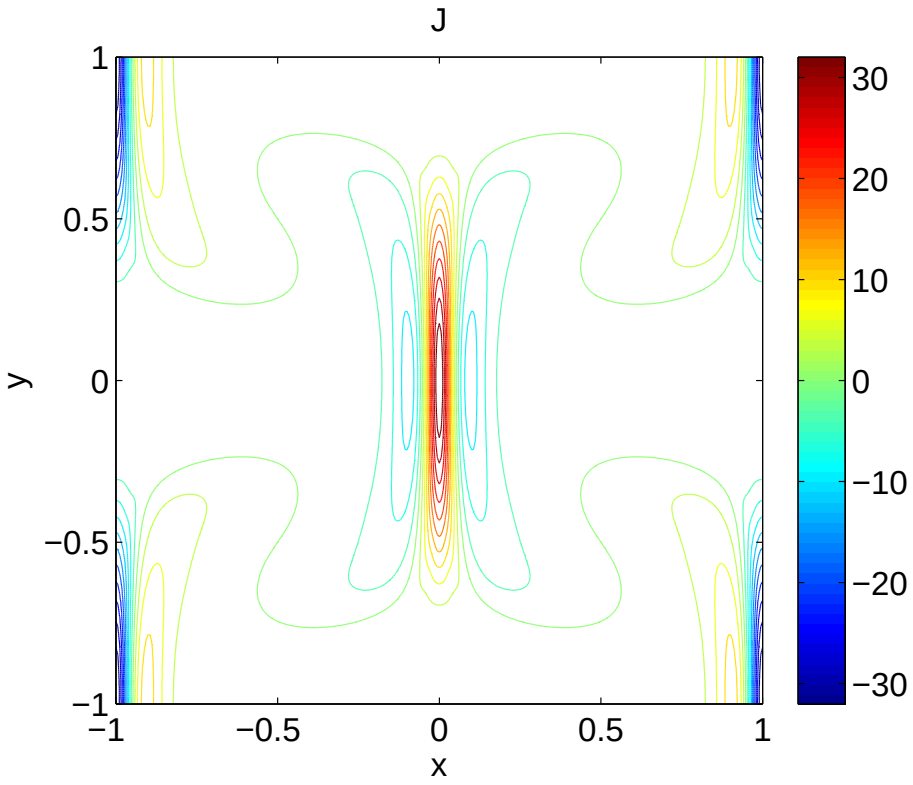

Figure 3.4: Contour plot of J taken at the time of maximum current density at the origin. The parameters are the same as in Figure 3.3, namely $\alpha_0 = 1$, $\beta_0 = 0$ and $\eta = \nu = 0.004$.

There is a good deal of analytical (Heerikhuisen and Craig, 2004) and numerical (DeLuca and Craig, 1992; Craig and Watson, 1999; Heerikhuisen *et al.*, 2000) evidence to suggest that the properties of the current layer, when taken at the time of maximum current, can be accurately described by the steady merging models such as those discussed in Section 3.2.

More specifically, suppose we use the fields displayed in Figures 3.3 and 3.4 to evaluate the rate of flux transfer E and the inflow velocity amplitude α_0. We can then compare one of our analytical models of Section 3.2, based on these parameters, alongside a slice of the simulated current sheet.

Figure 3.5 displays such a simulated slice at current maximum slice alongside the Sonnerup and Priest (1975) head-on analytical solution (3.9). Despite the fact that this model is for a steady-state plasma in an open topology, we

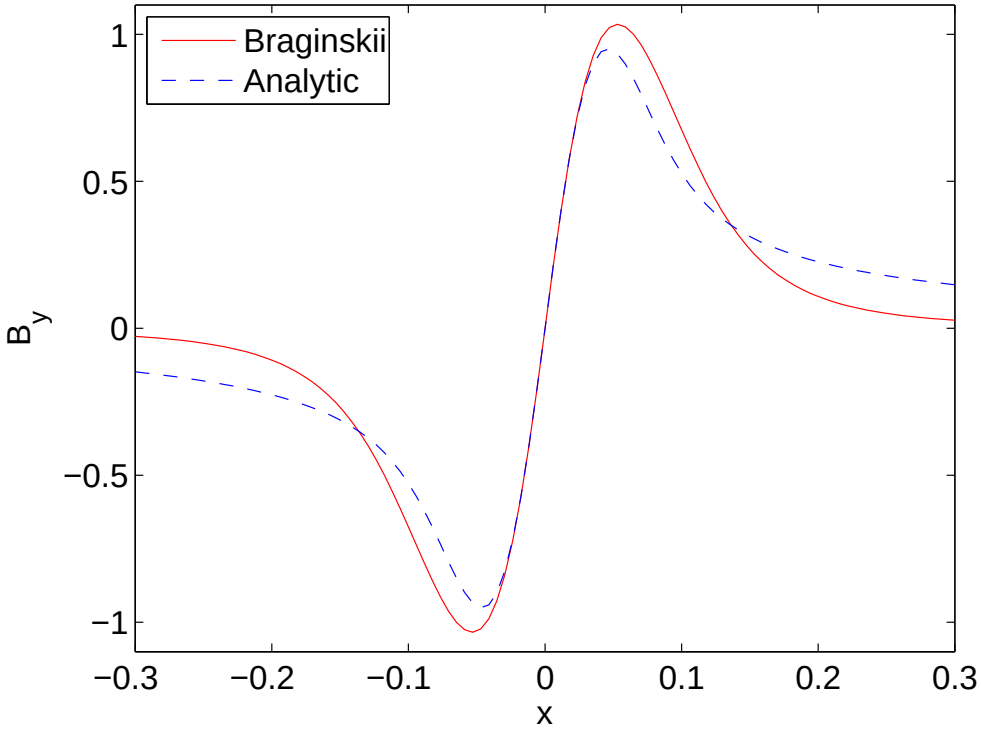

Figure 3.5: The y-component of the magnetic field in the current layer in the case of head-on merging. The parameters are the same as in Figures 3.3 and 3.4. The solid line is the numerical magnetic field and the dashed line is the analytical solution from (3.9).

see that a good representation of the dynamically evolved field in the current layer is achieved. The most obvious variations occur in the outer regions dominated by the large-scale vortical flows–the regions not accurately represented by the analytic, stagnation point flow model of (3.9). The implication is that viscosity simulations are unlikely to undermine the form of the purely resistive current layer.

3.4 Head-on magnetic merging simulations

We now turn to quantifying the key parameters v_{out}, v_{in}, and x_s of the current layer, and relating these to the global Ohmic and viscous energy release rates. As shown in Figure 3.6, where current density J is shown along the x and y axes, current sheet thickness is measured along the x axis at the level of half

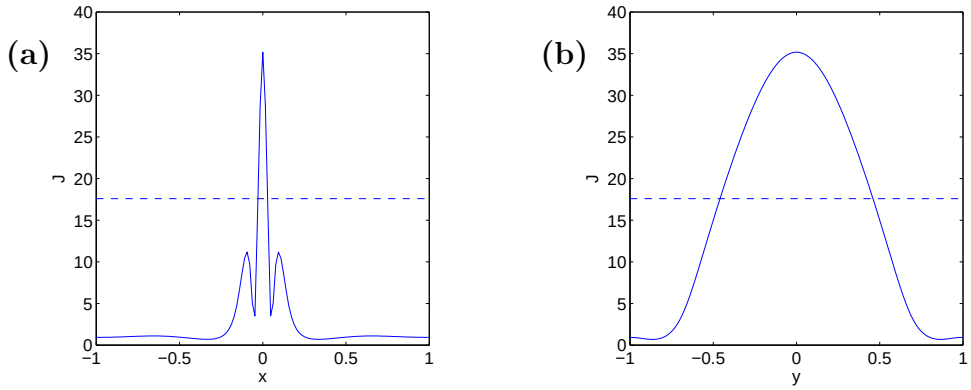

Figure 3.6: Current density along the x (a) and y (b) axes. The dashed line shows the level of half current maximum. Inflow and outflow speeds v_{in} and v_{out} are measured where the lines intersect in panels (a) and (b) respectively. Current sheet thickness x_s is measured between the two points of intersection in panel (a). The parameters are the same as in Figures 3.3 and 3.4.

current maximum. Inflow and outflow velocities are measured on the x and y axes respectively at the current half maximum level. Figure 3.7 shows a comparison of the classical, Braginskii and $\nu = \eta$ control current sheet outflow speeds, calculated at the time of maximum current. Minor variations are apparent, and the outflow is generally slower in the case of the classical viscosity, yet the outflow speeds vary by less than a factor of two over a 2.5 order of magnitude change in η. In particular there is no evidence for a slowdown, $v_{out} \sim \eta^{1/2}\nu^{-1/2}$, which would be caused by a visco-resistive scale in the case of a Sweet-Parker flow profile with classical viscosity (Section 3.2.1). The analytical scalings of Section 3.2.2 are clearly more accurate. As a general point, the slowing of the outflows by viscosity in the $\eta \ll \nu$ regime (when compared to the purely resistive case) is reinforced by observations of sub-Alfvénic flare outflows (e.g. McKenzie and Hudson, 1999; McKenzie, 2000; Asai *et al.*, 2004).

The scale of $\eta^{1/2}$ for the inflow speeds v_{in} and the current sheet thickness x_s is confirmed by the plots in Figure 3.8. In both cases it is very difficult to distinguish the Braginskii, classical and $\nu = \eta$ control plots. The classical shear viscosity provides the thickest current layer but the effect is marginal. This should be contrasted with the visco-resistive scale $x_s \sim (\eta\nu)^{1/4}$, which

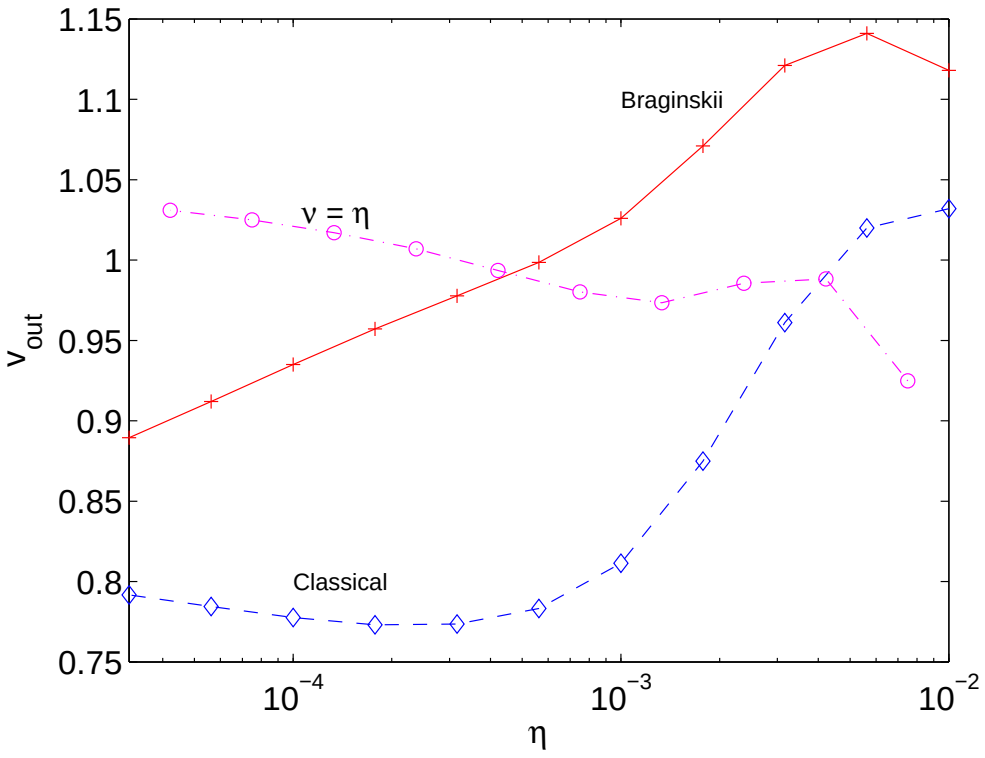

Figure 3.7: Current sheet outflow speed comparisons. Crosses, diamonds and circles refer to Braginskii, classical and $\nu = \eta$ control results respectively. The parameters are $\alpha_0 = 1$ and $\beta_0 = 0$; $\nu = 0.004$ for classical and Braginskii viscosity.

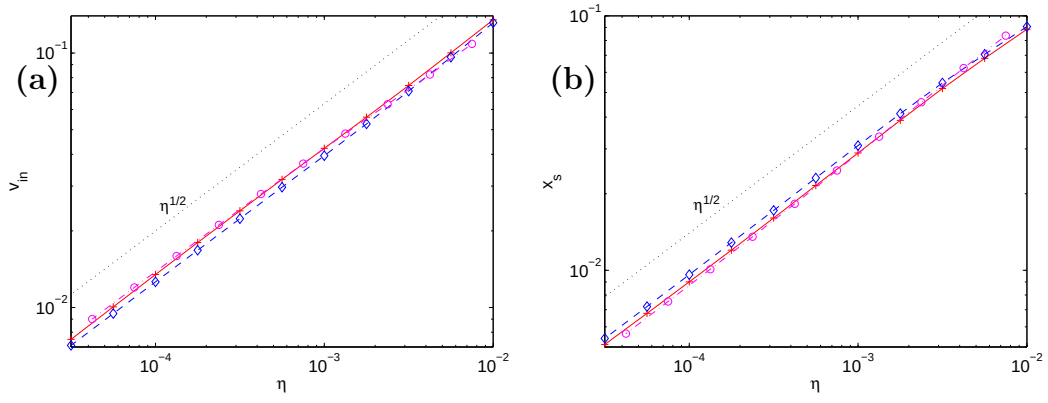

Figure 3.8: Current sheet inflow speed (a) and thickness (b) comparisons. Crosses, diamonds and circles refer to Braginskii, classical and $\nu = \eta$ control results respectively. The parameters are $\alpha_0 = 1$ and $\beta_0 = 0$; $\nu = 0.004$ for classical and Braginskii viscosity. The dotted line shows the predicted $\eta^{1/2}$ scaling.

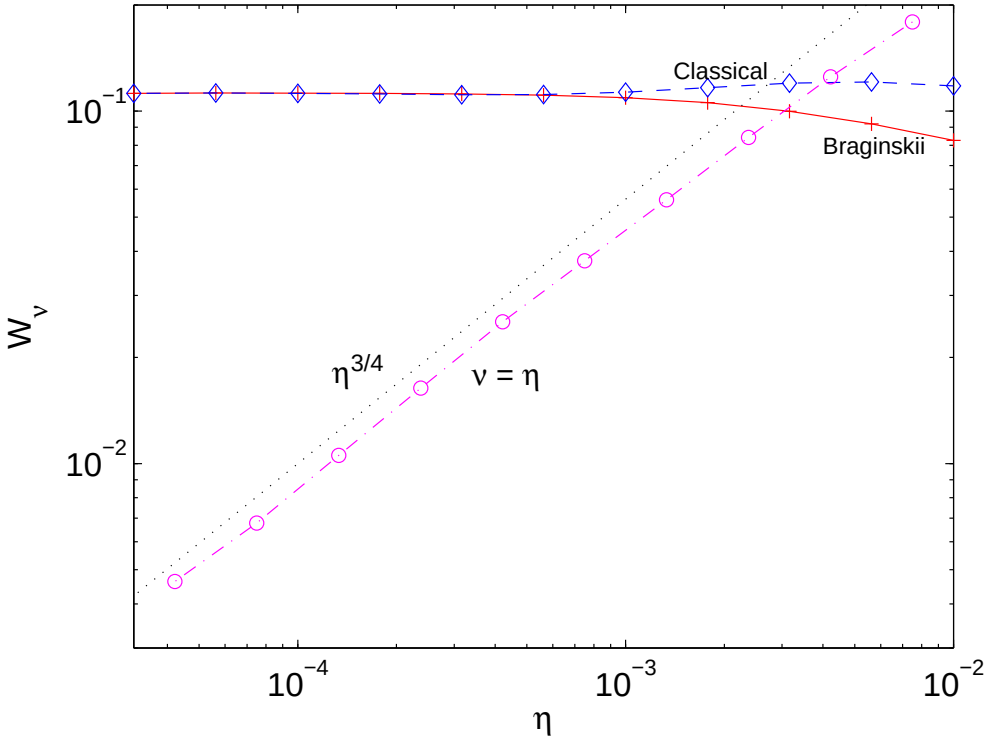

Figure 3.9: Viscous dissipation rate comparisons. Crosses, diamonds and circles refer to Braginskii, classical and $\nu = \eta$ control results respectively. The dotted line shows the $W_\nu \sim \eta^{3/4}$ scaling. The parameters are $\alpha_0 = 1$ and $\beta_0 = 0$; $\nu = 0.004$ for classical and Braginskii viscosity.

follows from Sweet-Parker style arguments with a uniform flow profile.

The relation $x_s \sim \eta^{1/2}$ for the sheet thickness, coupled to the constraint $B_s \simeq 1$, leads to flux transfer and Ohmic dissipation rates which also follow the $\eta^{1/2}$ trend. These scalings are confirmed numerically for all three regimes (the $\nu = \eta$ control, the classical and Braginskii viscosities).

More interesting is the behaviour of the global viscous losses W_ν. As indicated in Figure 3.9, the Braginskii and classical viscous losses are effectively invariant but the $\nu = \eta$ control strongly decreases with η. While the scaling arguments and exact models of Section 3.2 suggest that we might expect to see a scaling of $W_\nu \sim \eta$ for the control case, our results show a greater rate of $W_\nu \sim \eta^{3/4}$.

This increased rate is due to the enhanced sensitivity of the control calculation to sheet magnetic fields approaching or exceeding unity, known as

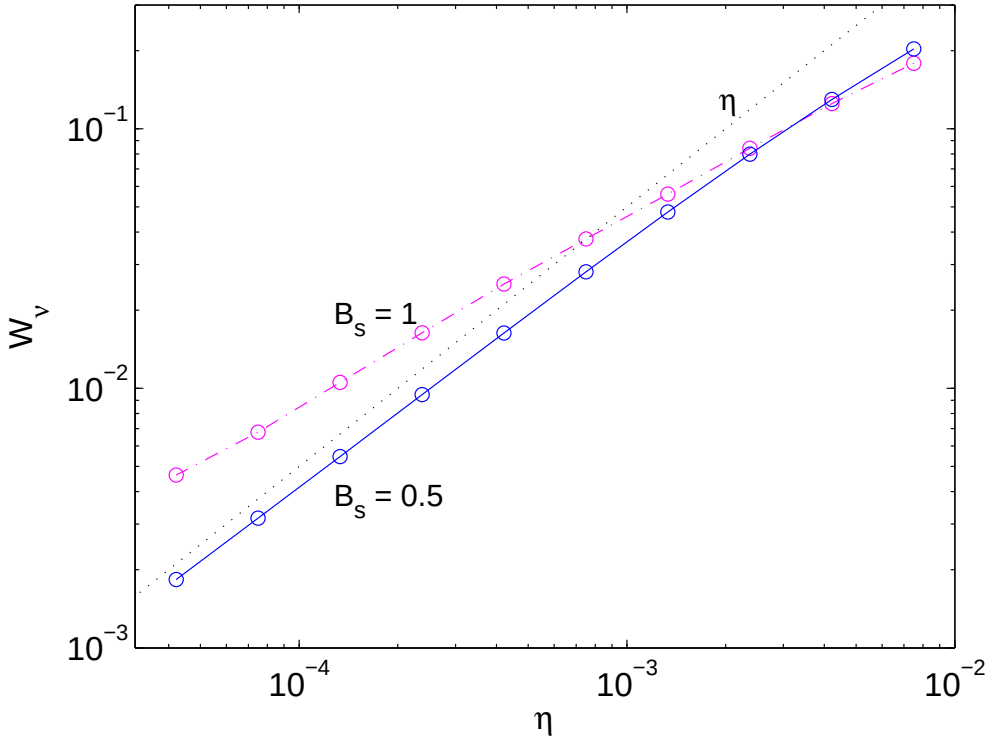

Figure 3.10: Viscous dissipation rate scalings, in the control case, for peak sheet magnetic fields of $B_s = 0.5$ (solid line) and $B_s = 1$ (dot-dashed line). The dotted line shows the $W_\nu \sim \eta$ scaling. The parameters are $\alpha_0 = 1$ and $\beta_0 = 0$.

"saturation" of the current layer. Recall that, to achieve optimal resistive dissipation rates, the simulations of Figures 3.7-3.9 have g_0 tuned so that $B_s \simeq 1$ at the time of measurement. Figure 3.10 shows viscous dissipation in the control case for the previous simulations ($B_s \simeq 1$) along with a set of runs with a weaker peak magnetic field ($B_s \simeq 0.5$). Obviously the weaker magnetic field runs recover the expected $W_\nu \sim \eta$ scaling. The $B_s \simeq 1$ case, however, has high current layer pressures that are likely stalling the flow (Heerikhuisen *et al.*, 2000), allowing more energy to be drawn from the velocity field. We point out that other properties of the control current layer scale as predicted by the exact models of Section 3.2; $v_{out} \sim \eta^0$ (Figure 3.7), $v_{in} \sim x_s \sim \eta^{1/2}$ (Figure 3.8) and $W_\eta \sim \eta^{1/2}$ (not pictured). The interesting point is that our results suggest that saturated current layers can result in increased viscous dissipation. We explore the effect of saturation of the current layer in more detail in Section

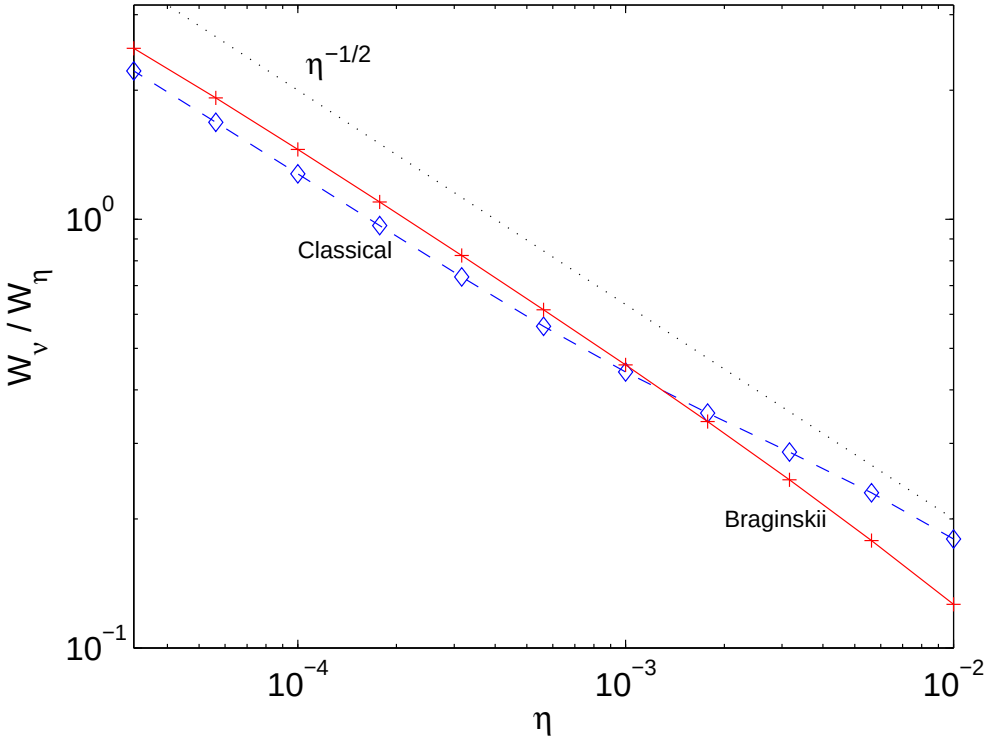

Figure 3.11: The ratio W_ν/W_η for classical (diamonds) and Braginskii (crosses) viscosity. The dotted line shows $\eta^{-1/2}$ scaling. The parameters are $\alpha_0 = 1$, $\beta_0 = 0$ and $\nu = 0.004$.

4.3.

Figure 3.11 plots the ratio of the viscous and resistive energy dissipation rates W_ν/W_η. As anticipated by equation (3.1) in the case of fixed ν, W_ν/W_η scales as $\eta^{1/2}$ as η is reduced. We see that, independent of the form of the viscosity, W_ν exceeds W_η by almost a factor of two at the lowest resistivity levels $\eta \leq 10^{-4}$.

In summary, all the resistive scalings presented in this section appear consistent with the simple analytical models of Sections 3.2.2 and 3.2.3. That is, for the flow-driven reconnection simulations considered here, the resistive scaling laws are effectively identical for both the Braginskii and classical viscosities. The limited role of the Sweet-Parker flow profile scaling arguments (Park *et al.*, 1984) should be emphasised - there is no sign of a visco-resistive scale (3.6). Although they provide a reliable description of the reconnecting current sheet in a non-viscous ($\nu = \eta$) plasma, they do not give a valid descrip-

tion of magnetic reconnection in a viscous plasma in the present flow-driven simulations.

3.5 Sheared reconnection simulations

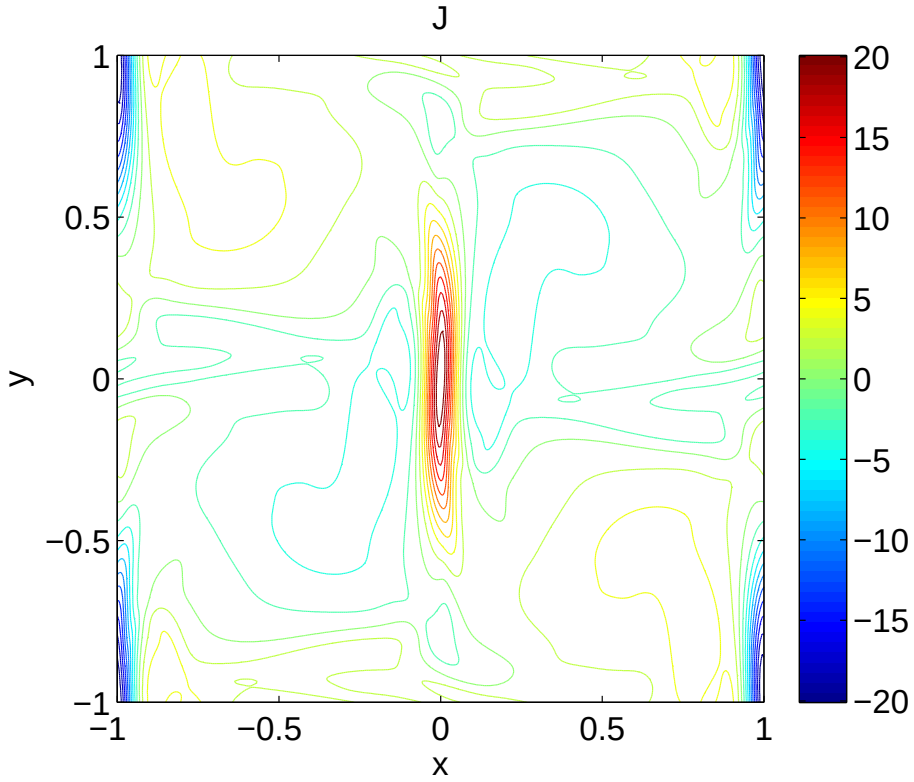

Figure 3.12: Current contour plot for sheared reconnection in the Braginskii case at time of maximum current density at the origin. The parameters are $\alpha_0 = 1$, $\beta_0 = 0.7$, $\eta = 0.004$, and $\nu = 0.004$.

Guided by the exact resistive solutions of Craig and Henton (1995) we might expect that, compared with the head-on case, visco-resistive reconnection of sheared magnetic field lines should occur in thicker current sheets, which would lead to reduced Ohmic energy dissipation and flux transfer rates. Figure 3.12 shows the current contour plot for a typical Braginskii run with a high value of shear ($\beta_0 = 0.7$). As in the head-on case there is a well defined current sheet in the vicinity of the magnetic null, but there is now significant warping of the ends of the sheet.

Our numerical results show that, even with relatively high levels of shear-

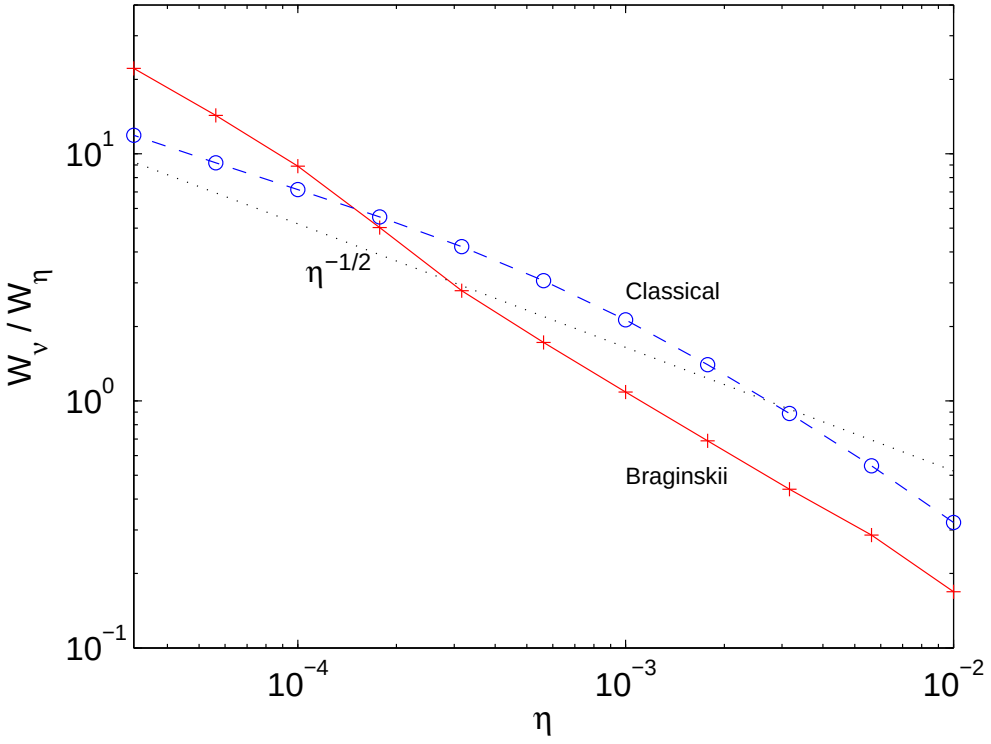

Figure 3.13: The ratio W_ν/W_η for classical (diamonds) and Braginskii (crosses) viscosity. The dotted line shows $\eta^{-1/2}$ scaling. The parameters are $\alpha_0 = 1$, $\beta_0 = 0.7$ and $\nu = 0.004$.

ing, the classical viscosity results essentially follow the same scalings as in the head-on case ($x_s \sim \eta^{1/2}$, $W_\eta \sim \eta^{1/2}$, $W_\nu \sim \eta^0$). Systematic deviations, however, appear in the case of the Braginskii viscosity for high levels of shearing. These deviations from the analytical predictions imply that the structure of the current sheet is significantly modified by the anisotropic Braginskii viscous forces when the reconnecting magnetic field lines are strongly sheared.

Figure 3.13 illustrates the main new effect of strong magnetic shear (cf. Figure 3.11). It shows W_ν/W_η for the classical and Braginskii viscosities in the case $\beta_0 = 0.7$. For the classical viscosity both the resistive dissipation rate W_η and the viscous dissipation rate W_ν agree with the analytical arguments, leading to equation (3.13). The ratio W_ν/W_η for the Braginskii viscosity, however, appears to follow a different scaling (closer to η^{-1}). Figure 3.14 confirms that this deviation is due to a slow down in the resistive dissipation rate (this scales closer to η rather than $\eta^{1/2}$) in the strongly sheared Braginskii

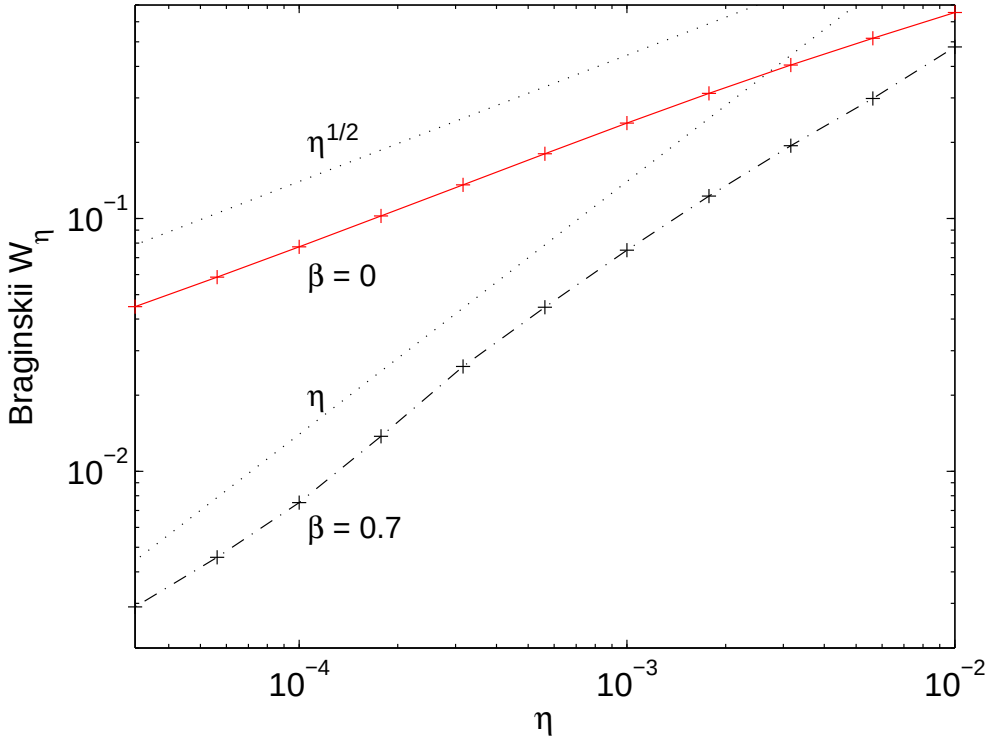

Figure 3.14: Comparison of Braginskii viscosity resistive dissipation W_η for head-on ($\beta = 0$) and highly sheared ($\beta = 0.7$). The dotted lines shows $\eta^{-1/2}$ and η scalings. The parameters are $\alpha_0 = 1$ and $\nu = 0.004$.

simulation.

3.6 Discussion and conclusions

Both analytical and numerical studies suggest that viscous dissipation may be capable of dominating resistive dissipation under a wide variety of coronal conditions (Hollweg, 1986; Litvinenko, 2005; Craig and Litvinenko, 2009). However studies of magnetic reconnection in a resistive viscous plasma lead to contradictory results. Analytical solutions (Park *et al.*, 1984; Titov and Priest, 1997) predict the formation of a current layer on the visco-resistive scale $\sim (\eta\nu)^{1/4}$, with corresponding energy dissipation rates $W_\eta \simeq W_\nu \simeq \eta^{3/4}\nu^{-1/4}B_s^{5/2}$. Crucially these arguments assume a Sweet-Parker style uniform flow profile. Numerical simulations in a tokamak geometry (Park *et al.*, 1984) and for X-point collapse (Craig *et al.*, 2005; Craig, 2010) support this

scale.

However, analytic arguments based on a stagnation point flow profile (Craig and Litvinenko, 2010) and numerical simulations involving large scale stagnation point flows in 3D (Craig and Litvinenko, 2009) result in scalings similar to Sweet-Parker, $W_\eta \simeq \eta^{1/2} B_s^{5/2}$ and $W_\nu \simeq \nu B_s^2$. Significantly these scalings predict that viscous dissipation would exceed resistive dissipation for $\nu \gg \eta^{1/2}$.

In this chapter we attempted to clarify the issue by performing numerical simulations of planar magnetic reconnection in doubly periodic geometry. We considered head-on reconnection, driven by large-scale vortical flows in an incompressible plasma. We used both the classical shear viscosity and the Braginskii form for the ion parallel viscosity in a magnetised plasma. Somewhat surprisingly, our numerical results show that the parameters of the reconnecting current sheet (its thickness, the inflow and outflow speeds) are accurately described by simple analytical scalings of flux pile-up magnetic merging, regardless of the form of the viscous stress tensor. The computed global resistive and viscous energy dissipation rates also closely follow the relation

$$\frac{W_\nu}{W_\eta} \sim \frac{\nu}{B_s^{1/2} \eta^{1/2}},$$

confirming that the current sheet thickness is effectively independent of viscosity for both the classical and Braginskii forms.

We have also made a preliminary study of the properties of the reconnection region in the case of a strong magnetic shear. It appears that in the Braginskii case magnetic shearing can modify the dissipation scalings, implying that the properties of the reconnecting current sheet depend on the form of the viscosity.

To summarise, we find no evidence of the visco-resistive scale $\sim (\eta\nu)^{1/4}$ or its corresponding energy release rate scalings in our simulations of planar, head-on, magnetic reconnection in doubly periodic geometry. This finding contrasts sharply with predictions of some steady analytical models, Sweet–Parker style scaling arguments, and time-dependent simulations in a closed X-point geometry. There appears to be no simple criterion for the emergence of the visco-resistive scale.

Our results may be partly due to there not being enough time for the visco-resistive scale to develop: we took the current sheet parameters at the time of the first current maximum (first implosion), and it may be that the scale would develop after several implosions (Craig *et al.*, 2005). However, as in excess of fifty percent of the available energy can be dissipated due to the first implosion (Craig, 2008), it seems unlikely that the visco-resistive scale will have significant bearing on explosive flare energy release rates.

The idealised nature of the simulations in this chapter are a useful starting point for our analysis of solar flare energy release. However, realistic coronal plasma interactions are unlikely to conform to such simple head-on symmetrical configurations. With this in mind we turn to simulations in a less restrictive environment.

Chapter 4

Visco-resistive dissipation driven by the Orszag-Tang vortex

4.1 Introduction

Coronal active regions are typically highly non-uniform and unlikely to conform to such idealised models as those presented in the previous chapters. The purpose of this chapter is to study the effect of viscosity on reconnection in a more general simulation framework. In particular, using a less restrictive initial condition than in the previous chapter, we will calculate viscous (W_ν) and resistive (W_η) dissipation rates and discuss the implications of our results for solar flare energy release.

In Section 3.2 we outlined the analytically based relation

$$\frac{W_\nu}{W_\eta} \sim \frac{\nu}{B_s^{1/2}\eta^{1/2}}, \tag{4.1}$$

which holds for stagnation point flow profiles with both Braginskii and classical forms of the viscosity (Craig and Litvinenko, 2010). Since the viscosity coefficient ν exceeds the resistivity η by approximately ten orders of magnitude in coronal plasmas we would expect that the viscous energy dissipation rate W_ν should dominate the resistive dissipation rate W_η. Global stagnation

point flows that support localized current layers are generic components in all exact current sheet reconnection solutions, no matter whether 2D (Craig and Henton, 1995) or 3D "fan" solutions (Craig and Fabling, 1996) are considered.

However, as the above relation was derived assuming "head-on" reconnection in an "open geometry" (Craig and Litvinenko, 2010), it cannot be expected to apply universally. It could break down, for instance, in 3D "spine" reconnection, where resistive losses occur in quasi-cylindrical current tubes as opposed to current sheets (Craig and Fabling, 1996). Furthermore, analytical and numerical studies (e.g. Park *et al.*, 1984; Craig *et al.*, 2005; Craig, 2008; Craig and Lopez, 2013) have found a visco-resistive current sheet thickness scale $x_s \simeq (\eta\nu)^{1/4} B_s^{-1/2}$ that would change the scaling above to $W_\nu \simeq W_\eta \simeq \eta^{3/4}\nu^{-1/4} B_s^{5/2}$.

A further area of interest is the effect of "saturation". As was pointed out in Section 3.3, saturation occurs when the strength of the current layer is so great that it feeds back on the driving flow (Rickard and Craig, 1993; Heerikhuisen *et al.*, 2000). The simulations of the previous chapter varied the strength of the initial field to keep the sheet right on the edge of saturation, thereby ensuring optimal resistive dissipation rates. This provided a limit to relation (4.1) for head-on reconnection that is conservative in terms of viscous losses. However, realistic active region plasmas are unlikely to have the properties of the current layer so closely matched to external parameters and could be prone to saturated effects. In particular it is reasonable to expect that the slowing of the driving flow by saturation would increase viscous dissipation. Indeed, in the control ($\nu = \eta$) simulation of Section 3.4, we have found potential evidence of this.

To explore the above issues we choose, in the simulations of this chapter, more general initial conditions that do not have prior assumed symmetries, with the goal of achieving more physically plausible results. We shall employ the same incompressible planar simulation framework as Chapter 3 but instead take as the initial condition a modified Orszag–Tang vortex (Orszag and Tang,

1979; Biskamp and Welter, 1989). The Orszag–Tang vortex is well used in the study of MHD turbulence (e.g. Dahlburg and Picone, 1989; Parashar *et al.*, 2009) and for validating numerical schemes (e.g. Zachary *et al.*, 1994; Ryu *et al.*, 1995).

The structure of this chapter is as follows. In Section 4.2, by adjusting the strength of the magnetic field to match the properties of the external driving, we examine the applicability of (4.1) in the case of optimal resistive dissipation ($B_s \simeq 1$). This is conservative in terms of viscous dissipation and therefore will provide a robust test of (4.1). We examine first a control ($\nu = \eta$) simulation in Section 4.2.1 to provide a check on our diagnostics. Then in Section 4.2.2 we perform classical and Braginskii viscosity simulations to examine (4.1) in this more general Orszag–Tang vortex formulation.

In Section 4.3 we turn to the question of saturation. Realistic current sheets are unlikely to have their properties strongly matched to the external driving. We therefore no longer carefully tune the initial conditions to provide optimal reconnection rates; instead we let the sheet saturate ($B_s > 1$) as resistivity is reduced and examine dissipation rates. A control ($\nu = \eta$) simulation is performed in Section 4.3.1 and full classical and Braginskii viscosity saturated simulations are performed in Section 4.3.2. Our conclusions are summarised in Section 4.4.

4.2 Optimal reconnection rates

Our goal in this section, while trying to maximise resistive dissipation, is to calculate visco-resistive dissipation rates and therefore check the validity of equation (4.1) using a more general set of initial conditions than in Section 3.3.

We employ the same doubly periodic code as in Chapter 3 but here our initial conditions are based on a modified version of the Orszag and Tang (1979)

vortex (e.g. Biskamp, 1993a; Biskamp, 1993b; Heerikhuisen *et al.*, 2000)

$$\phi(x,y) = \frac{1}{2\pi}\left[\cos(\pi x + 1.4) + \cos(\pi y + 0.5)\right], \tag{4.2}$$

$$\psi(x,y) = \frac{g_0}{2\pi}\left[\cos(2\pi x + 2.3) + \cos(\pi y + 4.8)\right], \tag{4.3}$$

where the phase numbers have no particular significance other than to break the initial symmetries (Biskamp and Welter, 1989); we have chosen them to mirror the inviscid calculation of Heerikhuisen *et al.* (2000).

Analogous to equation (3.27), $g_0 > 0$ is regarded as an external driving parameter which sets the amplitude of the initial magnetic field. As in Section 3.3, g_0 is scaled (roughly as $\eta^{1/2}$) to give peak magnetic field strengths B_s of order unity. This allows us to examine equation (4.1) in the limiting case of near-maximal resistive dissipation.

Figure 4.1 shows the initial current density (panel a) and the current density (b), magnetic flux (c) and velocity field (d) at the time of maximum current for a typical run based on classical viscosity ($\eta = 10^{-4}, \nu = 0.004$, and $g_0 = 0.05$). The peak current density of $J \approx 103.3$ is achieved at $t \approx 2.819$. We see that well defined current sheets, supported by large-scale vortical flows, are generated between magnetic island regions. That large-scale shearing flows are needed to support localized current layers is a common feature of similar models (as detailed by Biskamp, 1994; Heerikhuisen *et al.*, 2000). No qualitative differences were observed when similar runs were performed using Braginskii viscosity, in good accordance with the viscous, stagnation point flow profile models of Section 3.2. Note that this is in contrast to the X-point, line-tied, 2.5-dimensional study of Craig and Litvinenko (2007), which found significant differences between the two viscosities. In this study peak viscous dissipation for Braginskii viscosity, while still physically significant, was lower and took longer to occur than for classical viscosity. As we pointed out in Section 3.2.3, magnetic fields normal to the flow can strongly affect Braginskii viscous dissipation. As we do not consider axial fields in our 2D formulation, and considering the exact solutions of Section 3.2, we therefore might not expect to find significant differences in our results between the two forms of viscosity.

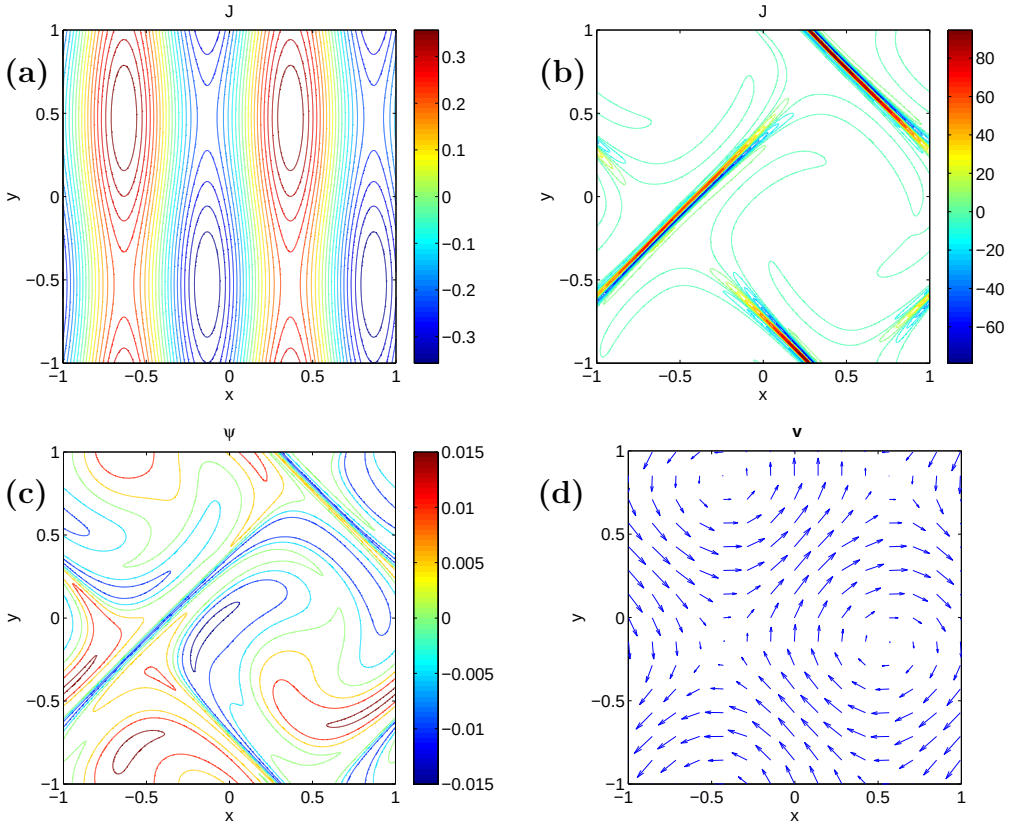

Figure 4.1: Typical classical viscosity simulation. Panel (a) shows a contour plot of current density for the initial distribution ($t = 0$), and (b), (c), and (d) show the current density, magnetic flux, and velocity field at the time of maximum current ($t = 2.819$) respectively. Both the magnetic and the velocity field amplitudes are of order unity. The parameters are $\eta = 10^{-4}, \nu = 0.004$, and $g_0 = 0.05$. Each spatial unit corresponds to a length scale l_c.

To extract dissipation rates consistently over our range of resistivity we run simulations over several Alfv́en times and compute time averages of W_η and W_ν. We again exploit the fact that current layer properties around the time of maximum current provide a good model of steady-state reconnection scalings, such as those described in Section 3.2 (see Figure 3.5). In practice we average dissipation rates over an interval of one Alfvén time, centred about the peak resistive dissipation. Figure 4.2 shows a time plot of the dissipation rates for the simulation of Figure 4.1 ($\eta = 10^{-4}, \nu = 0.004, g_0 = 0.05$), along with the global energy (2.29) $\mathcal{E} = \int (v^2/2 + B^2/2)\, \mathrm{d}V$. The averaging interval is indicated by the vertical dashed lines.

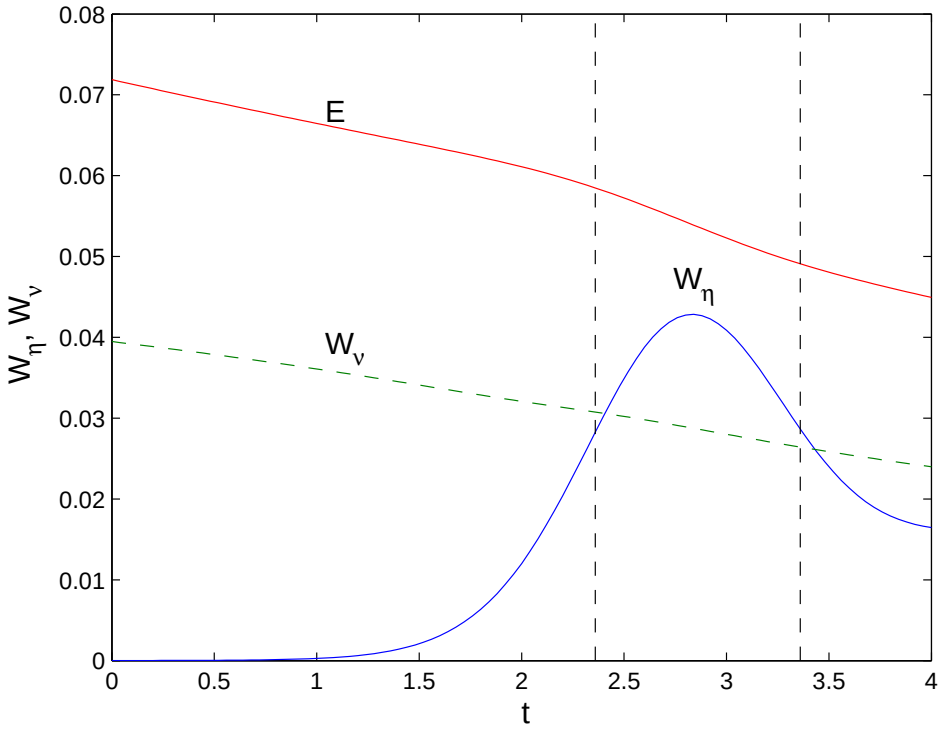

Figure 4.2: Temporal evolution of viscous and resistive dissipation rates in the case of classical viscosity, along with global energy $\mathcal{E} = \int (v^2/2 + B^2/2)\, \mathrm{d}V$ (divided by seven for comparison). Parameters are the same as Figure 4.1 ($\eta = 10^{-4},\ \nu = 0.004,\ g_0 = 0.05$). The vertical dashed lines show the interval over which the average is calculated.

4.2.1 Dissipation scalings for $\nu = \eta$

As a preliminary check on our diagnostics we perform a series of control simulations by setting $\nu = \eta$ for classical viscosity. Since the system is now controlled by a single small parameter η the computed Ohmic dissipation rate should fall within the compass of the resistive scaling law

$$W_\eta \simeq \eta^{1/2}\, B_s^{5/2}. \tag{4.4}$$

Recall that the range of resistivities which can be modelled is limited by numerical resolution - the mesh sizes are $\lesssim 10^{-3}$ for the resistivities approaching $\eta = 10^{-4.5}$. It should be remembered, however, that as we are trying to achieve maximal reconnection rates, the amplitude g_0 of the initial field is adjusted (roughly as $\eta^{1/2}$) to ensure that localized current sheets with peak fields

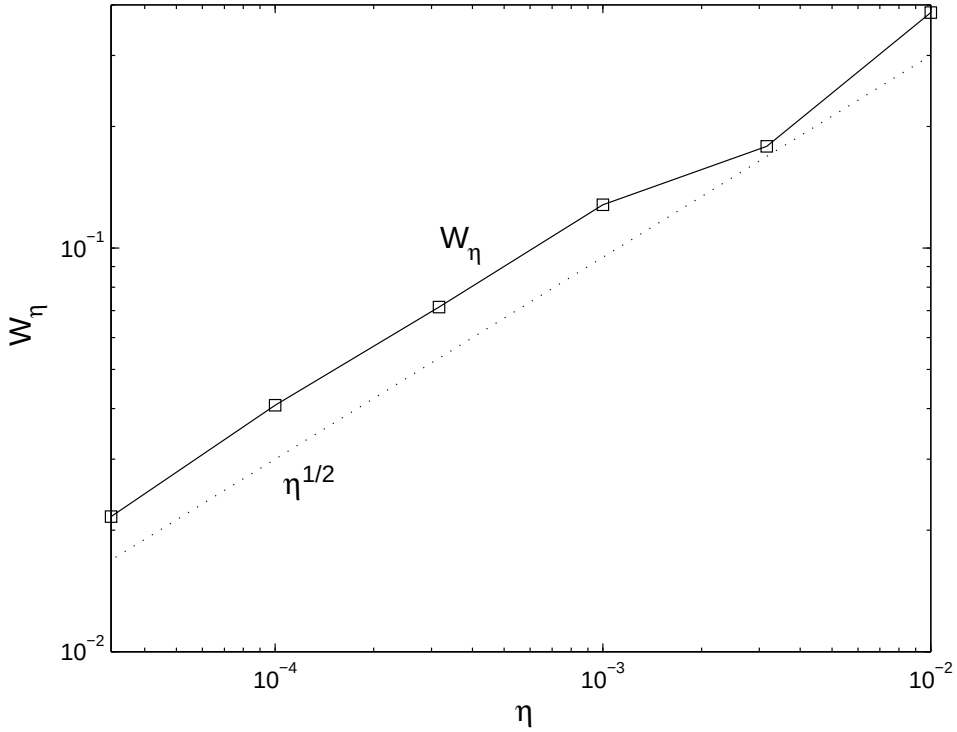

Figure 4.3: Resistive dissipation rate for the $\nu = \eta$ control case. The dotted line shows $\eta^{1/2}$ scaling.

$B_s \simeq 1$ are consistently achieved. With this understanding, the numerical results can be extrapolated to arbitrarily small η without inhibiting the current localization. Figure 4.3, showing the resistive dissipation rate scaling as $\sim \eta^{1/2}$, thus confirms that reconnection occurs via flux pile-up current layers in accordance with the scaling law derived in Section 3.2. Note that an increase in the control viscous dissipation rate, similar to the control simulation of Section 3.4, was seen for saturating current layers. As expected, the $W_\nu \simeq \eta$ scaling was recovered when the initial field amplitude g_0 was reduced to give unsaturated sheets. This reinforces our finding in Section 3.4 - that saturation can result in increased viscous dissipation.

4.2.2 Classical and Braginskii viscosity scalings

Consider now viscous dissipation. In the case of head-on reconnection, with a stagnation point flow profile, the viscous dissipation scales as $W_\nu \approx \nu v_m^2$,

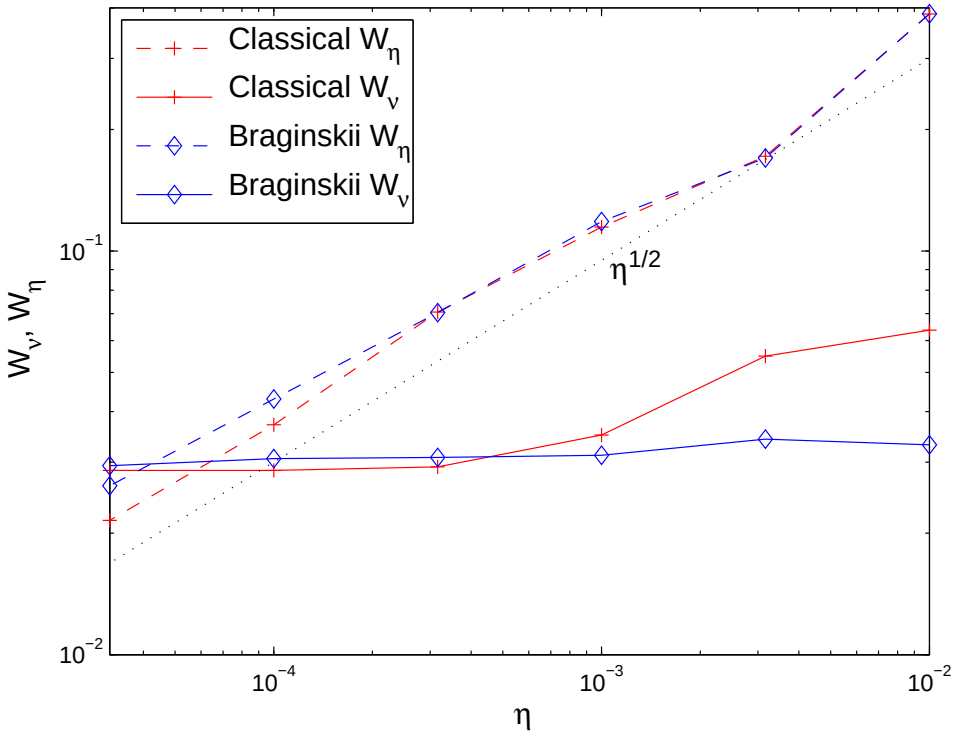

Figure 4.4: Viscous and resistive dissipation rates for classical (crosses) and Braginskii (diamonds) viscosity. The dotted line shows $\eta^{1/2}$ scaling. The viscosity parameter is $\nu = 0.004$.

where v_m is the amplitude of the velocity field (Craig and Litvinenko, 2010). Since reconnection models require Alfv́enic flow amplitudes we can identify $v_m \approx v_A \approx B_s$, and so

$$W_\nu \approx \nu\, B_s^2 \tag{4.5}$$

defines the global viscous dissipation. Combining equations (4.4) and (4.5), and taking $B_s \approx 1$, leads to the scaling law (4.1).

With this in mind we turn to the behaviour of the system when the viscosity coefficient is fixed but the resistivity is systematically reduced from $\eta = 10^{-2}$ to $\eta = 10^{-4.5}$. We take $\nu = 0.004$, corresponding to an active region plasma of $T_c = 6 \times 10^6\,\mathrm{K}$, in all of the results that follow.

Figure 4.4 highlights the weakening resistive losses for both classical and Braginskii viscosity. A key feature is the domination of the viscous losses over the weakening resistive losses for $\eta < 10^{-4}$. As anticipated by equation

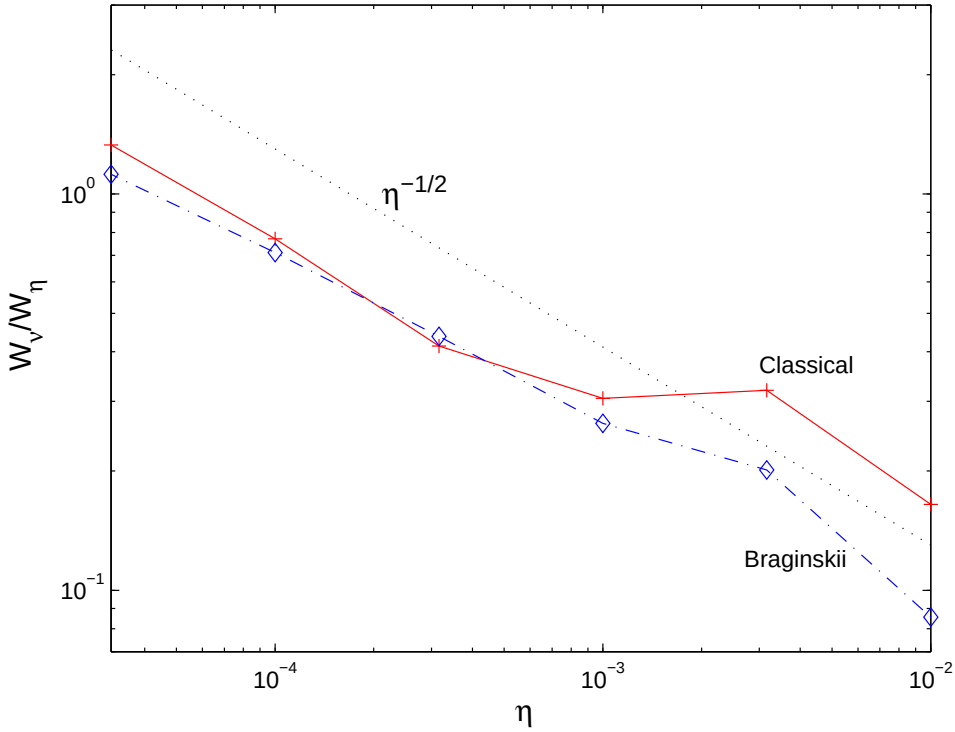

Figure 4.5: The ratio W_ν/W_η for classical (crosses) and Braginskii (diamonds) viscosity. The dotted line shows the asymptotic, predicted, $\eta^{-1/2}$ scaling. The viscosity parameter is $\nu = 0.004$.

(4.5), the viscous dissipation is effectively constant despite reductions in the resistivity.

The global Braginskii losses in the asymptotic regime ($\eta < 10^{-3}$) are slightly increased when compared to classical losses, but the overall trend is identical. We speculate that the slightly higher Ohmic losses in the case of Braginskii viscosity (namely $W_\eta \sim \eta^{0.44}$ for $\eta < 10^{-3}$) may be due to the stronger driving required to maintain $B_s \approx 1$. These results are clearly predicted by the exact solutions outlined in Section 3.2, and reinforce the point that viscous damping is likely to play a major role in energetic events such as the solar flare.

Finally, in Figure 4.5, we plot side by side resistive scalings for the ratio W_ν/W_η for both classical and Braginskii viscosities. It is clear that for sufficiently small η, in both cases, this ratio approximates the $\eta^{-1/2}$ scaling predicted by equation (4.1). Notably, the results are very similar in the asymp-

totic regime $\eta < 10^{-3}$: namely the ratio W_ν/W_η scales as $\eta^{-0.51}$ and $\eta^{-0.42}$ for classical and Braginskii viscosities respectively.

4.3 Saturated visco-resistive dissipation rates

In contrast to the simulations of the previous section, where the driving parameter g_0 was "tuned" to provide optimal Ohmic dissipation rates and explore energy dissipation scalings, in this section we keep g_0 fixed. The rationale behind this is that realistic coronal active region plasmas are highly dynamic, and the strength of the driving, at least in transient reconnection models, is unlikely to be strongly tuned to the properties of the current sheet.

Our present aim, therefore, is to investigate the resistive and viscous losses in strongly driven "saturated" current layers, in which the energy losses can be severely influenced by the stalling of the reconnection rate (Heerikhuisen *et al.*, 2000). This effect has been observed in simulations of coalescence of magnetic islands (Biskamp and Welter, 1980) - high magnetic pressure in the current layer can reverse the inwards flow of plasma, creating an oscillatory 'tidal' motion. As reconnection requires inwards flow of plasma to occur, we would expect to see a drop in resistive dissipation for strongly driven current layers. However, due to the feedback on the driving flow, we might expect to see a corresponding increase in our viscous dissipation rate. Recall we have seen evidence to support this in the head-on control cases of Sections 3.4 and 4.2.1.

4.3.1 The resistive control computation

We start by setting $\nu = \eta$ to establish a control, and examine resistive dissipation rates. Classical viscosity is assumed and the magnetic driving amplitude g_0 is held fixed.

As we have previously discussed, the resistive system evolves from the initial configuration of equations (4.2) and (4.3) into a periodic array of well

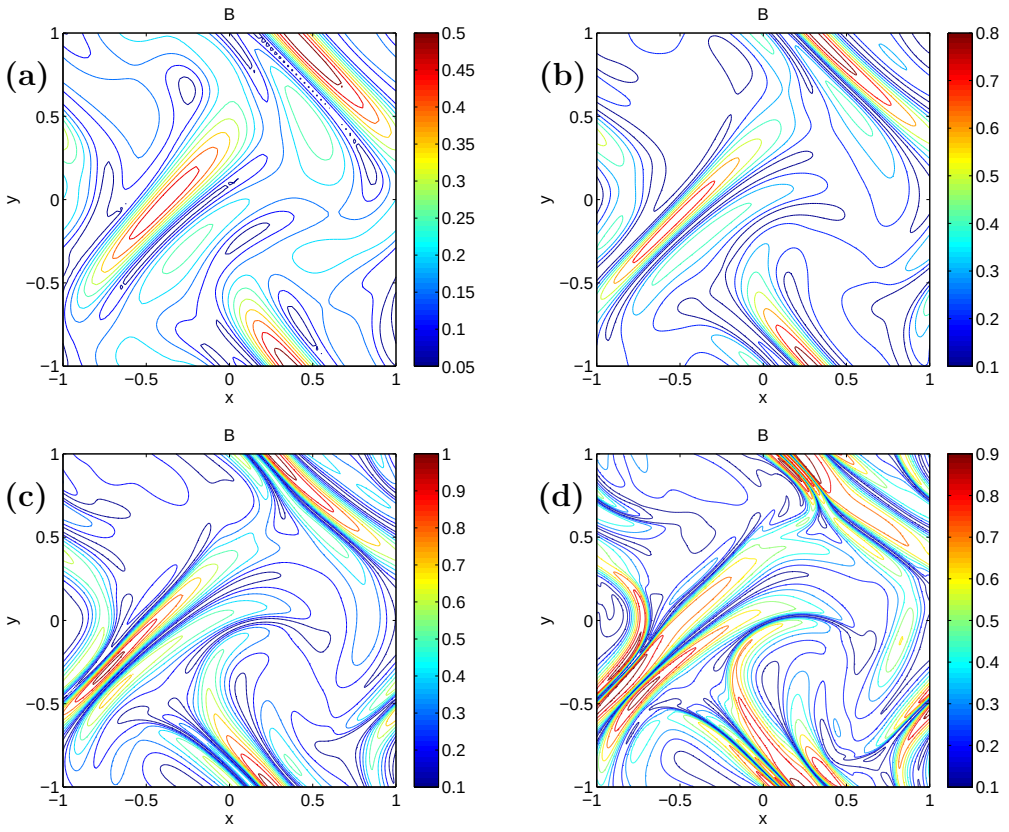

Figure 4.6: Magnetic field intensity $|\mathbf{B}|$ around the time of current maximum for $\eta = 10^{-2}$ (a), $\eta = 10^{-2.5}$ (b), $\eta = 10^{-3}$ (c) and $\eta = 10^{-3.5}$ (d). As η decreases the current layers become increasingly well defined. The magnetic driving parameter is $g_0 = 0.3$.

defined current layers. Figure 4.6 shows magnetic field intensity around the time of current maximum for $\eta = 10^{-2}$ (a), $\eta = 10^{-2.5}$ (b), $\eta = 10^{-3}$ (c) and $\eta = 10^{-3.5}$ (d). As resistivity reduces, the current layers become increasingly well defined as typified by panels (a) and (b). However, for the lower resistivities of panels (c) and (d), we start to see the effects of saturation. In panel (d) significant warping of the current layer is apparent, along with strong flux pile-up at the edge of the sheet.

A main concern is the behaviour with resistivity of the Ohmic dissipation rate for a typical current sheet. Figure 4.7 shows the Ohmic rate W_η plotted against resistivity for the driving amplitude $g_0 = 0.3$, along with the peak current sheet magnetic field B_s. Three distinct resistive regimes, predicted by the flux pile-up models of Section 3.2, are separated by the vertical dashed

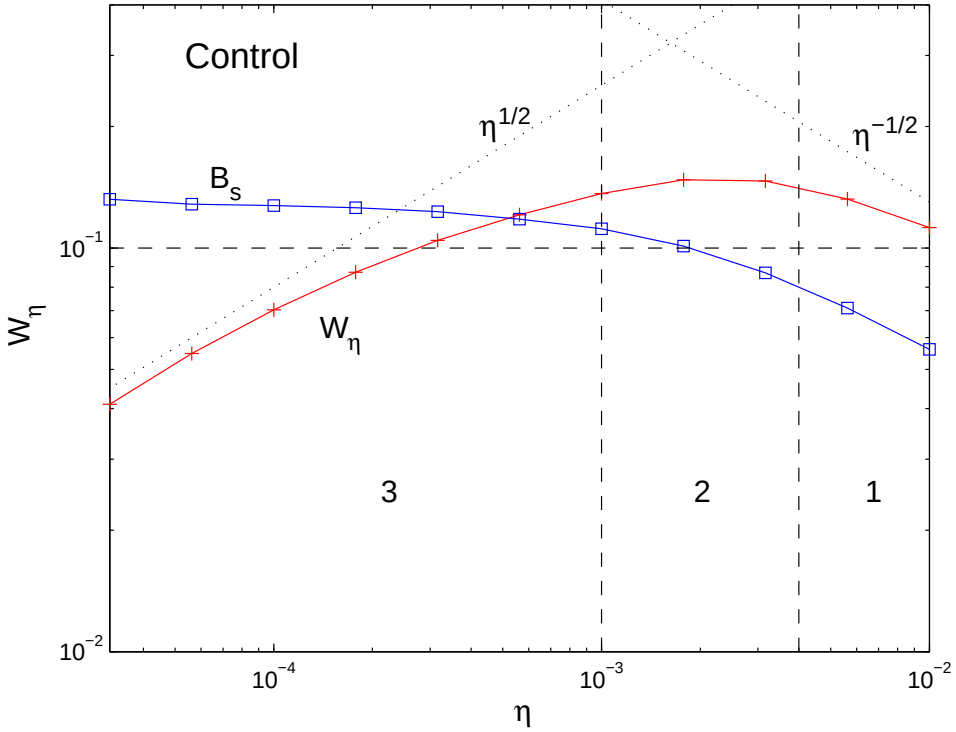

Figure 4.7: Resistive dissipation rate (W_η) for the $\nu = \eta$ control case (classical viscosity), along with peak magnetic field (B_s - divided by ten for comparison). The driving amplitude parameter is $g_0 = 0.3$. The dotted lines show saturated ($\eta^{1/2}$) and pre-saturation ($\eta^{-1/2}$) dissipation scalings. The three regions, separated by the vertical dashed lines, indicate the pre-saturation (1), optimal reconnection (2) and saturation (3) regimes. The horizontal dashed line indicates $B_s = 1$.

lines.

In regime (1), when η is sufficiently large and $B_s < 1$, the current sheet strengthens with reductions in η and the sheet thickness x_s systematically reduces ($x_s \sim \eta^{1/2}$). This behaviour leads to an Ohmic dissipation rate that builds up roughly as $\eta^{-1/2}$.

In regime (2) the amplitude of the field in the current layer begins to saturate ($B_s = 1$). Saturation occurs when the field amplitude in the sheet becomes comparable to the external hydromagnetic pressures driving the merging. This occurs for $\eta \simeq 10^{-3}$ at the present level of driving ($g_0 = 0.3$) and corresponds to a peak in the Ohmic dissipation rate. By choosing a smaller driving parameter g_0 the "fast" scaling of $W_\eta \sim \eta^{-1/2}$ (regime (1)) can be extended, in which

case the maximum reconnection rate occurs at progressively lower values of η. However, the maximum "saturated" dissipation rate of regime (2), as given by equation (4.4), always exists for any sensible choice of the driving parameter g_0.

Finally, in regime (3), when the field amplitude is fully saturated ($B_s > 1$), the dissipation rate falls off as $W_\eta \sim \eta^{1/2}$ as the resistivity is further reduced. The increasing current density is now solely due to the thinning of the current layer and significant warping of the sheet is observed (Figure 4.6, panel (d)).

It should be noted that equation (4.4) does not imply that the merging can be described by Sweet-Parker modelling (Section 2.4.1). Although the dissipation rate $W_\eta \sim \eta^{1/2}$ mimics the Sweet-Parker rate–at least when the flux pile-up factor B_s is ignored–the flow topology outside the current layer is highly non-uniform and therefore prone to viscous losses on a global scale. These additional losses are not represented realistically in the control simulation due to the constraint $\nu = \eta$.

Finally we stress that, although regimes (1) and (2) are generally well described by existing analytic reconnection models, the fully saturated regime (3) is rather poorly understood. Saturation is repeatedly witnessed computationally, for instance during coalescence merging (Biskamp and Welter, 1980), and may well involve chaotic behaviour (Craig and Watson, 1999). With this in mind we turn our attention to whether complications arising from saturation affect the dissipation scalings of the current layer.

4.3.2 Resistive versus viscous energy dissipation

We now repeat the control simulation of Section 4.3.1, but fix the viscous coefficient ν as well as the driving parameter g_0. It is important to contrast this approach with that of Section 4.2, where we "tuned" g_0 (roughly as $\eta^{1/2}$) to maintain optimal Ohmic dissipation rates across the range of resistivities. That is, to avoid saturation as η is reduced, increasingly weak fields were washed into the reconnection regions to keep the simulation on the edge of

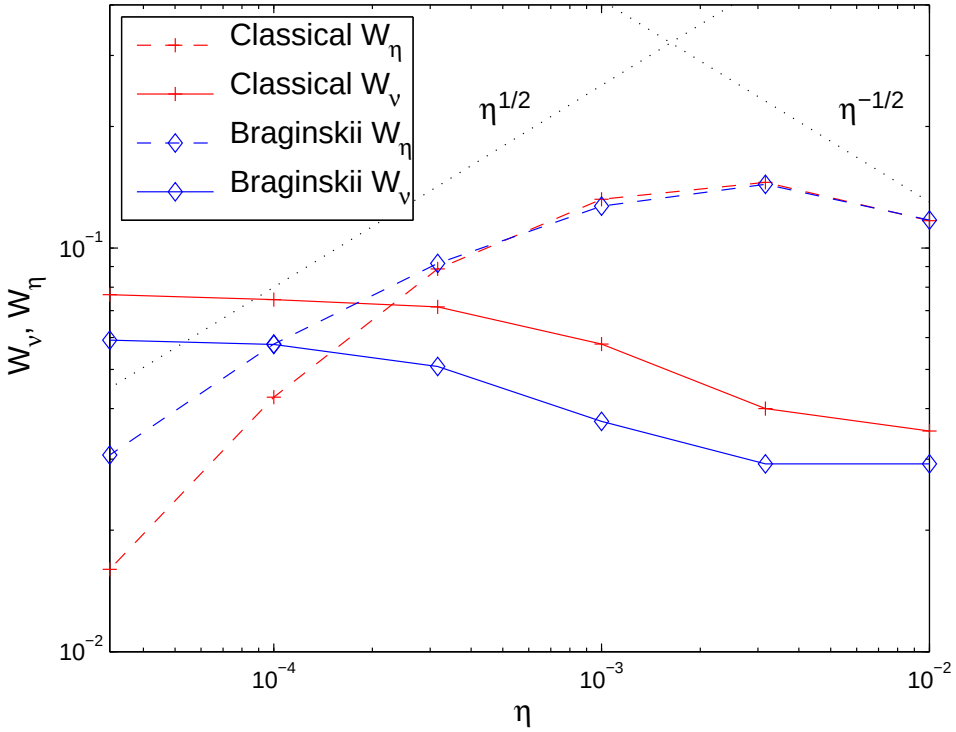

Figure 4.8: Viscous and resistive dissipation rates for classical (crosses) and Braginskii (diamonds) viscosity. The dotted lines show saturated ($\eta^{1/2}$) and pre-saturation ($\eta^{-1/2}$) scalings. The viscosity parameter is $\nu = 0.004$ and the magnetic driving parameter is $g_0 = 0.3$.

saturation (regime (2)). The motivation in that case was to compare viscous losses with the maximum achievable Ohmic losses (4.4) for physically based values. In contrast, by fixing g_0, our present concern is the saturated regime (regime (3)) where resistive losses are weaker. In this case the strength of the magnetic field, external to the current layers, will be comparable to the strength of the velocity field. Due to the symmetry between the magnetic and velocity fields we would not, in general, expect one field to dominate the other. The equipartition between the fields attained by fixing g_0 therefore presents a more physically robust picture of a reconnecting environment.

Figure 4.8 shows the results of fixing the viscosity parameter at the level $\nu = 0.004$, for both classical and Braginskii viscosities. Two key observations can be made. Firstly, saturation of the sheet appears to amplify viscous dissipation compared to pre-saturation levels. This is accompanied by a slight

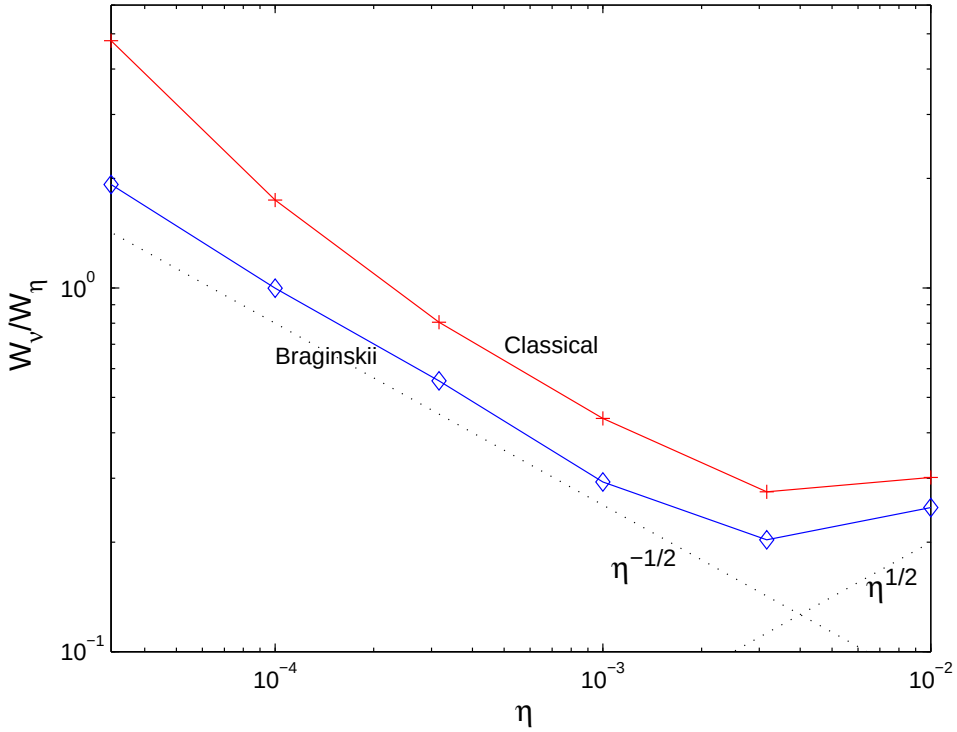

Figure 4.9: The ratio W_ν/W_η for classical (crosses) and Braginskii (diamonds) viscosity. The dotted lines show the saturated $\eta^{-1/2}$ and the pre-saturation $\eta^{1/2}$ scalings. The viscosity parameter is $\nu = 0.004$ and the magnetic driving parameter is $g_0 = 0.3$.

decrease in resistive dissipation when compared to the resistive control (Figure 4.7). We speculate that the decrease in classical W_η in the saturated regime, when compared to the Braginskii model (in which viscosity is suppressed normal to the field), is due to the increased effectiveness of classical viscosity at dissipating energy from the velocity field. Secondly, the predicted scalings of equations (4.4) and (4.5) provide a reasonable guide to the dissipation scalings even when the current sheet is fully saturated.

This behaviour is reinforced in Figure 4.9, where side by side scalings are plotted for the ratio W_ν/W_η for both forms of viscosity. In particular, while the inclusion of large fixed viscosity causes some variation in dissipation rates, the scaling $W_\nu/W_\eta \sim \nu/\eta^{1/2}$ remains a conservative estimate as far as viscous losses are concerned. We are led to conclude that viscous losses, even in strongly driven reconnection simulations, are likely to remain robust to the

presence of saturated current layers.

4.4 Discussion and conclusions

In this chapter we have considered resistive and viscous dissipation driven by the Orszag–Tang vortex. In the present formulation, the Orszag–Tang vortex generates flux pile-up current layers controlled by three parameters, the resistive and viscous coefficients η and ν and the strength of the driving vortex g_0. The key advantage of the vortex is that it allows the system to evolve from a situation free from the assumed prior symmetries of the head-on simulations of the previous chapter.

Of central concern is the analytically-based scaling law (4.1)

$$\frac{W_\nu}{W_\eta} \approx \frac{\nu}{B_s^{1/2}\eta^{1/2}}.$$

In Section 4.2 we performed a series of simulations aimed at exploring whether the above relation holds in the limiting case where resistive dissipation is maximised by tuning the driving parameter g_0. We began by verifying that, by the customary expedient of setting $\nu = \eta$, expected Sweet-Parker scalings are recovered, namely $W_\eta \sim \eta^{1/2}$. Then, by fixing the viscosity parameter ν at a physically based level, we found that equation (4.1) holds even in the limit of maximal resistive dissipation.

It remained unclear, however, whether these scalings would be preserved in more physically realistic situations. In Section 4.3, therefore, no attempt was made to tune the driving g_0 to provide current sheets with optimal Ohmic dissipation rates. Computations performed in this way have the advantage of maintaining equipartition, that is comparable global strengths in both velocity and magnetic fields. Our results therefore extended into the saturated regime where peak fields in current sheets are naturally limited by the strength of the driving. As in Section 4.2 we obtained resistive scalings for the control case of $\nu = \eta$. It was shown that the scalings were in good agreement with the flux pile-up reconnection solutions of Section 3.2. Secondly, the results of Section

4.3.2 were obtained by fixing ν as well as the driving amplitude g_0. Once again equation (4.1) was shown to hold true in the asymptotic case $\nu \gg \eta$.

The present results suggest that the scaling of equation (4.1) is not limited to specialized symmetries or merging geometries, but is generic to all current sheet magnetic reconnection models. Our main conclusion is that the global viscous losses for both classical and Braginskii forms of the viscosity are almost invariant with resistivity, even in the presence of relatively weak reconnective merging. More physically, given that $\nu \gg \eta$ in coronal plasmas, the present analysis suggests that viscous dissipation is likely to dominate resistive dissipation in dynamic active-region plasmas where Alfvénic vortical flows are expected.

It is important to underline the distinction between traditional models of energy release and the viscous picture we have presented. Much of the focus of traditional models has been on finding a "fast" resistive dissipation rate to release energy on the short flare time scales ($\sim 100\,\mathrm{s}$), with little attention paid to viscous effects. In our model fast energy dissipation comes from viscosity acting on the large scale, non-uniform, velocity fields supporting the reconnection. Magnetic energy is transferred to the velocity field and dissipated via viscosity, while also dissipating via resistive effects at a slower ($W_\eta \sim \eta^{1/2}$) rate. The key point is that global viscous losses can easily account for a significant fraction of the flare energy budget on flare time scales.

This concludes the reconnection part of this thesis. We have studied visco-resistive energy release mechanisms which can account for substantial energy liberation from the Sun's magnetic field. One of the resultant effects of this energy release will be particle acceleration, which can occur due to the strong electric fields within current layers. In general, accelerated particle distributions are common throughout the universe – studying particle acceleration is the subject of the remainder of this thesis.

Chapter 5

Particle acceleration and transport

5.1 Introduction

Particle distributions accelerated to energies above the thermal background are a common occurrence across the universe. Synchrotron radiation is produced by strong plasma jets in radio galaxies (Burbidge, 1956), supernovae remnants are known to be a source of acceleration for cosmic-rays (Ackermann *et al.*, 2013), and the solar wind (Parker, 1958) is a constant stream of accelerated particles blown out by the Sun. Furthermore, up to a third of the energy release from a solar flare may manifest in the form of accelerated particles (Priest, 1982). Large electric fields in current layers, turbulent outflow jets and MHD shock waves all provide mechanisms for particle acceleration due to flare events (Priest and Forbes, 2000).

Our goal in this chapter is to describe the Fokker-Planck stochastic approach to modelling non-relativistic particle acceleration and transport. To this end we employ the Fokker-Planck equation, first derived by Adriaan Fokker and Max Planck (Fokker, 1914). This second order partial differential equation, which models both advective and diffusive transport effects, can also be found in areas as diverse as population dynamics (Goudon and Saad,

1998) and financial modelling (Friedrich *et al.*, 2000). One of the advantages of the Fokker-Planck approach is that it allows multiple numerical and analytical avenues for extracting information. A key technique which we shall use is the expression of the Fokker-Planck equation as a system of stochastic differential equations (Itô, 1944, 1951).

The structure of this chapter is as follows. In Section 5.2 we outline the derivation of the Fokker-Planck equation and state the form of the equation we shall use. We show how the Fokker-Planck equation can be written as a system of stochastic equations in Section 5.3, and examine the equivalence of the Fokker-Planck and stochastic formulations using numerical simulations of a simple model of particle transport in Section 5.4. In Section 5.5, as an illustrative application, we consider the scattering of electrons by Coulomb collisions in flare loops. Section 5.6 contains our summary.

5.2 Fokker-Planck equation

We use the Fokker-Planck equation for our study of particle acceleration. It describes the time evolution of a distribution function. We shall outline the derivation of the general Fokker-Planck equation below, but first we briefly discuss phase space and distribution functions.

To explore the evolution of a system of particles we need to track their position and momentum. We therefore work in "phase space", this being the six dimensional space consisting of all possible position ($\mathbf{x}$) and momentum ($\mathbf{p}$) values. A distribution function gives the probability that a random variable of a system takes on a given value. For example, consider the particle number phase space distribution function $f_0(\mathbf{x}, \mathbf{p}, t)$, which gives the number of particles at a phase space point ($\mathbf{x},\ \mathbf{p}$) at time t. The total number of particles n in the system at a time t is found by integrating the distribution function over position and momentum

$$n(t) = \int_{\mathbf{p}} \int_{\mathbf{x}} f_0(\mathbf{x},\, \mathbf{p},\, t)\ \mathrm{d}^3\mathbf{x}\ \mathrm{d}^3\mathbf{p}.$$

The initial distribution function is therefore normalised via

$$n(t=0) = \int_{\mathbf{p}} \int_{\mathbf{x}} f_0(\mathbf{x},\, \mathbf{p},\, t=0)\ \mathrm{d}^3\mathbf{x}\ \mathrm{d}^3\mathbf{p}. \tag{5.1}$$

Expressions for mean values (moments) of different quantities of the model can be easily expressed. For example, in Cartesian coordinates, the mean of the momentum in the x direction p_x is

$$\langle p_x \rangle = \frac{1}{n} \int_{\mathbf{p}} \int_{\mathbf{x}} p_x f_0\ \mathrm{d}^3\mathbf{x}\ \mathrm{d}^3\mathbf{p}.$$

The Fokker-Planck equation governs the evolution of the distribution function. Following Chandrasekhar (1943) we sketch a derivation. For simplicity we assume no creation or annihilation of particles or other extra physical effects. Consider the particle number distribution function $f_0(\mathbf{x}, \mathbf{p}, t)$, describing the number of particles with mass m at a phase space point $(\mathbf{x},\, \mathbf{p})$ at time t. The number of particles at the same point a short time later $t + \Delta t$ is given by

$$\begin{aligned} f_0(\mathbf{x},\, \mathbf{p},\, t+\Delta t) \;\; = \;\; & \int_{-\infty}^{\infty} \int_{-\infty}^{\infty} f_0(\mathbf{x} - \Delta\mathbf{x}, \mathbf{p} - \Delta\mathbf{p}, t) \\ & \times P(\mathbf{x} - \Delta\mathbf{x},\, \mathbf{p} - \Delta\mathbf{p};\, \Delta\mathbf{x},\, \Delta\mathbf{p})\ \mathrm{d}\Delta\mathbf{x}\ \mathrm{d}\Delta\mathbf{p}, \end{aligned} \tag{5.2}$$

where $P(\mathbf{x} - \Delta\mathbf{x},\, \mathbf{p} - \Delta\mathbf{p};\, \Delta\mathbf{x},\, \Delta\mathbf{p})$ is the probability that a particle at position $\mathbf{x} - \Delta\mathbf{x}$ with momentum $\mathbf{p} - \Delta\mathbf{p}$ increments its position by $\Delta\mathbf{x}$ and its momentum by $\Delta\mathbf{p}$ after time Δt. For sufficiently small Δt the position increment is given by $\Delta\mathbf{x} = \partial_t \mathbf{x}\, \Delta t = \mathbf{p}\Delta t/m$ ($\mathbf{p} = m\mathbf{v}$ for non-relativistic particles). We can remove the $\Delta\mathbf{x}$ dependence from the right of equation (5.2) by means of delta functions. Using

$$P(\mathbf{x} - \Delta\mathbf{x},\, \mathbf{p} - \Delta\mathbf{p};\, \Delta\mathbf{x},\, \Delta\mathbf{p}) = P(\mathbf{x} - \Delta\mathbf{x},\, \mathbf{p} - \Delta\mathbf{p};\, \Delta\mathbf{p})\, \delta\left(\Delta\mathbf{x} - \frac{\mathbf{p}}{m}\Delta t\right),$$

we can re-write equation (5.2) as

$$\begin{aligned} f_0(\mathbf{x},\, \mathbf{p},\, t+\Delta t) \;\; = \;\; & \int_{-\infty}^{\infty} f_0\left(\mathbf{x} - \frac{\mathbf{p}}{m}\Delta t,\, \mathbf{p} - \Delta\mathbf{p},\, t\right) \\ & \times P\left(\mathbf{x} - \frac{\mathbf{p}}{m}\Delta t,\, \mathbf{p} - \Delta\mathbf{p};\, \Delta\mathbf{p}\right)\ \mathrm{d}\Delta\mathbf{p}, \end{aligned}$$

or by relabelling the $\mathbf{x}$ coordinate ($\mathbf{x} \rightarrow \mathbf{x} + \mathbf{p}\Delta t/m$),

$$f_0\left(\mathbf{x} + \frac{\mathbf{p}}{m}\Delta t,\, \mathbf{p},\, t + \Delta t\right) = \int_{-\infty}^{\infty} f_0(\mathbf{x},\, \mathbf{p} - \Delta\mathbf{p},\, t)\; P(\mathbf{x},\, \mathbf{p} - \Delta\mathbf{p};\, \Delta\mathbf{p})\; \mathrm{d}\Delta\mathbf{p}.$$

Expanding both sides in a Taylor series and using the summation convention we have

$$\begin{aligned} f_0 + \left(\frac{\partial f_0}{\partial t} + \frac{p_i}{m}\frac{\partial f_0}{\partial x_i}\right)\Delta t \;\; = \;\; & \int_{-\infty}^{\infty}\left[f_0 - \frac{\partial f_0}{\partial p_i}\Delta p_i + \frac{1}{2}\frac{\partial^2 f_0}{\partial p_i \partial p_j}\Delta p_i \Delta p_j + \ldots\right] \\ & \times\left[P - \frac{\partial P}{\partial p_i}\Delta p_i + \frac{1}{2}\frac{\partial^2 P}{\partial p_i \partial p_j}\Delta p_i \Delta p_j + \ldots\right]\mathrm{d}\Delta\mathbf{p} \\ & + O(\Delta t^2), \end{aligned} \tag{5.3}$$

where the indices $i,\, j \in \{x,\, y,\, z\}$. To simplify this we can consider the momentum change averages:

$$\langle \Delta p_i \rangle = \int_{-\infty}^{\infty} \Delta p_i\, P\; \mathrm{d}\Delta\mathbf{p}, \tag{5.4}$$

and

$$\langle \Delta p_i \Delta p_j \rangle = \int_{-\infty}^{\infty} \Delta p_i \Delta p_j\, P\; \mathrm{d}\Delta\mathbf{p}. \tag{5.5}$$

Substituting the above in equation (5.3) gives

$$\begin{aligned} \left(\frac{\partial f_0}{\partial t} + \frac{p_i}{m}\frac{\partial f_0}{\partial x_i}\right)\Delta t \;\; = \;\; & -\frac{\partial}{\partial p_i}\left(\langle \Delta p_i \rangle f_0\right) + \frac{1}{2}\frac{\partial^2}{\partial p_i \partial p_j}\left(\langle \Delta p_i \Delta p_j \rangle f_0\right) \\ & + O(\langle \Delta p_i \Delta p_j \Delta p_k \rangle) + O(\Delta t^2), \end{aligned}$$

where the $O(\langle \Delta p_i \Delta p_j \Delta p_k \rangle)$ term involves averages of the quantities that are third order or higher in their momentum displacements. Taking the limit $\Delta p,\; \Delta t \rightarrow 0$ and neglecting the third order components (Rosenbluth *et al.*, 1957) we can define the coefficients

$$D_i \;\; = \;\; \lim_{\Delta p,\, \Delta t \rightarrow 0} \frac{\langle \Delta p_i \rangle}{\Delta t}, \tag{5.6}$$

$$D_{ij} \;\; = \;\; \lim_{\Delta p,\, \Delta t \rightarrow 0} \frac{\langle \Delta p_i \Delta p_j \rangle}{\Delta t}, \tag{5.7}$$

and obtain the Fokker-Planck equation for six dimensional phase space

$$\frac{\partial f_0}{\partial t} + v_i \frac{\partial f_0}{\partial x_i} = -\frac{\partial}{\partial p_i}\left(D_i f_0\right) + \frac{1}{2}\frac{\partial^2}{\partial p_i \partial p_j}\left(D_{ij} f_0\right). \tag{5.8}$$

Of interest in this thesis is the application of this equation to the propagation and acceleration of plasma particles in a magnetic field. A natural coordinate system to use for this case is spherical polars; we discuss how to write the Fokker-Planck equation in terms of this coordinate system next.

5.2.1 Fokker-Planck equation for high-energy plasma particles

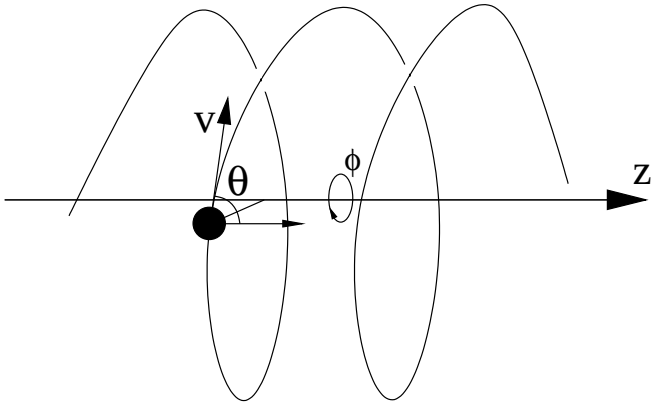

Figure 5.1: The propagation of a charged particle in a magnetic field which is aligned to the z axis. The particle, with speed v, spirals around the field line with an angle of θ to the axis.

Due to the effect of the Lorentz force, charged particles travelling through a magnetic field spiral around and along the field lines. A common approach, when considering the acceleration and transport of charged particles, is to assume a "guide" magnetic field along which the particles propagate. Particles travelling along the guide magnetic field may be subject to superimposed physical effects, such as collisions with a "cold" (thermal) background plasma of passive particles or interactions with magnetic and electric fields generated by turbulent plasma motions.

A natural formulation for charged particles propagating along a field line is to consider the field aligned to one of the spatial coordinates (z axis), and work in spherical coordinates for the momentum (Figure 5.1). Analogous to the relationship between Cartesian and spherical polar positional coordinates

(specified by $x = r\cos\phi\sin\theta$, $y = r\sin\phi\sin\theta$, $z = r\cos\theta$, where r is distance from the origin), the Cartesian momentum components p_x, p_y and p_z are related to the momentum magnitude p, pitch angle cosine $\mu = \cos\theta$ and azimuthal angle ϕ by

$$\begin{aligned} p_x &= p\cos\phi\sqrt{1-\mu^2}, \\ p_y &= p\sin\phi\sqrt{1-\mu^2}, \\ p_z &= \mu p, \end{aligned}$$

where $0 \le \phi \le 2\pi$, $-1 \le \mu \le 1$ ($0 \le \theta \le \pi$), and the momentum space volume element is

$$\mathrm{d}^3\mathbf{p} = p^2\,\mathrm{d}p\,\mathrm{d}\mu\,\mathrm{d}\phi.$$

We now seek to express the Fokker-Planck equation (5.8) in these coordinates. Using the chain rule we can write, for example,

$$\frac{\partial}{\partial p_x} = \frac{\partial p}{\partial p_x}\frac{\partial}{\partial p} + \frac{\partial \mu}{\partial p_x}\frac{\partial}{\partial \mu} + \frac{\partial \phi}{\partial p_x}\frac{\partial}{\partial \phi},$$

and obtain

$$\frac{\partial}{\partial p_x} = \sqrt{1-\mu^2}\cos\phi\frac{\partial}{\partial p} - \frac{\mu\sqrt{1-\mu^2}\cos\phi}{p}\frac{\partial}{\partial \mu} - \frac{\sin\phi}{p\sqrt{1-\mu^2}}\frac{\partial}{\partial \phi}, \quad (5.9)$$

$$\frac{\partial}{\partial p_y} = \sqrt{1-\mu^2}\sin\phi\frac{\partial}{\partial p} - \frac{\mu\sqrt{1-\mu^2}\sin\phi}{p}\frac{\partial}{\partial \mu} + \frac{\cos\phi}{p\sqrt{1-\mu^2}}\frac{\partial}{\partial \phi}, \quad (5.10)$$

$$\frac{\partial}{\partial p_z} = \mu\frac{\partial}{\partial p} + \frac{1-\mu^2}{p}\frac{\partial}{\partial \mu}. \quad (5.11)$$

For reference, second order operators are given in Appendix A.

By defining the spherical polar advection and diffusion coefficients

$$D_p = \sqrt{1-\mu^2}\cos\phi D_x + \sqrt{1-\mu^2}\sin\phi D_y + \mu D_z, \quad (5.12)$$

$$D_\mu = -\frac{\mu\sqrt{1-\mu^2}\cos\phi}{p}D_x - \frac{\mu\sqrt{1-\mu^2}\sin\phi}{p}D_y + \frac{1-\mu^2}{p}D_z, \quad (5.13)$$

$$D_\phi = -\frac{\sin\phi}{p\sqrt{1-\mu^2}}D_x + \frac{\cos\phi}{p\sqrt{1-\mu^2}}D_y, \quad (5.14)$$

$$
\begin{aligned}
D_{pp} &= \frac{1}{2}(1-\mu^2)\cos^2\phi D_{xx} + \frac{1}{2}(1-\mu^2)\sin^2\phi D_{yy} + \frac{\mu^2}{2}D_{zz} \\
&\quad +\mu\sqrt{1-\mu^2}\cos\phi D_{xz} + \mu\sqrt{1-\mu^2}\sin\phi D_{yz} \\
&\quad +(1-\mu^2)\sin\phi\cos\phi D_{xy}, \qquad (5.15)\\
D_{\mu p} &= -\frac{\mu(1-\mu^2)\cos^2\phi}{2p}D_{xx} - \frac{\mu(1-\mu^2)\sin^2\phi}{2p}D_{yy} + \frac{\mu(1-\mu^2)}{2p}D_{zz} \\
&\quad +\frac{(1-2\mu^2)\sqrt{1-\mu^2}\cos\phi}{2p}D_{xz} + \frac{(1-2\mu^2)\sqrt{1-\mu^2}\sin\phi}{2p}D_{yz} \\
&\quad -\frac{\mu(1-\mu^2)\sin\phi\cos\phi}{p}D_{xy}, \qquad (5.16)\\
D_{\mu\mu} &= \frac{\mu^2(1-\mu^2)\cos^2\phi}{2p^2}D_{xx} + \frac{\mu^2(1-\mu^2)\sin^2\phi}{2p^2}D_{yy} + \frac{(1-\mu^2)^2}{2p^2}D_{zz} \\
&\quad -\frac{\mu(1-\mu^2)^{3/2}\cos\phi}{p^2}D_{xz} - \frac{\mu(1-\mu^2)^{3/2}\sin\phi}{p^2}D_{yz} \\
&\quad +\frac{\mu^2(1-\mu^2)\sin\phi\cos\phi}{p^2}D_{xy}, \qquad (5.17)\\
D_{\phi\phi} &= \frac{\sin^2\phi}{2p^2(1-\mu^2)}D_{xx} + \frac{\cos^2\phi}{2p^2(1-\mu^2)}D_{yy} - \frac{\sin\phi\cos\phi}{p^2(1-\mu^2)}D_{xy}, \qquad (5.18)\\
D_{\phi p} &= -\frac{\sin\phi\cos\phi}{2p}D_{xx} + \frac{\sin\phi\cos\phi}{2p}D_{yy} - \frac{\mu\sin\phi}{2p\sqrt{1-\mu^2}}D_{xz} \\
&\quad +\frac{\mu\cos\phi}{2p\sqrt{1-\mu^2}}D_{yz} + \frac{\sin^2\phi-\cos^2\phi}{2p}D_{xy}, \qquad (5.19)\\
D_{\phi\mu} &= \frac{\mu\sin\phi\cos\phi}{2p^2}D_{xx} - \frac{\mu\sin\phi\cos\phi}{2p^2}D_{yy} - \frac{\sqrt{1-\mu^2}\sin\phi}{2p^2}D_{xz} \\
&\quad +\frac{\sqrt{1-\mu^2}\cos\phi}{2p^2}D_{yz} + \frac{\mu(\sin^2\phi-\cos^2\phi)}{2p^2}D_{xy}, \qquad (5.20)
\end{aligned}
$$

we may write the Fokker-Planck equation (5.8) as

$$
\begin{aligned}
\frac{\partial f_0}{\partial t} &= -v_i\frac{\partial f_0}{\partial x_i} - \frac{1}{p^2}\frac{\partial}{\partial p}(p^2 D_p f_0) - \frac{\partial}{\partial\mu}(D_\mu f_0) - \frac{\partial}{\partial\phi}(D_\phi f_0) \\
&\quad +\frac{1}{p^2}\frac{\partial}{\partial p}\left[p^2\left(D_{\mu p}\frac{\partial f_0}{\partial\mu} + D_{pp}\frac{\partial f_0}{\partial p} + D_{\phi p}\frac{\partial f_0}{\partial\phi}\right)\right] \\
&\quad +\frac{\partial}{\partial\mu}\left(D_{\mu\mu}\frac{\partial f_0}{\partial\mu} + D_{\mu p}\frac{\partial f_0}{\partial p} + D_{\phi\mu}\frac{\partial f_0}{\partial\phi}\right) \\
&\quad +\frac{\partial}{\partial\phi}\left(D_{\phi\mu}\frac{\partial f_0}{\partial\mu} + D_{\phi p}\frac{\partial f_0}{\partial p} + D_{\phi\phi}\frac{\partial f_0}{\partial\phi}\right). \qquad (5.21)
\end{aligned}
$$

If the gyro-radius (2.8) is small compared to magnetic field variations then we can assume axial symmetry (Schlickeiser and Jenko, 2010). This allows us to remove the dependence on the azimuthal coordinate ϕ from the distribution function. We likewise assume negligible particle transport perpendicular to the field, allowing us to ignore the x and y spatial coordinates and write

$v_z = \mu v$. We define the spatially averaged gyrotropic particle number density distribution function

$$f_0 = f_0(z,\, p,\, \mu,\, t) \tag{5.22}$$

which, from equation (5.1), obeys the normalisation

$$\int_z \int_\mu \int_p f_0(z,\, p,\, \mu,\, t=0)\, p^2 \, \mathrm{d}p \, \mathrm{d}\mu \, \mathrm{d}z = \frac{n}{2\pi}. \tag{5.23}$$

Here n is the number of particles in a volume with unit cross-section aligned to the z axis and extending to $z \to \pm\infty$. Assuming the coefficients D_i and D_{ij} are independent of ϕ and integrating equation (5.21) over ϕ leads to

$$\begin{aligned} \frac{\partial f_0}{\partial t} &= -\mu v \frac{\partial f_0}{\partial z} - \frac{1}{p^2}\frac{\partial}{\partial p}(p^2 D_p f_0) - \frac{\partial}{\partial \mu}(D_\mu f_0) \\ &\quad + \frac{1}{p^2}\frac{\partial}{\partial p}\left[p^2\left(D_{\mu p}\frac{\partial f_0}{\partial \mu} + D_{pp}\frac{\partial f_0}{\partial p}\right)\right] \\ &\quad + \frac{\partial}{\partial \mu}\left(D_{\mu\mu}\frac{\partial f_0}{\partial \mu} + D_{\mu p}\frac{\partial f_0}{\partial p}\right), \end{aligned} \tag{5.24}$$

where coefficients become

$$D_p = \mu D_z, \tag{5.25}$$

$$D_\mu = \frac{1-\mu^2}{p} D_z, \tag{5.26}$$

$$D_{pp} = \frac{1}{4}(1-\mu^2)D_{xx} + \frac{1}{4}(1-\mu^2)D_{yy} + \frac{\mu^2}{2}D_{zz}, \tag{5.27}$$

$$D_{\mu p} = -\frac{\mu(1-\mu^2)}{4p}D_{xx} - \frac{\mu(1-\mu^2)}{4p}D_{yy} + \frac{\mu(1-\mu^2)}{2p}D_{zz}, \tag{5.28}$$

$$D_{\mu\mu} = \frac{\mu^2(1-\mu^2)}{4p^2}D_{xx} + \frac{\mu^2(1-\mu^2)}{4p^2}D_{yy} + \frac{(1-\mu^2)^2}{2p^2}D_{zz}. \tag{5.29}$$

The form of condition (5.23) suggests a natural change to the distribution function. Defining

$$f(z,\, p,\, \mu,\, t) = 2\pi p^2 f_0 \tag{5.30}$$

leads to the normalisation

$$\int_z \int_\mu \int_p f(z,\, p,\, \mu,\, t=0)\, \mathrm{d}p \, \mathrm{d}\mu \, \mathrm{d}z = n, \tag{5.31}$$

and the Fokker-Planck equation

$$\begin{aligned}\frac{\partial f}{\partial t} &= -\frac{\partial}{\partial z}(\mu v f) - \frac{\partial}{\partial \mu}\left[\left(D_\mu + \frac{\partial D_{\mu\mu}}{\partial \mu} + \frac{1}{p^2}\frac{\partial}{\partial p}\left(p^2 D_{\mu p}\right)\right) f\right] \\ &\quad -\frac{\partial}{\partial p}\left[\left(D_p + \frac{\partial D_{\mu p}}{\partial \mu} + \frac{1}{p^2}\frac{\partial}{\partial p}\left(p^2 D_{pp}\right)\right) f\right] \\ &\quad +\frac{\partial^2}{\partial \mu^2}(D_{\mu\mu} f) + \frac{\partial^2}{\partial \mu \partial p}(2 D_{\mu p} f) + \frac{\partial^2}{\partial p^2}(D_{pp} f). \end{aligned} \tag{5.32}$$

Equation (5.32) represents the starting point for much of the remaining work of this thesis. However, this second order partial differential equation in variables z, t, μ and p can only be solved analytically in very restrictive cases. In addition, solving this Fokker-Planck equation directly using numerical methods can be problematic due to the large number of mesh points required for four dimensional simulations. In many cases, however, progress can be made by expressing the Fokker-Planck equation as a system of stochastic differential equations. We now discuss the underpinning theory of the equivalence of the Fokker-Planck and stochastic equations.

5.3 Stochastic calculus

To demonstrate the stochastic approach to solving the Fokker-Planck equation, let us first examine how considering probability density fluctuations on a small scale can lead to both the Fokker-Planck equation and a set of stochastic equations.

We follow the argument as laid out in Schulman (1996). Consider a simple discrete system on a one dimensional mesh, where $u(j,\, n)$ is a particle position probability at a mesh point $x = j\Delta x$ and time $t = n\Delta t$ (Δx and Δt are the space and time steps respectively). Suppose the particle has a probability p of moving to the right and q of moving to the left. For a particle, which started at $x = 0$ at time 0, to get to a position x requires k steps to the right and l steps to the left, where $k - l = j$ and $k + l = n$. The probability of the particle

reaching the point is given by

$$u(j,\, n) = \begin{cases} \frac{n!}{k!(n-k)!} p^k q^l & n-j \text{ even}, \\ 0 & n-j \text{ odd}. \end{cases}$$

Using the exponential limit

$$e^x = \lim_{n\to\infty} \left(1 + \frac{x}{n}\right)^n,$$

Stirling's approximation

$$n! \sim \sqrt{2\pi n} \left(\frac{n}{e}\right)^n,$$

and assuming j and n are large, we may write the probability

$$u(j,\, n) = \sqrt{\frac{2}{n\pi}} \exp\left(-\frac{(j - n(p-q))^2}{2n}\right).$$

Consider the particle probability density $f(x,\, t) = u(j,\, n)/(2\Delta x)$. Here the factor of two comes from the observation that, for a give time index n, u is only non-zero for $n - j$ even. Writing in terms of x and t, and taking the limit of $\Delta x,\ \Delta t \to 0$, gives

$$f(x,\, t) = \sqrt{\frac{1}{2\pi D_{xx} t}} \exp\left(-\frac{(x - D_x t)^2}{2 D_{xx} t}\right) \tag{5.33}$$

where we have defined, similar to equations (5.6-5.7),

$$D_x = \lim_{\Delta x, \Delta t \to 0} \frac{\Delta x}{\Delta t}(p - q), \tag{5.34}$$

$$D_{xx} = \lim_{\Delta x, \Delta t \to 0} \frac{\Delta x^2}{\Delta t}. \tag{5.35}$$

Equation (5.33) is simply a Gaussian function for x with mean $D_x t$ and variance $D_{xx} t$. A particular particle will therefore update its position according to the relation

$$\mathrm{d}x = D_x \,\mathrm{d}t + \sqrt{D_{xx}}\, W(t),$$

where $W(t)$, known as a Wiener process (Hopf and Wiener, 1932), is a function with mean 0 and variance t that simulates random noise – it is essentially a representation of Brownian motion (Einstein, 1905). Additionally, it is also straightforward to verify that (5.33) satisfies the Fokker-Planck equation

$$\frac{\partial f}{\partial t} = -\frac{\partial}{\partial x}(D_x f) + \frac{1}{2}\frac{\partial^2}{\partial x^2}(D_{xx} f).$$

In general we can express the equivalence of the Fokker-Planck equation to equations detailing the changes in the variables of the system as prescribed by Itô calculus (Itô (1944, 1951); see also Gardiner (2004) for a review). The general Fokker-Planck equation in variables s_i,

$$\frac{\partial}{\partial t}\left(f(\mathbf{s},\ t)\right) = -\frac{\partial}{\partial s_i}[D_i(\mathbf{s})f(\mathbf{s},\ t)] + \frac{1}{2}\frac{\partial^2}{\partial s_i \partial s_j}\left[D_{ij}f(\mathbf{s},\ t)\right], \tag{5.36}$$

is completely equivalent to the system of stochastic equations

$$\mathrm{d}\mathbf{s}(t) = \mathbf{D}(\mathbf{s})\,\mathrm{d}t + B(\mathbf{s})\,\mathrm{d}\mathbf{W}(t), \tag{5.37}$$

where $D_{ij} = (B(\mathbf{s},\ t)B^T(\mathbf{s},\ t))_{ij}$, $\mathbf{W}$ is a vector of Wiener processes each with mean 0 and variance t (Lemons, 2002; Gardiner, 2004) and summation over repeated indices is assumed.

This stochastic method is commonly used to study the Fokker-Planck equation both analytically (e.g. Conway *et al.*, 1998, Litvinenko, 2012b) and numerically (e.g. MacKinnon and Craig, 1991, Zhang, 1999, Strauss *et al.*, 2011). This method is distinguished from other Monte Carlo techniques (e.g. Earl, 1992) by the explicit introduction of a system of stochastic ordinary differential equations (see also Earl *et al.*, 1995 for a comparison of various numerical approaches).

We have discussed how a Fokker-Planck equation, often used to model particle distribution evolution, can be expressed as a system of stochastic differential equations. The next section demonstrates this equivalence by numerically examining a physically-based example problem of particle diffusion (as might occur, for example, with electrons in solar flare current sheets).

5.4 Diffusive charged particle transport

We consider the Fokker-Planck equation for the diffusion of charged particles along a guiding magnetic field. We follow the formulation of Earl (1974) (see also Earl, 1992) in which particles are elastically scattered due to interactions with turbulent magnetic fields propagating along the guiding field.

Specifically we assume that there is no momentum change of particles due to collisions ($\partial_p = 0$), that there are no drift forces on the system ($D_z = 0$) and that diffusion is isotropic and spatially invariant ($D_{xx} = D_{yy} = D_{zz} = D$, where D is a constant which controls the strength of the scattering). The Fokker-Planck equation (5.32) becomes

$$\frac{\partial f}{\partial t} = -\frac{\partial}{\partial z}(\mu v f) - \frac{\partial}{\partial \mu}\left(\frac{\partial D_{\mu\mu}}{\partial \mu} f\right) + \frac{\partial^2}{\partial \mu^2}(D_{\mu\mu} f), \tag{5.38}$$

where the scattering coefficient is given by

$$D_{\mu\mu} = \frac{D}{2p^2}(1-\mu^2).$$

Non-dimensionalising equation (5.38) using the variables $t = p^2 t^*/D$ and $z = vp^2 z^*/D$ allows us to write

$$\frac{\partial f}{\partial t} = -\frac{\partial}{\partial z}(\mu f) - \frac{\partial}{\partial \mu}(-\mu f) + \frac{1}{2}\frac{\partial^2}{\partial \mu^2}\left((1-\mu^2) f\right), \tag{5.39}$$

where we have dropped the asterisk notation in the final equation. Using equations (5.36) and (5.37) we can write the Fokker-Planck equation (5.39) as the system of stochastic differential equations

$$\mathrm{d}z = \mu\,\mathrm{d}t, \tag{5.40}$$

$$\mathrm{d}\mu = -\mu\,\mathrm{d}t + (1-\mu^2)^{1/2}\,\mathrm{d}W(t), \tag{5.41}$$

where W is a Wiener process (with mean 0 and variance t).

The dual formulations of the system, being the Fokker-Planck equation (5.39) and the stochastic system equations (5.40-5.41), each have different numerical methods of solution. We will now compare both approaches.

5.4.1 Comparison of numerical treatments

We will consider the solution of the Fokker-Planck system for a Gaussian initial condition

$$f(z,\, \mu,\, t=0) = \frac{1}{I}\exp\left(-\frac{(\mu - \langle\mu\rangle)^2}{2\sigma_\mu^2}\right)\exp\left(-\frac{(z-\langle z\rangle)^2}{2\sigma_z^2}\right),$$

where the distribution is centred around the point $(\langle z\rangle, \langle\mu\rangle)$ and has standard deviations σ_z and σ_μ for the z and μ directions respectively. The normalisation factor I is given, from equation (5.31), by

$$\begin{aligned} I &= \int_{-\infty}^{\infty}\int_{-1}^{1} \exp\left(-\frac{(\mu-\langle\mu\rangle)^2}{2\sigma_\mu^2}\right)\exp\left(-\frac{(z-\langle z\rangle)^2}{2\sigma_z^2}\right)\mathrm{d}\mu\,\mathrm{d}z \\ &= \pi\sigma_z\sigma_\mu\left(\mathrm{erf}\left(\frac{1-\langle\mu\rangle}{\sqrt{2}\sigma_\mu}\right)+\mathrm{erf}\left(\frac{1+\langle\mu\rangle}{\sqrt{2}\sigma_\mu}\right)\right). \end{aligned}$$

Note that we have chosen to represent f as a probability density ($n = 1$) for the sake of simplicity. Here the error function is defined by

$$\mathrm{erf}(x) = \frac{2}{\sqrt{\pi}}\int_0^x e^{-\lambda^2}\,\mathrm{d}\lambda,$$

and we made use of the Gaussian integral $\int_{-\infty}^{\infty} e^{-\lambda^2}\,\mathrm{d}\lambda = \sqrt{\pi}$. We calculate the solution over the area $|\mu| \leq 1$, $|z| \leq 3$ for time $0 \leq t \leq 2.5$. As we are representing both advective and diffusive effects the time step Δt in our simulations is chosen to obey both the advective Courant-Friedrichs-Lewy (CFL) (Courant *et al.*, 1928) and diffusion restrictions. For an advection-diffusion equation of the form

$$\frac{\partial f}{\partial t} = a\frac{\partial f}{\partial x} + b\frac{\partial^2 f}{\partial x^2},$$

the CFL and diffusion conditions are

$$\Delta t \leq \frac{\Delta x}{a}, \tag{5.42}$$

and

$$\Delta t \leq \frac{(\Delta x)^2}{b}, \tag{5.43}$$

respectively. These conditions lead to timestep limits of $\Delta t \leq \Delta x$ and $\Delta t \leq (\Delta x)^2$ for the present simulation. In practice, simulations are repeated, with the timestep halved, to check the consistency and convergence of the solution.

We begin our comparison of numerical techniques by solving equation (5.39) directly using a standard finite difference method on a 401×401 point mesh in variables μ and z. For simplicity the condition on the $|z| = 3$ boundary was taken to be $f = 0$, with the simulation run for such time as the distribution did not interact significantly with z limit.

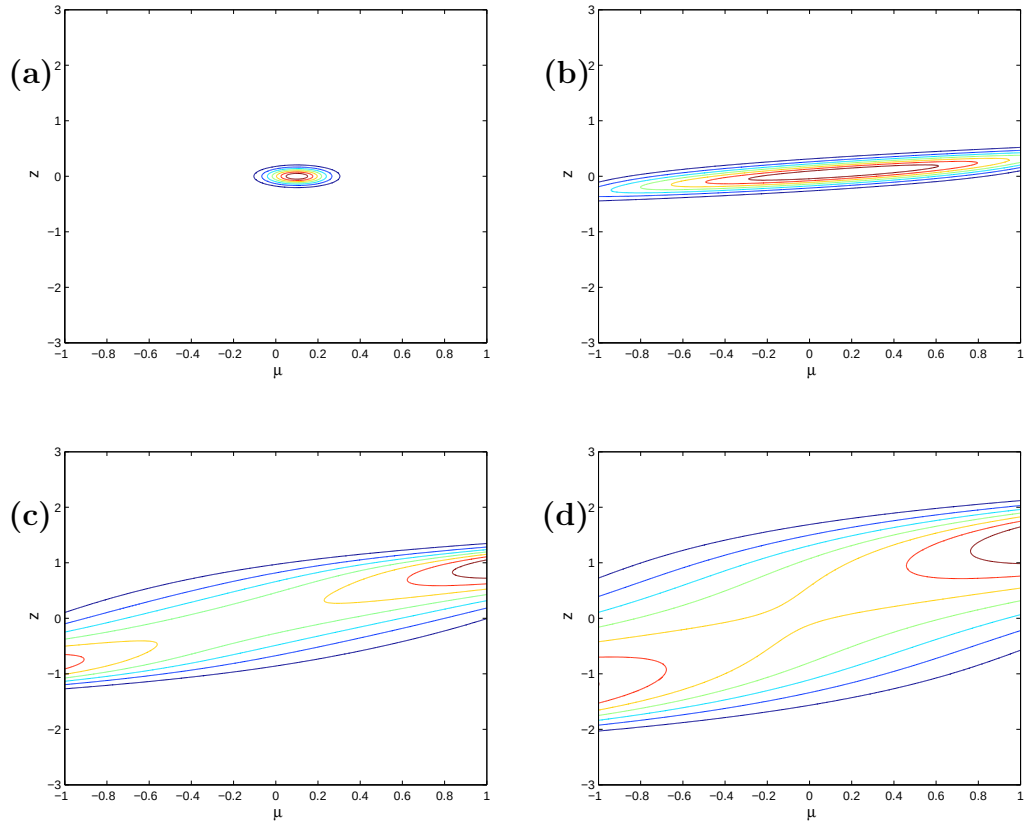

Figure 5.2: Finite difference solution of equation (5.39) at $t = 0$ (a), $t = 0.5$ (b), $t = 1.5$ (c) and $t = 2.5$ (d) on a 401×401 point mesh in variables μ and z. The initial parameters are $\langle \mu \rangle = \sigma_z = \sigma_\mu = 0.1$, $\langle z \rangle = 0$.

The $|\mu| = 1$ boundary requires a more subtle approach as fixing the value of the solution on this boundary or taking a constant flux condition would be non-physical. We evaluate it by calculating the solution excluding the boundary and then interpolating the boundary points from the internal mesh.

Figure 5.2 shows the evolution ($t = 0$, 0.5, 1.5, 2.5) of a distribution function that begins with parameters $\langle\mu\rangle = \sigma_z = \sigma_\mu = 0.1$, $\langle z\rangle = 0$. This initial distribution corresponds to a closely clumped population of particles travelling slowly along the positive z direction. The distribution quickly spreads in pitch angle space (panel b) which leads to spacial diffusion (panels c and d).

5.4.2 Stochastic solution

A stochastic solution of equations (5.40) and (5.41) involves using an explicit Euler-Maruyama scheme (for a discussion see Higham., 2001) to model a large enough number of particles so that we obtain an adequate representation of the distribution function. Explicitly, we iteratively calculate (from equations (5.40-5.41)):

$$z_{i+1} = z_i + \mu_i \, \Delta t, \tag{5.44}$$

$$\mu_{i+1} = \mu_i - \mu_i \, \Delta t + (1 - \mu_i^2)^{1/2} \, \Delta W(t), \tag{5.45}$$

where i denotes the level of iteration and Δt is the timestep. The Wiener process is modelled as

$$\Delta W(t) = N(t)\sqrt{\Delta t},$$

where $N(t)$ is a normally distributed pseudo-random number with mean 0 and variance 1 (Gardiner, 2004; Strauss *et al.*, 2011).

We use an array of 41×41 bins of uniform width to record the number of particles within a coordinate range at a certain time. Using this approach only one boundary condition needs to be considered, that of $|\mu| = 1$. While the $1 - \mu^2$ dependence of equation (5.41) prohibits any particle nearing the boundary from reaching it, in practice for discrete time steps there is a chance that a particle may end up with a pitch angle $|\mu| > 1$. We therefore take

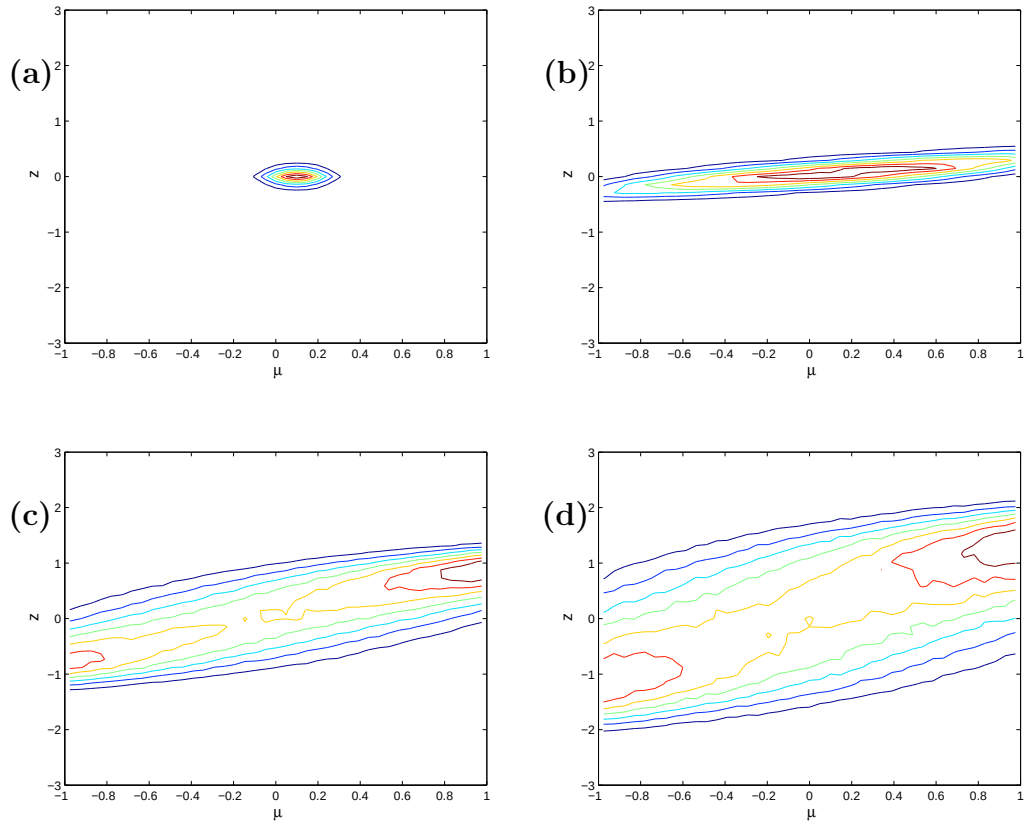

Figure 5.3: Stochastic solution of equations (5.40) and (5.41) at $t = 0,\ 0.5,\ 1.5$ and 2.5. The initial condition is the same as in Figure 5.2. The distribution was generated using 10^6 particles distributed across an array of 41×41 bins of uniform width.

the simplest approach to particles crossing this boundary - they retain their previous pitch angle. The simulation is found to be largely insensitive to this or other sensible choice of boundary condition. A possible alternative would be reflection whereby, for example, a particle reaching $\mu = 1 + \delta$ is given the value $\mu = 1 - \delta$.

A stochastic simulation of 10^6 particles using the same initial conditions as Figure 5.2 is shown in Figure 5.3. As can be seen we recover the distribution of Figure 5.2 with some small variations. We stated above that the representation of the distribution depends on the number of particles used - more precisely the variance of a measurement is inversely proportional to the number of particles used (Lemons, 2002). This is illustrated in Figure 5.4, where the standard deviation (σ) of $\langle z \rangle$ and $\langle \mu \rangle$ at time $t = 2.5$ is shown for varying particle

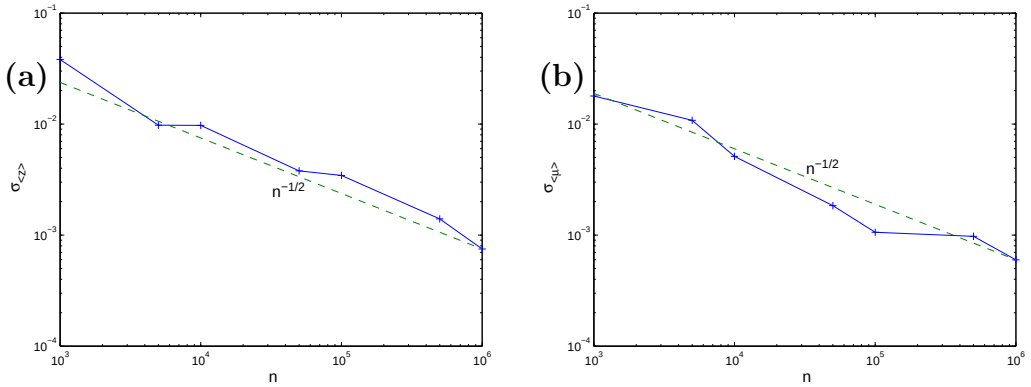

Figure 5.4: Comparison of standard deviation (σ) of $\langle z \rangle$ (panel a) and $\langle \mu \rangle$ (panel b) at $t = 2.5$ for increasing particle numbers. For each data point the simulation was repeated ten times and the standard deviation of the average z and μ values was calculated over these runs. The initial condition is the same as in Figure 5.2.

numbers. For each data point the simulation was repeated ten times and the standard deviation of the average z and μ values was calculated over these runs. The expected $\sigma \sim n^{-1/2}$ scaling is clear in both cases.

Finally the equivalence between the Fokker-Planck and stochastic formulations is demonstrated in Figure 5.5, where the finite difference solution averaged over pitch angle at time $t = 2.5$ is compared to normalised stochastic solutions for 10^3, 5×10^3, 2×10^4 and 10^6 particles. We see that as particle numbers are increased we recover the finite difference solution.

This section allowed us to discuss how we can easily numerically model Fokker-Planck systems using a stochastic formulation. In the next section we demonstrate how analytic arguments based on a stochastic approach can readily lead to useful results by considering a model of electron propagation in a coronal loop.

5.5 Electron transport in solar flare loops

Observations by the Japanese satellite Yokoh and the Reuven Ramaty High Energy Solar Spectroscopic Imager (RHESSI) have shown some solar flare

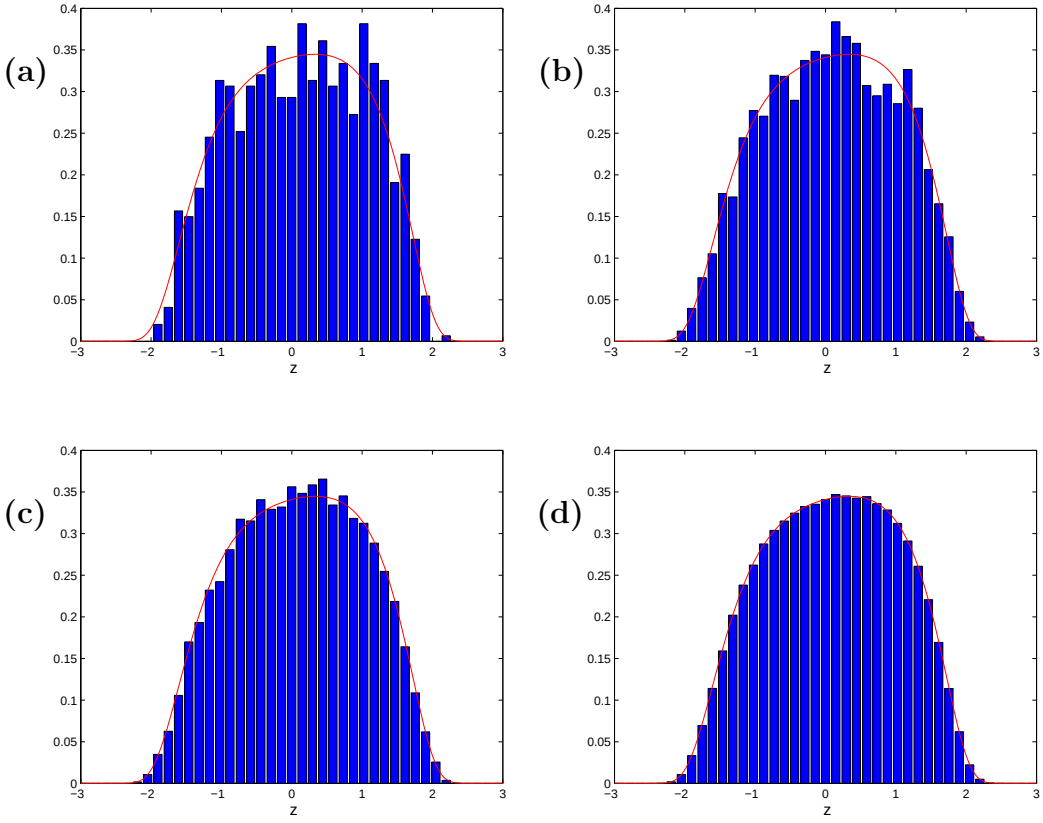

Figure 5.5: Comparison of pitch angle averaged finite difference (solid line) and normalised stochastic (bars) solutions at $t = 2.5$. The stochastic solutions were generated with (a) 10^3, (b) 5×10^3, (c) 2×10^4 and (d) 10^6 particles distributed in 41 bins.

loops have hard X-ray sources at the looptop and footpoints (Masuda *et al.*, 1995; Krucker *et al.*, 2008). These hard X-rays are believed to be produced by bremsstrahlung emission (Holman *et al.*, 2011). That is to say, accelerated electrons scatter off thermal electrons and ions in the background plasma and release high energy X-rays. Studies such as Wheatland and Melrose (1995) showed that much of the observed phenomena can be explained by electron collisional transport (see also Fletcher and Martens, 1998; Conway *et al.*, 1998; Holman *et al.*, 2011).

In this section we use the flare loop situation as a platform from which to demonstrate various useful analytical techniques for Fokker-Planck systems. Firstly, we formulate a Fokker-Planck electron scattering model. Then, by taking a mean scattering approach, we will consider the implications on the energy spectrum of the distribution. In addition, by expressing the Fokker-Planck equation in stochastic form and calculating moments, we obtain a generalisation to the hard X-ray emission prediction of Conway *et al.* (1998). We will compare this with a diffusion approximation and check the validity of the results using a numerical simulation.

5.5.1 Coulomb collision model

Consider the coronal loop of Figure 5.6, where a population of n electrons, potentially accelerated due to a reconnection event, is injected in the top of a coronal loop before streaming towards the foot-points. These particles undergo Coulomb collisions with the "background" hydrogen ions in the loop. Based on this simple model we consider a guide magnetic field Fokker-Planck model where the coefficients represent Coulomb interactions.

Rosenbluth *et al.* (1957) demonstrated that the Fokker-Planck coefficients (5.4) and (5.5) for Coulomb collisions between "test" particles (signified by index a) and a background distribution (b) can be written

$$D_i = m_a D' \frac{\partial H_{ab}}{\partial v_i}, \qquad D_{ij} = m_a^2 D' \frac{\partial^2 G_{ab}}{\partial v_i \partial v_j}, \tag{5.46}$$

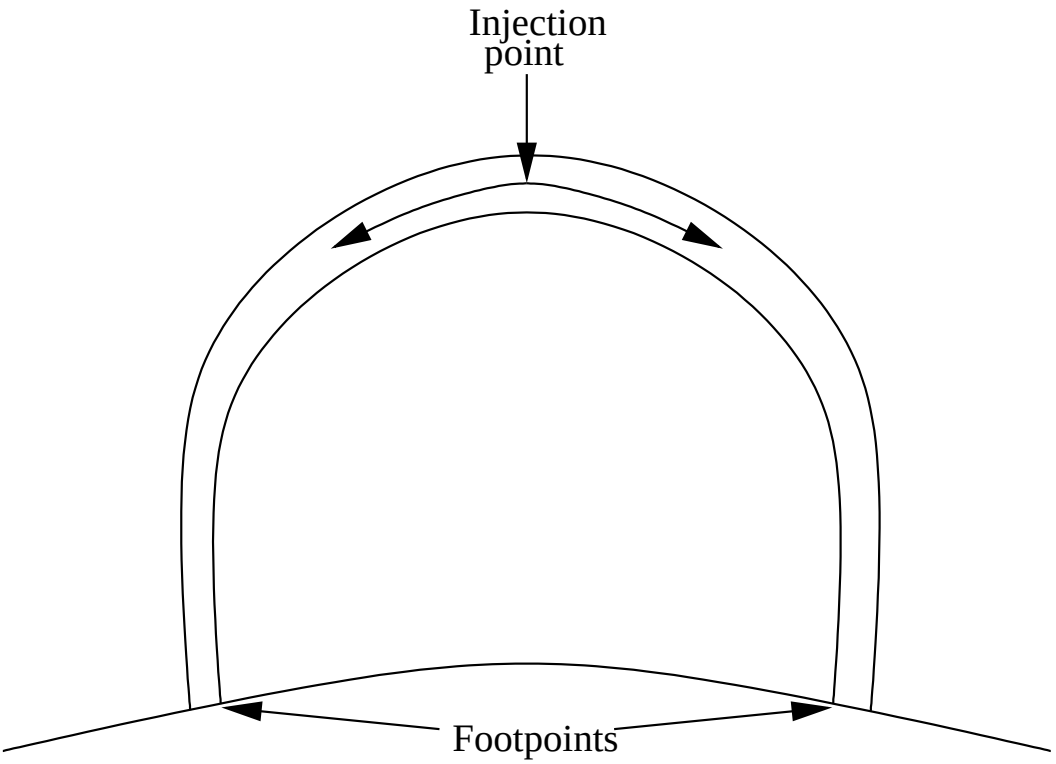

Figure 5.6: A model coronal loop. Here electrons are injected in the top of the loop, where they undergo Coulomb interactions with the loop plasma while propagating towards the foot-points.

where the Rutherford scattering coefficient is given by

$$D' = \frac{4\pi (Z_a Z_b e^2)^2 \lambda_{ab}}{m_a^2}. \tag{5.47}$$

Here $e = 4.803 \times 10^{-10}$ statC is the electron charge, Z_a and Z_b are the charges of particles of type a and b in units of e, and m_a is the mass of particles of type a. The Coulomb logarithm λ_{ab} generally varies between 5 and 25 in the corona (Priest, 1982). The Rosenbluth potentials are

$$H_{ab}(\mathbf{v}_a) = \frac{m_a + m_b}{m_b} \int \frac{f_b(\mathbf{v}'_b)}{|\mathbf{v}_a - \mathbf{v}'_b|} \, \mathrm{d}\mathbf{v}'_b, \tag{5.48}$$

$$G_{ab}(\mathbf{v}_a) = \int f_b(\mathbf{v}'_b) |\mathbf{v}_a - \mathbf{v}'_b| \, \mathrm{d}\mathbf{v}'_b, \tag{5.49}$$

where we have followed the notation of Ljepojevic and Burgess (1990).

Converting (5.46) to spherical polar coordinates (similar to Section 5.2.1),

and integrating over ϕ leads to the coefficients

$$D_p = D' m_a \frac{\partial H_{ab}}{\partial v}, \tag{5.50}$$

$$D_\mu = D' \frac{1-\mu^2}{v^2} \frac{\partial H_{ab}}{\partial \mu}, \tag{5.51}$$

$$D_{pp} = D' m_a^2 \frac{\partial^2 G_{ab}}{\partial v^2}, \tag{5.52}$$

$$D_{\mu p} = D' m_a \frac{1-\mu^2}{v^2} \left(\frac{\partial^2 G_{ab}}{\partial \mu \partial v} - \frac{1}{v} \frac{\partial G_{ab}}{\partial \mu} \right), \tag{5.53}$$

$$D_{\mu\mu} = \frac{D'}{v^2} \left(\frac{(1-\mu^2)^2}{v^2} \frac{\partial^2 G_{ab}}{\partial \mu^2} + \frac{1-\mu^2}{v} \frac{\partial G_{ab}}{\partial v} - \frac{\mu(1-\mu^2)}{v^2} \frac{\partial G_{ab}}{\partial \mu} \right). \tag{5.54}$$

We are considering the case of a population of electrons colliding with background hydrogen ions. If we expand equations (5.48-5.49) to first order in Legendre polynomials, assume that the electron speed is large and assume that the ion speed is small compared to the electron speed, we may write the Rosenbluth potentials as (Ljepojevic and Burgess, 1990)

$$H_{ei} = \frac{m_e + m_i}{m_i} \frac{n}{v}, \qquad G_{ei} = nv.$$

Here n is the background number density and the electron mass has the value $m_e = 9.110 \times 10^{-28}\,\mathrm{g}$. Additionally assuming $m_e + m_i \simeq m_i$ the coefficients reduce to $D_\mu = D_{\mu p} = D_{pp} = 0$,

$$D_p = -\frac{D m_e}{v^2}, \tag{5.55}$$

and

$$D_{\mu\mu} = \frac{D(1-\mu^2)}{v^3}, \tag{5.56}$$

where the scattering parameter is

$$D = \frac{4\pi e^4 \lambda_{ei} n}{m_e^2}. \tag{5.57}$$

Therefore, for Coulomb collisions, the axi-symmetric Fokker-Planck equation (5.32) becomes (e.g. MacKinnon and Craig, 1991, Conway *et al.*, 1998)

$$\frac{\partial f}{\partial t} = -\frac{\partial}{\partial z}(\mu v f) - \frac{\partial}{\partial v}\left(-\frac{D}{v^2} f\right) - \frac{\partial}{\partial \mu}\left(-\frac{2D\mu}{v^3} f\right) + \frac{\partial^2}{\partial \mu^2}\left(\frac{D(1-\mu^2)}{v^3} f\right), \tag{5.58}$$

where we have written it in terms of v for consistency with the literature. Equation (5.58) can be non-dimensionalised with respect to some characteristic speed v_0 by substituting $v = v_0 v^*$, $z = v_0^4 z^*/D$ and $t = v_0^3 t^*/D$. Dropping the non-dimensional asterisk notation we can write

$$\frac{\partial f}{\partial t} = -\frac{\partial}{\partial z}(\mu v f) - \frac{\partial}{\partial v}\left(-\frac{f}{v^2}\right) - \frac{\partial}{\partial \mu}\left(-\frac{2\mu f}{v^3}\right) + \frac{1}{2}\frac{\partial^2}{\partial \mu^2}\left(\frac{2}{v^3}(1-\mu^2)f\right). \quad (5.59)$$

This is the form of the Fokker-Planck equation we will use for the work of this section. We begin by considering the evolution of a population of particles which have a power law energy spectrum as their initial condition.

5.5.2 Coronal energy spectra

Energy spectra in the corona typically follow a power law $F(E) \propto E^{-\gamma}$, where $F(E)$ is the number of particles at energy E and γ is a positive spectral index. Distributions with proportionally more particles at higher energies than lower energies (γ small) are described as "hard" (and conversely, proportionally more particles at lower energies (γ large) are called "soft" distributions).

Observations of flare electron energetics put the hardest spectral index around $\gamma = 3/2$ (Lin *et al.*, 1982; Miller *et al.*, 1997; Holman *et al.*, 2003). Recent work (e.g. Heerikhuisen *et al.*, 2002; Wood and Neukirch, 2005; Drake *et al.*, 2013) has attempted to simulate particle acceleration in a reconnection framework. We take a much simpler approach here and demonstrate how the method of characteristics can be used on a simplified, mean scattering, form of the Fokker-Planck equation to calculate the evolution of the energy spectrum.

Assuming mean scattering, whereby the second order derivative in pitch angle is neglected, the Fokker-Planck equation (5.59) becomes

$$\frac{\partial f}{\partial t} + \mu v \frac{\partial f}{\partial z} - \frac{1}{v^2}\frac{\partial f}{\partial v} - \frac{2\mu}{v^3}\frac{\partial f}{\partial \mu} = 0. \quad (5.60)$$

The method of characteristics (see Craig *et al.*, 1985) gives the characteristic

equations

$$\begin{aligned} \mathrm{d}z &= \mu v \,\mathrm{d}t, && (5.61)\\ \mathrm{d}v &= -\frac{1}{v^2}\,\mathrm{d}t, && (5.62)\\ \mathrm{d}\mu &= -\frac{2\mu}{v^3}\,\mathrm{d}t, && (5.63)\\ \mathrm{d}f &= 0. && (5.64) \end{aligned}$$

Solving equations (5.61 - 5.63) will give an individual particle's trajectory, based on its initial position in phase space. Consider, for instance, a particle with initial coordinates $v_i,\ z_i$ and μ_i. Equations (5.61 - 5.63) give

$$\begin{aligned} v &= (v_i^3 - 3t)^{1/3}, && (5.65)\\ \mu &= \frac{\mu_i}{v_i^2}(v_i^3 - 3t)^{2/3}, && (5.66)\\ z &= z_i + \frac{\mu_i}{6v_i^2}\left(v_i^6 - (v_i^3 - 3t)^2\right), && (5.67) \end{aligned}$$

which completely specify the particle's behaviour. Equation (5.64) results in a constant distribution function along a characteristic $f(z,\, \mu,\, v,\, t) = F(z_i,\, \mu_i,\, v_i)$. This allows us, by inverting equations (5.65-5.67), to find the distribution function based on some given initial distribution F.

To examine the energy spectrum evolution, however, we need only consider equation (5.65). We can write it in the form

$$E(E_i,\, t) = \left(E_i^{3/2} - 3t\right)^{2/3}, \qquad (5.68)$$

where E is the kinetic energy for a particle (non-dimensionalised by the factor $m_e v_0^2/2$) at some time t and E_i is the initial energy. Suppose now that we have a spatially averaged power law initial energy spectrum of the form

$$F(E_i,\, t = 0) = n(\gamma - 1)E_0^{\gamma-1}E_i^{-\gamma},$$

where n is the number of electrons in the distribution, E_0 is a background "cutoff" energy and the spectral index is bounded by $\gamma > 1$. The cutoff parameter E_0 prevents the normalisation integral

$$n = \int_{E_0}^{\infty} F(E_i,\, t = 0)\,\mathrm{d}E_i$$

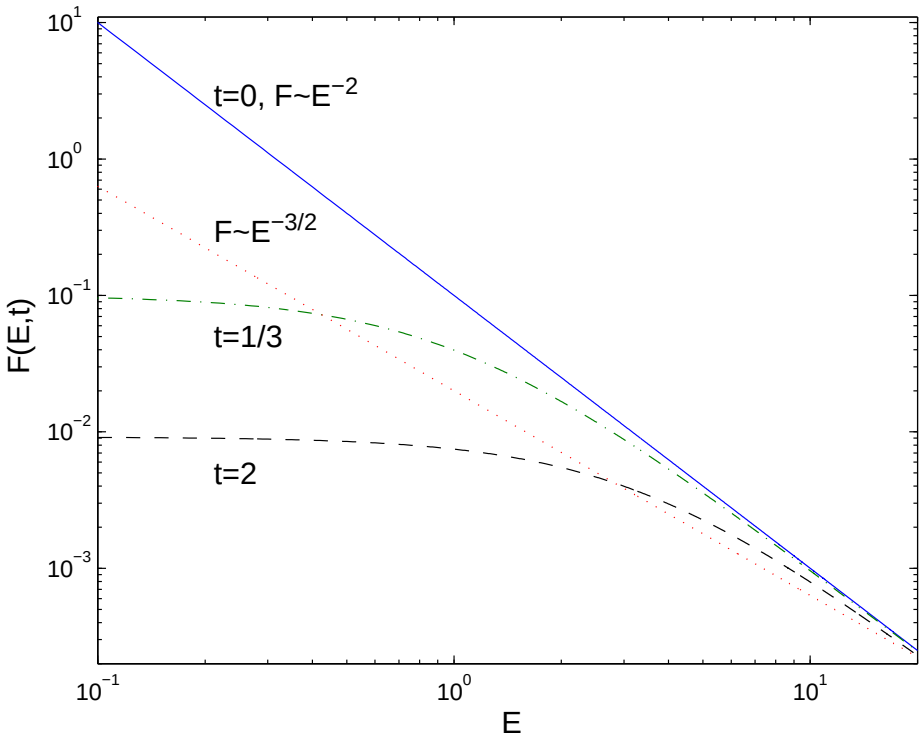

Figure 5.7: Energy spectrum distribution F at times $t = 0$ (solid line), $t = 1/3$ (dot-dashed line) and $t = 2$ (dashed line). The initial parameters are $n = 1$, $E_0 = 0.1$ and $\gamma = 2$. An energy spectrum of the form $F \sim E^{-3/2}$ (dotted line) is shown for comparison.

from diverging – physically it represents the energy at which electrons rejoin the background plasma. We can rearrange equation (5.68) for E_i and substitute to give the time-dependent energy spectrum

$$F(E,\, t) = n(\gamma - 1)E_0^{\gamma-1}\left(E^{3/2} + 3t\right)^{-2\gamma/3}. \tag{5.69}$$

To examine what our simple model means for flare particle energetics we consider the evolution of an electron distribution with initial spectral index $\gamma = 2$. Figure 5.7 shows the energy spectrum distribution at times $t = 0,\ 1/3$ and 2, for sample parameters $n = 1$, $E_0 = 0.1$ and $\gamma = 2$. As time progresses lower energy electrons are decelerated and absorbed by the background plasma, while high energy particles are largely unaffected. For comparison we have plotted a spectrum with index $\gamma = 3/2$, representing the physically observed hard spectrum limit (Holman *et al.*, 2003). Clearly the current analysis predicts

hardening of the electron spectrum past observed limits, and is therefore too simplistic to describe realistic flare particle energetics. The extra turbulent effects of the full Fokker-Planck equation may help to soften the spectrum somewhat. We note that the recent study of Drake *et al.* (2013) predicts a $F \sim E^{-3/2}$ spectrum resulting from a multi-island reconnecting system, as long as the characteristic electron energy loss time is larger than the acceleration time.

Further examination of flare particle spectra is outside the scope of this thesis – the above example is purely an illustration of one mathematical approach towards extracting information from a Fokker-Planck system. While the full equation may only be solvable via a numerical simulation, we now show that considering the Fokker-Planck equation as a system of stochastic differential equations can quickly provide moment equations. These give valuable insight into the system's properties and how it will evolve.

5.5.3 Hard X-ray emission

A stochastic analysis of the Fokker-Planck equation (5.59) by Conway *et al.* (1998) gave a prediction for the dependence on density of hard X-ray production in coronal loops. While our goal is to illustrate how the stochastic equations can quickly lead to useful moment equations, we also obtain a generalisation of the Conway result.

Consider the coronal loop as shown in Figure 5.6 and take the spatial coordinate z to be zero at the injection point. The hard X-ray emission rate $\mathcal{R}$ in this region will be proportional to nM_L, where M_L is number of electrons in the loop top. The number of electrons in the region will evolve according to

$$\frac{\partial M_L}{\partial t} = I - \frac{M_L}{\tau_L},$$

where I is the rate of injection and τ_L is the time for an electron to leave the loop top. Assuming a steady state situation with a constant rate of injection

(M_L, I constant) we can express the hard X-ray emission rate via

$$\mathcal{R} \propto n\tau_L. \tag{5.70}$$

To obtain an expression for τ_L we need to consider how the distribution will spread from the point of injection. In other words, we need to calculate the variance $Var(z) = \langle z^2 \rangle - \langle z \rangle^2$. Conway *et al.* (1998) gave an expression for the variance for small times

$$Var(z) \sim \left(\frac{n v_0^3}{6 N_s} \right) t^3, \tag{5.71}$$

where $N_s(v_0) = m_e^2 v_0^4 / 16\pi e^4 \lambda_{ei}$ is the column depth that is required to reduce an electron's speed to zero. This result assumes the simple initial condition (corresponding to a population of n electrons injected with speed $v = v_0$ at $z = 0$, all with pitch angle $\mu = 0$)

$$f(z,\, \mu,\, v,\, t = 0) = n\, \delta(\mu)\, \delta(z)\, \delta(v - v_0). \tag{5.72}$$

In our dimensionless notation (5.71) becomes

$$Var(z) \sim \frac{2}{3} t^3. \tag{5.73}$$

By taking $Var(z) = L^2$ at $t = \tau_L$, and using equation (5.70), equation (5.71) leads to a hard X-ray emission dependence on density of $\mathcal{R} \propto n^{2/3}$. We generalise this result by using the (dimensional) initial condition

$$f(z,\, \mu,\, v,\, t = 0) = n\, M(\mu)\, \delta(z)\, \delta(v - v_0), \tag{5.74}$$

where $M(\mu)$ is an arbitrary function, with mean μ_0 and variance σ_0^2, subject to the condition (from equation (5.31))

$$\int_{-1}^{1} M(\mu)\, \mathrm{d}\mu = 1. \tag{5.75}$$

The non-dimensionalised form of our initial condition is

$$f(z,\, \mu,\, v,\, t = 0) = n\, \frac{v_0^5}{D} M(\mu)\, \delta(z)\, \delta(v - 1),$$

and we note that taking the initial distribution

$$F(z,\, \mu,\, v) = n\, M(\mu)\, \delta(z)\, \delta(v - 1), \tag{5.76}$$

and solving equation (5.59) allows solutions with arbitrary initial velocities to be generated (MacKinnon and Craig, 1991).

We use equations (5.36) and (5.37) to convert the Fokker-Planck equation (5.59) to a series of stochastic equations, giving

$$\begin{aligned} \mathrm{d}z &= \mu v \,\mathrm{d}t, & (5.77)\\ \mathrm{d}v &= -\frac{1}{v^2}\,\mathrm{d}t, & (5.78)\\ \mathrm{d}\mu &= -\frac{2\mu}{v^3}\,\mathrm{d}t + \sqrt{2\frac{1-\mu^2}{v^3}}\,\mathrm{d}W(t). & (5.79) \end{aligned}$$

To calculate the moment equations we make use of Ito's formula (e.g., Gardiner, 2004 Chapter 4). A stochastic system of the form in equation (5.37) can be written in terms of some arbitrary function $h = h(\mathbf{s})$ via

$$\begin{aligned} \mathrm{d}h &= \left[D_i(\mathbf{s},\ t)\partial_i h + \frac{1}{2}[B(\mathbf{s},\ t)B^T(\mathbf{s},\ t)]_{ij}\partial_i\partial_j h\right]\,\mathrm{d}t \\ &\quad + B_{ij}(\mathbf{s},\ t)\partial_i h\,\mathrm{d}W_j(t). \end{aligned} \quad (5.80)$$

Using equations (5.77-5.79) we can write

$$\mathrm{d}h = \left[\mu v\frac{\partial h}{\partial z} - \frac{1}{v^2}\frac{\partial h}{\partial v} - \frac{2\mu}{v^3}\frac{\partial h}{\partial \mu} + \frac{1-\mu^2}{v^3}\frac{\partial^2 h}{\partial \mu^2}\right]\,\mathrm{d}t + \sqrt{2\frac{1-\mu^2}{v^3}}\frac{\partial h}{\partial \mu}\,\mathrm{d}W. \quad (5.81)$$

The first order moments are found by substituting μ and z in to (5.81) and averaging. Solving the resultant equations we obtain

$$\begin{aligned} \langle \mu \rangle &= \mu_0(1-3t)^{2/3}, & (5.82)\\ \langle z \rangle &= \mu_0\left(t - \frac{3t^2}{2}\right). & (5.83) \end{aligned}$$

Calculation of $\langle z^2 \rangle$ requires $\langle \mu^2 \rangle$ and $\langle \mu z \rangle$. Some algebraic manipulation leads to

$$\begin{aligned} \left\langle \mu^2 \right\rangle &= \frac{1-(1-3(\sigma_0^2+\mu_0^2))(1-3t)^2}{3}, & (5.84)\\ \langle \mu z \rangle &= \frac{(1-3t)^{2/3}}{3}\left[-\frac{1}{2}(1-3t)^{2/3} + \frac{1}{8}(1-3(\sigma_0^2+\mu_0^2))(1-3t)^{8/3}\right. \\ &\quad \left. + \frac{3}{8} + \frac{3}{8}(\sigma_0^2+\mu_0^2)\right], & (5.85)\\ \left\langle z^2 \right\rangle &= \frac{3(\sigma_0^2+\mu_0^2)-1}{168}(1-3t)^{14/3} + \frac{1}{24}(1-3t)^{8/3} \\ &\quad + \frac{1}{4}(1+\sigma_0^2+\mu_0^2)\left(t - \frac{3t^2}{2}\right) - \frac{(\sigma_0^2+\mu_0^2)}{56} - \frac{1}{28}. & (5.86) \end{aligned}$$

Using equations (5.83) and (5.86) we can now write the variance

$$\begin{aligned} Var(z) &= \frac{3(\sigma_0^2+\mu_0^2)-1}{168}(1-3t)^{14/3}+\frac{1}{24}(1-3t)^{8/3} \\ &\quad +\frac{1}{4}(1+\sigma_0^2+\mu_0^2)\left(t-\frac{3t^2}{2}\right)-\frac{(\sigma_0^2+\mu_0^2)}{56}-\frac{1}{28} \\ &\quad -\mu_0^2\left(t-\frac{3t^2}{2}\right)^2, \end{aligned} \tag{5.87}$$

which, when Taylor expanded for small t, gives

$$Var(z) \approx \sigma_0^2 t^2 + \frac{1}{3}(2-2\mu_0^2-11\sigma_0^2)t^3. \tag{5.88}$$

Equations (5.87) and (5.88) are new results - the expression of Conway *et al.* (5.73) is recovered for $\mu_0 = \sigma_0 = 0$. An important consequence of our result is that, for non-zero dispersion in the initial pitch angle distribution ($\sigma_0 \neq 0$), the first term in equation (5.88) will dominate at small times. If we express this in our dimensional variables we obtain

$$Var(z) \sim \sigma_0^2 v_0^2 t^2, \tag{5.89}$$

which leads to a stronger hard X-ray emission rate density dependence of $\mathcal{R} \propto n$ than in Conway *et al.* ($\mathcal{R} \propto n^{2/3}$). This result seems to be consistent with what one might expect from binary particle collisions - the emission rate would purely depend on the amount of target background particles.

This result helps to emphasise the convenience of working with the stochastic equations rather than the full Fokker-Planck equation – for one thing it allows us to go beyond the first order equations of the mean scattering approach. To further reinforce our result Figure 5.8 shows a comparison of the moment equations (5.82-5.84, 5.87) with a numerical simulation of equations (5.77-5.79), using 10000 particles and initial parameters $\sigma_0 = 0$ and $\mu_0 = 0.5$ ($M(\mu) = \delta(\mu - 0.5)$). Obviously there is good agreement between the analytical and numerical results – in particular the numerical results for variance are virtually indistinguishable from the analytical solution (5.87). The diffusion in pitch angle of the distribution is shown in Figure 5.9. The initial delta function spreads out until the distribution is completely diffuse and the particles have effectively rejoined the background plasma.

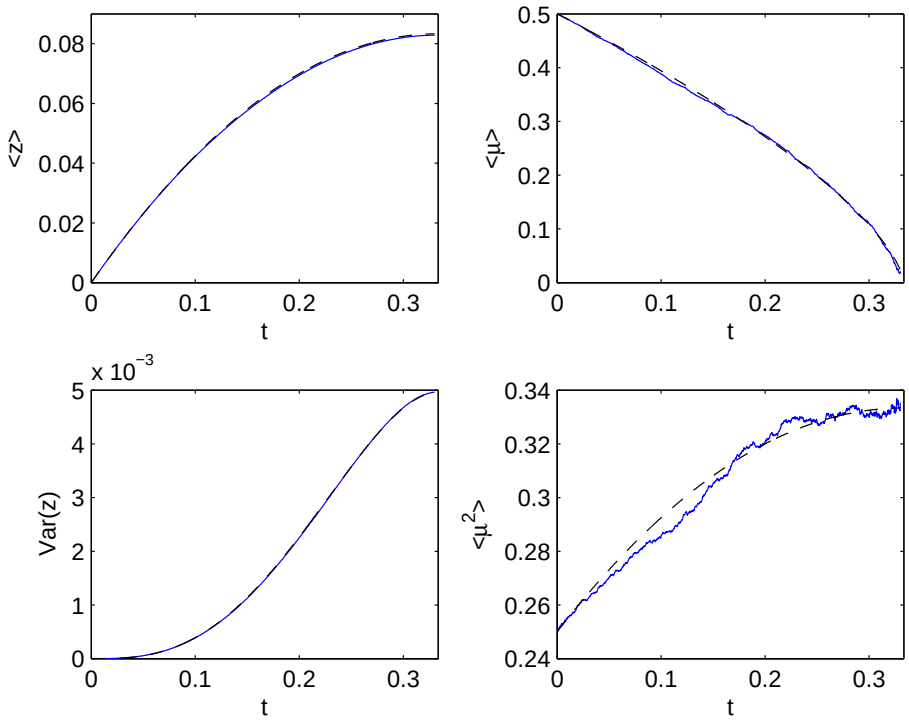

Figure 5.8: Comparison of simulation moments ($\langle z \rangle$, $\langle \mu \rangle$, $Var(z), \langle \mu^2 \rangle$) (solid line) and the moment solutions of equations (5.82-5.84, 5.87) (dashed lines) versus t. The simulation was run using 10000 particles and the initial parameters are $\sigma_0 = 0$ and $\mu_0 = 0.5$.

To complete our discussion of analytical techniques we briefly examine the diffusion approximation. For weakly anisotropic distributions, a diffusion equation can be obtained by integrating the Fokker-Planck equation with respect to pitch angle (Hasselmann and Wibberenz, 1970). Equally, if the particle distribution relaxes to a steady state, i.e. the pitch angle scattering time is much shorter than other characteristic time-scales, we should be able to set $\mathrm{d}\mu \approx 0$ in the stochastic equations (e.g. Litvinenko, 2012a; Litvinenko, 2012b).

To demonstrate this, by setting $\mathrm{d}\mu \approx 0$ in equation (5.79), we calculate the variance of our current example for an isotropic initial distribution. Combining equations (5.77) and (5.79) gives

$$\mathrm{d}z = v^3 \sqrt{\frac{1-\mu^2}{2v}}\, \mathrm{d}W(t). \tag{5.90}$$

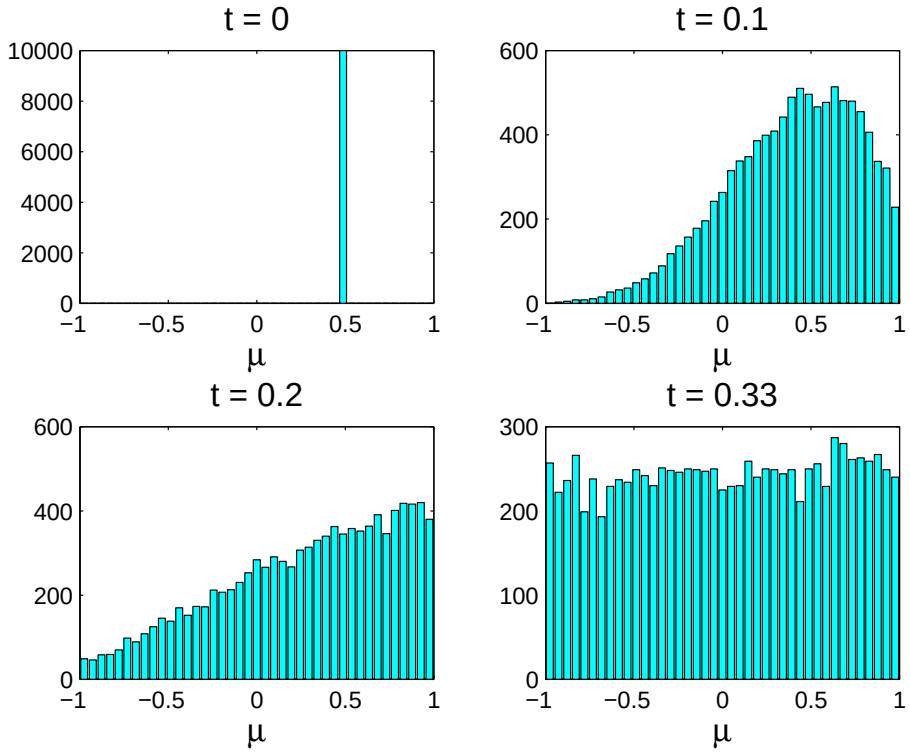

Figure 5.9: Pitch angle distribution (number of particles vs pitch angle cosine μ) at times $t = 0,\ 0.1,\ 0.2,\ 0.33$. The parameters are the same as in Figure 5.8 and the particles are distributed across 41 bins of uniform width.

This is equivalent to the diffusion equation

$$\frac{\partial F}{\partial t} = \frac{v^5}{6}\frac{\partial^2 F}{\partial z^2},$$

where $F = F(z, t)$ is the corresponding distribution function and we have integrated over pitch angle. We can multiply the diffusion equation by z^2 and integrate, giving

$$\frac{\partial \langle z^2 \rangle}{\partial t} = \frac{v^5}{3}. \tag{5.91}$$

An expression for v is found by integrating equation (5.78); substituting the result in (5.91) leads to a simple integral for $\langle z^2 \rangle$ in terms of t. The variance $Var(z) = \langle z^2 \rangle - \langle z \rangle^2$ can then be found by integrating and noting that $\langle z \rangle^2 = 0$, giving

$$Var(z) = \frac{1}{24}\left(1 - (1 - 3t)^{8/3}\right). \tag{5.92}$$

Figure 5.10 shows a comparison of equation (5.92) with a simulation of equations (5.77-5.79) using an isotropic ($\sigma_0^2 = 1/3,\ \mu_0 = 0$) initial distribution

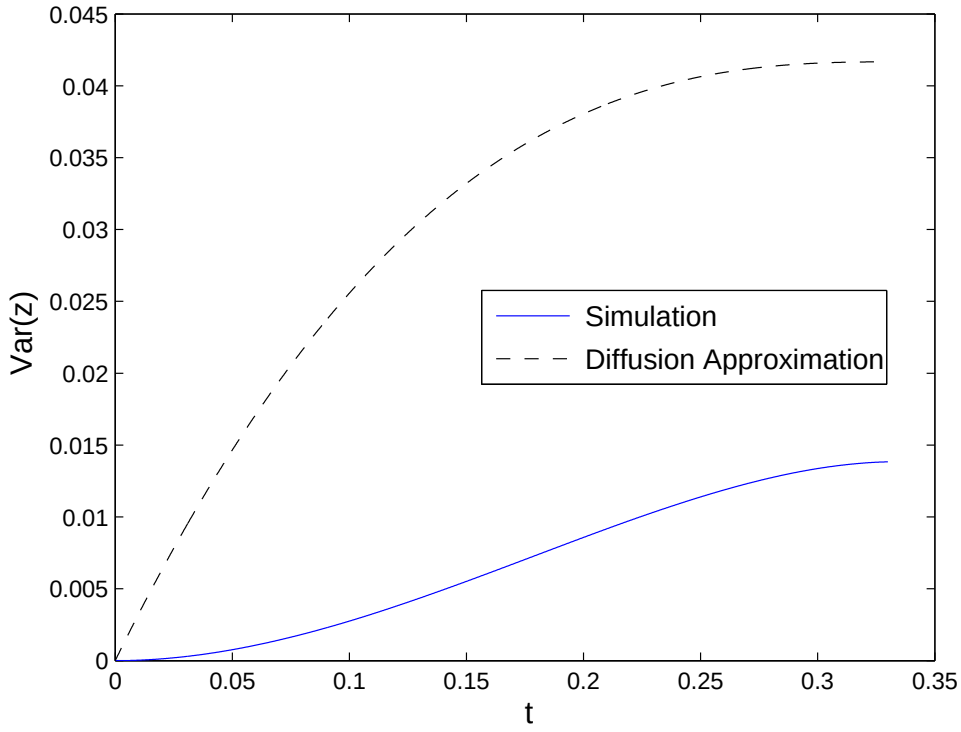

Figure 5.10: Comparison of Coulomb collision simulation $Var(z)$, and the diffusion approximation prediction of equation (5.92), versus t. The simulation was run using 30000 particles and the initial parameters are for an isotropic initial distribution ($\sigma_0^2 = 1/3$, $\mu_0 = 0$).

($M(\mu) = S(1+\mu)S(1-\mu)/2$ where S is the Heaviside step function). The distribution stays isotropic throughout its evolution – particle density remains evenly spread across the range of pitch angle. Note that the difference between the simulated variance and that predicted by equation (5.87) was found to be virtually indistinguishable – hence only the simulation results are displayed.

Clearly the diffusion approximation is not a good representation of the variance of our current example – it predicts far greater spatial spreading of the distribution. While the diffusion approximation is useful in, for example, cosmic-ray transport where momentum diffusion is neglected (Schlickeiser and Shalchi, 2008; Artmann *et al.*, 2011; Litvinenko, 2012a,b), it appears in our case that energy loss time-scales are of the same order as pitch angle scattering times. Obviously care must be taken when applying the diffusion approximation to some astrophysical situations.

5.6 Summary

In this chapter we have presented the equation we use to study particle acceleration and transport in the solar atmosphere, the Fokker-Planck equation. We have examined the equivalence of the Fokker-Planck and stochastic formulations and applied the results to two models of particle transport.

We outlined the Fokker-Planck equation and its form for charged particles in Section 5.2. Section 5.3 discussed the equivalence of the Fokker-Planck equation with a system of stochastic differential equations. Using a simple turbulent scattering model as a basis we numerically examined the equivalence of the Fokker-Planck and stochastic approaches in Section 5.4.

Section 5.5 examined electron transport in a coronal loop using several differing analytical approaches. In particular, using the stochastic formulation to calculate moment equations, we gave a generalisation to the result of Conway *et al.* (1998), which predicts a stronger hard X-ray emission rate density dependence.

We have seen that a stochastic formulation of a Fokker-Planck system provides attractive avenues for extracting useful information from the system. In the next chapter we shall use some of the analytical and numerical techniques discussed here to study cosmic-ray particle acceleration at the heliospheric termination shock.

Chapter 6

Modelling focused acceleration of cosmic-ray particles by stochastic methods

6.1 Introduction

The edge of the solar system is marked by the heliopause, where the constantly out-flowing solar wind meets the surrounding interstellar medium. While ionised particles from the interstellar medium are deflected by the far-reaching solar magnetic field, neutral gas flows through the turbulent boundary into the inner solar system (Isenberg, 1997; Reames, 1999). Here the gas can be ionized (either by interaction with a photon or with a solar wind ion) and the resulting "pick-up ions" are transported back outward along the solar magnetic field to the heliospheric termination shock, where the solar wind is slowed to sub-sonic speeds (Figure 6.1). It is what happens to the pick-up ions in the vicinity of the termination shock that serves as the setting for this chapter. In this region the pick-up ions are accelerated to great energies and become anomalous cosmic-rays. These particles are then flung out and can be detected through the shield of the Earth's atmosphere.

The primary mechanism for acceleration of the pick-up ions has long been

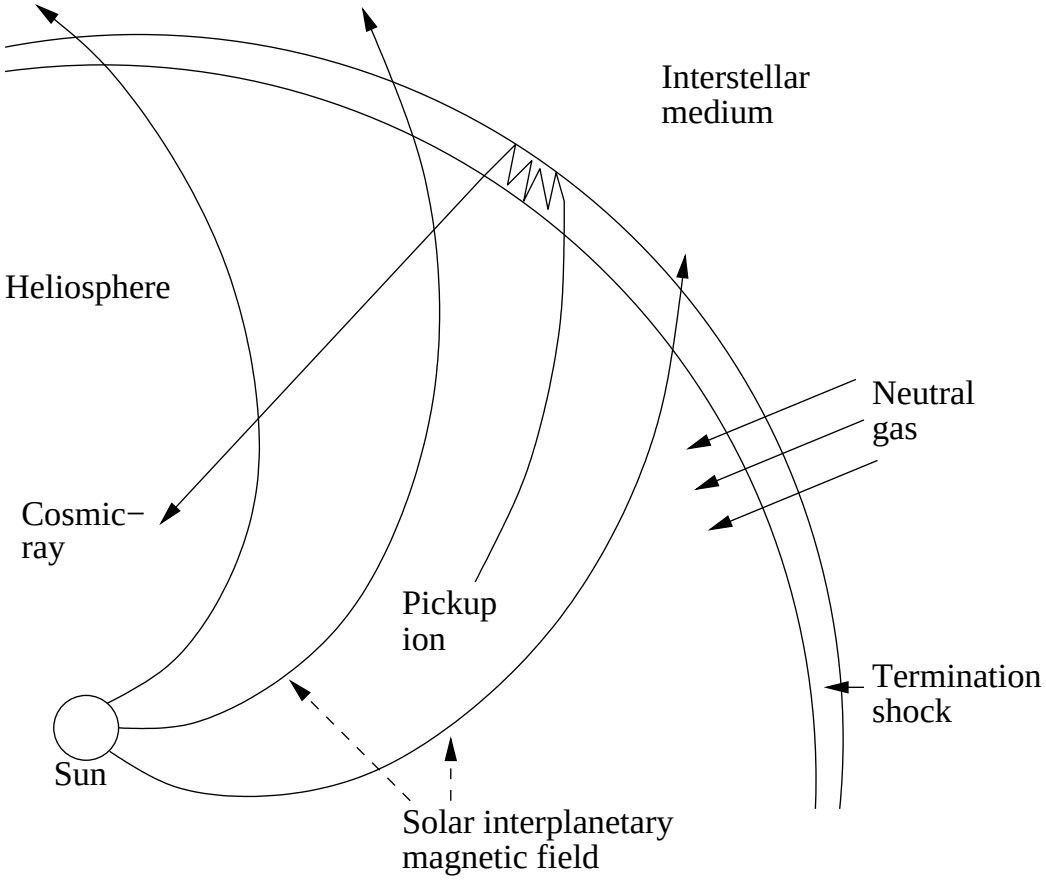

Figure 6.1: Anomalous cosmic ray acceleration. Neutral interstellar gas that flows into the solar system is ionised and picked up by the solar interplanetary magnetic field. These pick-up ions are transported to the termination shock, where they are accelerated to cosmic-ray energies.

believed to be diffusive shock acceleration (also known as first order Fermi acceleration - see Blandford and Eichler, 1987 for a review). Ionised particles are stochastically accelerated due to resonant interactions with turbulent magnetic fields at a shock. However, observations by the spacecraft Voyager in the vicinity of the termination shock have shown that, in contrast to the predictions of diffusive shock acceleration theory, anomalous cosmic-ray intensity does not peak at the shock itself (Stone *et al.*, 2008). This has necessitated more detailed models of cosmic-ray acceleration.

One of the physical effects that has been largely overlooked until recently is that of the force produced by a spatially varying magnetic field. In space, large scale guide fields are often significantly non-uniform. The Parker (1958) spiral, due to the rotation of the Sun, describes the solar interplanetary magnetic field

(Figure 6.1). Large scale spatial variations are also present in the galactic guide magnetic field perpendicular to the galactic plane (Sofue *et al.*, 1986). Spatial variations in a guide magnetic field have been shown to introduce an adiabatic focusing effect, whereby diverging or converging field lines induce a magnetic mirror force on propagating particles (Roelof, 1969).

Adiabatic focusing, coupled with the effect of scattering by the turbulent magnetic field, results in enhanced Fermi acceleration or deceleration of particles (Schlickeiser and Shalchi, 2008; see also Litvinenko and Schlickeiser, 2011). Whether this mechanism results in acceleration or deceleration of particles depends on the sign of the quantity $H_C L$. Here H_C is the magnetohydrodynamic wave cross helicity and L is the guide magnetic field focusing length (see Section 6.2.1 for full definitions). This mechanism has a number of potential astrophysical applications, including explaining the cosmic-ray distribution in the heliospheric termination shock region (Litvinenko and Schlickeiser, 2011) and in the interstellar medium (Schlickeiser, 2009).

A key result, derived by Schlickeiser and Shalchi (2008), is the prediction of the acceleration rate in terms of H_C and other parameters. This is based on several assumptions, however, and is only valid for a restricted parameter range (see Section 6.3 for details). A detailed examination of this result provides a central motivation for the present chapter. In particular, we explore the Fokker-Planck description of focused acceleration using a combination of analytical and numerical techniques.

We begin by presenting the Fokker-Planck equation and formulating it as a system of stochastic differential equations in Section 6.2.1. We then, in Section 6.2.2, specialise to a simplified case of the Fokker-Planck coefficients, and use arguments based on averaging to extend the Schlickeiser and Shalchi (2008) theory for the particular choice of the transport parameters in Section 6.3. Section 6.4 contains numerical simulations of the stochastic system, which are used to determine the distribution function in some indicative cases and to examine the analytical predictions and their limitations. Finally, in Section

6.5, we discuss our results and their implications for the focused acceleration mechanism in astrophysics.

6.2 Formulation of the stochastic system

6.2.1 Fokker-Planck equation and stochastic equations

The Fokker-Planck equation needs to model both scattering of particles due to waves and adiabatic focusing. To begin with we will outline the adiabatic focusing effect, which is due to spatially varying magnetic fields.

We start from the Boltzmann equation for the averaged distribution function $f_0(\mathbf{x}, \mathbf{p}, t)$,

$$\frac{\partial f_0}{\partial t} = -\mathbf{v} \cdot \nabla_{\mathbf{x}} f_0 - \frac{\partial \mathbf{p}}{\partial t} \cdot \nabla_{\mathbf{p}} f_0, \tag{6.1}$$

where, due to cosmic-ray particles being much higher in energy than background plasma, we have neglected particle-particle collisional effects (Kennel and Engelmann, 1966; Schlickeiser, 1989). Here $\nabla_{\mathbf{x}}$ and $\nabla_{\mathbf{p}}$ denote spatial and momentum gradient operators respectively. In a magnetic field $\mathbf{B}$ the particles will be influenced by the Lorentz force

$$\frac{\partial \mathbf{p}}{\partial t} = Ze\left(\mathbf{E} + \frac{1}{c}\mathbf{v} \times \mathbf{B}\right), \tag{6.2}$$

where Z is the particle charge in units of e and $\mathbf{E}$ is the electric field.

We consider the Boltzmann equation (6.1), subject to the Lorentz force (6.2), in the absence of an external electric field $\mathbf{E}$. We assume that the gyro-radius is small compared to magnetic field variations, resulting in axial symmetry for the magnetic field and distribution function (Schlickeiser and Jenko, 2010). Furthermore, neglecting density variations perpendicular to the field direction and using, for convenience, cylindrical polar coordinates for the momentum (e.g. p_z, $p_r = \sqrt{p_x^2 + p_y^2}$ and $\tan(p_\phi) = p_y/p_x$) allows us to write (Luhmann, 1976)

$$\frac{\partial f_0}{\partial t} = -v_z \frac{\partial f_0}{\partial z} - \frac{ZeB_r}{c}\left(v_\phi \frac{\partial}{\partial p_z} - v_z \frac{\partial}{\partial p_\phi}\right) f_0. \tag{6.3}$$

Here $f_0(z,\, p_z,\, p_\phi,\, t)$ is the spatially averaged gyrotropic distribution function. By considering Gauss's law for magnetism $\nabla \cdot \mathbf{B} = 0$ in cylindrical coordinates we get the relation

$$\frac{\partial}{\partial r}\left(rB_r\right) = -r\frac{\partial B_z}{\partial z}.$$

If we assume that changes in the magnetic field $\mathbf{B}$ occur on scales far greater than the particle gyro-radius then we can treat $\partial B_z/\partial z$ as constant in the above integration, resulting in

$$B_r = -\frac{r}{2}\frac{\partial B_z}{\partial z}. \tag{6.4}$$

Recalling equation (2.8) for the gyro-radius and substituting the above in (6.3) gives

$$\frac{\partial f_0}{\partial t} = -v_z\frac{\partial f_0}{\partial z} + \frac{v_\phi}{2B_z}\frac{\partial B_z}{\partial z}\left(p_\phi\frac{\partial}{\partial p_z} + p_z\frac{\partial}{\partial p_r}\right)f_0. \tag{6.5}$$

Defining the focusing length $L(z)$

$$\frac{1}{L} = -\frac{1}{B_z}\frac{\mathrm{d}B_z}{\mathrm{d}z}, \tag{6.6}$$

and writing the momentum in terms of spherical coordinates (e.g. $p_z = \mu p$, $p_\phi = \sqrt{1-\mu^2}\, p$) results in

$$\frac{\partial f_0}{\partial t} = -\mu v\frac{\partial f_0}{\partial z} - \frac{v}{2L}(1-\mu^2)\frac{\partial f_0}{\partial \mu}. \tag{6.7}$$

The second term on the right of equation (6.7) accounts for the effects of adiabatic focusing due to a spatially varying magnetic field. It arises from the adiabatic invariance of the magnetic moment

$$\mathcal{M} = \frac{mv^2}{2B}(1-\mu^2), \tag{6.8}$$

and is closely related to the magnetic mirror mechanism, where particles can be reflected when encountering strong magnetic fields (Priest and Forbes, 2000). For simplicity we will assume that the focusing length L is a positive constant - this assumption is robust as long as L is much larger than scattering length scales (Earl, 1976).

The adiabatic focusing term on the right of equation (6.7) modifies the full Fokker-Planck equation (5.24) to

$$\begin{aligned}\frac{\partial f_0}{\partial t} &= -\mu v\frac{\partial f_0}{\partial z} - \frac{v}{2L}(1-\mu^2)\frac{\partial f_0}{\partial \mu} \\ &\quad + \frac{1}{p^2}\frac{\partial}{\partial p}\left[p^2\left(D_{\mu p}\frac{\partial f_0}{\partial \mu} + D_{pp}\frac{\partial f_0}{\partial p}\right)\right] \\ &\quad + \frac{\partial}{\partial \mu}\left(D_{\mu\mu}\frac{\partial f_0}{\partial \mu} + D_{\mu p}\frac{\partial f_0}{\partial p}\right). \end{aligned} \tag{6.9}$$

The forms of the Fokker-Planck wave scattering coefficients $D_{\mu\mu}$, $D_{\mu p}$ and D_{pp} are presented in Section 6.2.2; we first seek to express (6.9) as a series of stochastic equations.

Similar to the simplification of equation (5.30), we may rewrite equation (6.9) in terms of the gyrotropic differential particle number density $f(z,\, p,\, \mu,\, t)$. This is related to f_0 by

$$f_0(z,\, p,\, \mu,\, t) = \frac{e^{-z/L}}{2\pi p^2} f(z,\, p,\, \mu,\, t). \tag{6.10}$$

The Fokker-Planck equation (6.9) can then be expressed in the form (Schlickeiser, 2011; Litvinenko and Schlickeiser, 2011)

$$\begin{aligned}\frac{\partial f}{\partial t} &= -\frac{\partial}{\partial z}\left(\mu v f\right) - \frac{\partial}{\partial \mu}\left[\left(\frac{v}{2L}(1-\mu^2) + \frac{\partial D_{\mu\mu}}{\partial \mu} + \frac{1}{p^2}\frac{\partial}{\partial p}(p^2 D_{\mu p})\right) f\right] \\ &\quad - \frac{\partial}{\partial p}\left[\left(\frac{\partial D_{\mu p}}{\partial \mu} + \frac{1}{p^2}\frac{\partial}{\partial p}(p^2 D_{pp})\right) f\right] \\ &\quad + \frac{\partial^2}{\partial \mu^2}(D_{\mu\mu} f) + \frac{\partial^2}{\partial \mu \partial p}(2 D_{\mu p} f) + \frac{\partial^2}{\partial p^2}(D_{pp} f). \end{aligned} \tag{6.11}$$

Using equations (5.36) and (5.37) with equation (6.11) we identify $\mathbf{s} = (z(t),\, \mu(t),\, p(t))$,

$$\mathbf{D} = \begin{pmatrix} \mu v \\ \frac{v}{2L}(1-\mu^2) + \frac{\partial D_{\mu\mu}}{\partial \mu} + \frac{1}{p^2}\frac{\partial (p^2 D_{\mu p})}{\partial p} \\ \frac{\partial D_{\mu p}}{\partial \mu} + \frac{1}{p^2}\frac{\partial (p^2 D_{pp})}{\partial p} \end{pmatrix}$$

and

$$B = \begin{pmatrix} 0 & 0 & 0 \\ 0 & \sqrt{2D_{\mu\mu}} & 0 \\ 0 & \sqrt{\frac{2D_{\mu p}^2}{D_{\mu\mu}}} & \sqrt{2D_{pp} - \frac{2D_{\mu p}^2}{D_{\mu\mu}}} \end{pmatrix}$$

as long as $D_{\mu\mu} > 0$ and $D_{pp} \geq D_{\mu p}^2/D_{\mu\mu}$. Thus equation (6.11) is replaced by the stochastic system

$$\begin{aligned}
\mathrm{d}z &= \mu v \,\mathrm{d}t, && (6.12)\\
\mathrm{d}\mu &= \left[\frac{v}{2L}(1-\mu^2) + \frac{\partial D_{\mu\mu}}{\partial \mu} + \frac{1}{p^2}\frac{\partial}{\partial p}(p^2 D_{\mu p})\right] \mathrm{d}t \\
&\quad + \sqrt{2D_{\mu\mu}}\,\mathrm{d}W_2(t), && (6.13)\\
\mathrm{d}p &= \left[\frac{\partial D_{\mu p}}{\partial \mu} + \frac{1}{p^2}\frac{\partial}{\partial p}(p^2 D_{pp})\right] \mathrm{d}t + \sqrt{\frac{2D_{\mu p}^2}{D_{\mu\mu}}}\,\mathrm{d}W_2(t) \\
&\quad + \sqrt{2D_{pp} - \frac{2D_{\mu p}^2}{D_{\mu\mu}}}\,\mathrm{d}W_3(t). && (6.14)
\end{aligned}$$

We now turn to the form of the Fokker-Planck coefficients under some simplifying assumptions.

6.2.2 Fokker-Planck coefficients and simplifying assumptions

The Fokker-Planck scattering coefficients account for turbulence due to forward and backward travelling transverse Alfvén waves. These waves may be either left- or right-hand polarised and may have differing intensities. The forms of the coefficients are obtained by using quasi-linear theory (Kennel and Engelmann, 1966; Jokipii, 1966; Luhmann, 1976), where the magnetic field (along with the electric field and distribution function) is separated into an averaged guide field component (e.g. B) and a rapidly fluctuating turbulent component (e.g. δB). The coefficients are (see Schlickeiser, 1989 or Schlickeiser, 2002 for a review)

$$\begin{aligned}
D_{\mu\mu} &= \tilde{D}(1-\mu^2)N, && (6.15)\\
D_{\mu p} &= \epsilon p \tilde{D}(1-\mu^2)M, && (6.16)\\
D_{pp} &= \epsilon^2 p^2 \tilde{D}(1-\mu^2)R, && (6.17)\\
\tilde{D} &= \frac{\pi}{2}(q-1) v k_{min}^{q-1} r_g^{q-2} \left(\frac{\delta B}{B}\right)^2. && (6.18)
\end{aligned}$$

Here r_g is the gyroradius, k_{min} is the minimum wavenumber, and $\epsilon = v_A/v$, where v_A is the Alfvén speed, is typically small (Litvinenko and Schlickeiser,

2011). The parameter q, being the spectral index of the assumed power law form of the power spectrum, governs the anisotropy of the scattering; $q \to 1$ corresponds to weakly anisotropic scattering. The functions N, M and R are given by (Luhmann, 1976; Schlickeiser, 1989; Dung and Schlickeiser, 1990)

$$\begin{aligned} N(\mu) &= (1+H_C)(1-\epsilon\mu)^2|\mu-\epsilon|^{q-1} \\ &\quad \times \left((1+\sigma^+)\, S[Z(\epsilon-\mu)] + (1-\sigma^+)\, S[Z(\mu-\epsilon)]\right) \\ &\quad +(1-H_C)(1+\epsilon\mu)^2|\mu+\epsilon|^{q-1} \\ &\quad \times \left((1+\sigma^-)\, S[-Z(\epsilon+\mu)] + (1-\sigma^-)\, S[Z(\epsilon+\mu)]\right), \quad (6.19) \\ M(\mu) &= (1+H_C)(1-\epsilon\mu)|\mu-\epsilon|^{q-1} \\ &\quad \times \left((1+\sigma^+)\, S[Z(\epsilon-\mu)] + (1-\sigma^+)\, S[Z(\mu-\epsilon)]\right) \\ &\quad -(1-H_C)(1+\epsilon\mu)|\mu+\epsilon|^{q-1} \\ &\quad \times \left((1+\sigma^-)\, S[-Z(\epsilon+\mu)] + (1-\sigma^-)\, S[Z(\epsilon+\mu)]\right), \quad (6.20) \\ R(\mu) &= (1+H_C)|\mu-\epsilon|^{q-1} \\ &\quad \times \left((1+\sigma^+)\, S[Z(\epsilon-\mu)] + (1-\sigma^+)\, S[Z(\mu-\epsilon)]\right) \\ &\quad +(1-H_C)|\mu+\epsilon|^{q-1} \\ &\quad \times \left((1+\sigma^-)\, S[-Z(\epsilon+\mu)] + (1-\sigma^-)\, S[Z(\epsilon+\mu)]\right). \quad (6.21) \end{aligned}$$

We recall that S is the Heaviside step function. The magnetic helicities σ^+ and σ^- indicate the polarization state of the forward and backward propagating Alfvén waves (Matthaeus and Goldstein, 1982). For multiple waves travelling in the positive direction, the magnetic helicity is given by $\sigma^+ = (I_L^+ - I_R^+)/I^+$ where I_L^+ and I_R^+ are the intensities of the left- and right-handed polarised waves respectively and $I^+ = I_L^+ + I_R^+$ is the total intensity. Similarly for waves travelling in the opposite direction $\sigma^- = (I_L^- - I_R^-)/I^-$. The cross helicity is

$$H_C = \frac{I^+ - I^-}{I^+ + I^-}, \quad (6.22)$$

which is a measure of the net directional intensity of the Alfvén waves.

Particles will be accelerated by "head-on" interactions with Alfvén waves, and slowed by "overtaking" interactions (Fermi, 1949). The addition of adiabatic focusing serves to enhance the effect of the acceleration if the particles are

focused towards the oncoming waves. If $L > 0$, as we have assumed, negative cross helicity will result in focused acceleration, while positive cross helicity will result in focused deceleration (Schlickeiser and Shalchi, 2008; Litvinenko and Schlickeiser, 2011). The greatest acceleration rates are due to large negative values of cross helicity ($H_C \to -1$, see Section 6.3.3 for details).

To achieve analytical progress, we make some physically motivated simplifying assumptions. As mentioned previously, one of the regions in which adiabatic focusing effects may be significant is the heliospheric termination shock region (Litvinenko and Schlickeiser, 2011). The Alfvén speed (2.13) is approximately $v_A \simeq 5 \times 10^6\,\mathrm{cm\,s^{-1}}$ both at 1 AU (Barnes, 1979) and at the termination shock (Li *et al.*, 2008). We therefore exploit the expedient of using a constant Alfvén speed, which is equivalent to the adoption of the background gas density partition scaling $n(z) \propto B^2(z)$ (e.g. Litvinenko and Schlickeiser, 2011). We consider speeds in the range $v_A \ll v \ll c$ and assume non-relativistic momenta, $p = mv$, so that the parameter $\epsilon = v_A/v \ll 1$. Finally Shalchi *et al.* (2009) argue that pitch angle scattering is isotropic for sufficiently strong turbulence, so we take $q \to 1$.

Taking the limit $\epsilon \to 0$ in N, M and R, and setting $\sigma^+ = \sigma^- = 0$ (no net polarisation), we may rewrite the Fokker-Planck coefficients in the non-relativistic limit as

$$D_{\mu\mu} = D_0(1-\mu^2), \tag{6.23}$$

$$D_{\mu p} = mv_A H_C D_0(1-\mu^2), \tag{6.24}$$

$$D_{pp} = m^2 v_A^2 D_0(1-\mu^2), \tag{6.25}$$

where $D_0 = 2\tilde{D}$ is a constant that represents the strength of the scattering.

The stochastic equations (6.12-6.14) become

$$\begin{aligned}
\mathrm{d}z &= \frac{\mu p}{m}\,\mathrm{d}t, && (6.26)\\
\mathrm{d}\mu &= \left[\frac{p}{2mL}(1-\mu^2) + 2D_0\left(mv_A H_C\frac{1-\mu^2}{p} - \mu\right)\right]\mathrm{d}t \\
&\quad +\sqrt{2D_0(1-\mu^2)}\,\mathrm{d}W_2(t), && (6.27)\\
\mathrm{d}p &= \left[2D_0 mv_A\left(mv_A\frac{1-\mu^2}{p} - H_C\mu\right)\right]\mathrm{d}t \\
&\quad +mv_A\sqrt{2D_0H_C^2(1-\mu^2)}\,\mathrm{d}W_2(t) \\
&\quad +mv_A\sqrt{2D_0(1-\mu^2)(1-H_C^2)}\,\mathrm{d}W_3(t). && (6.28)
\end{aligned}$$

We now non-dimensionalise the system using the parameters v_A and L.

6.2.3 Non-dimensionalisation

Substituting $z = L\,z^*$, $v = v_A v^*$ ($p^* = p/mv_A = v^*$), $D_0 = v_A D_0^*/L$ and $t = Lt^*/v_A$ in equations (6.26-6.28) results in

$$\begin{aligned}
\mathrm{d}z^* &= \mu p^*\,\mathrm{d}t^*, && (6.29)\\
\mathrm{d}\mu &= \left[\frac{p^*}{2}(1-\mu^2) + 2D_0^*\left(H_C\frac{1-\mu^2}{p^*} - \mu\right)\right]\mathrm{d}t^* \\
&\quad +\sqrt{2D_0^*(1-\mu^2)}\,\mathrm{d}W_2(t^*), && (6.30)\\
\mathrm{d}p^* &= \left[2D_0^*\left(\frac{1-\mu^2}{p^*} - H_C\mu\right)\right]\mathrm{d}t^* + \sqrt{2D_0^*H_C^2(1-\mu^2)}\,\mathrm{d}W_2(t^*) \\
&\quad +\sqrt{2D_0^*(1-\mu^2)(1-H_C^2)}\,\mathrm{d}W_3(t^*). && (6.31)
\end{aligned}$$

The equation set (6.29-6.31) is the dimensionless stochastic system that forms the basis of our analytical and numerical investigations. In the next section we analyse the system in some limiting cases using simple averaging arguments. The veracity of these arguments will be explored numerically in Section 6.4.

6.3 Analytic approximations based on the stochastic system

Initial analysis of the focused acceleration mechanism by Schlickeiser and Shalchi (2008) gave a prediction for the focused acceleration time scale

$t_{ac} = -3L/(H_C v_A)$, which in our dimensionless notation becomes

$$t^*_{ac} = -\frac{3}{H_C}. \tag{6.32}$$

This result applies in the case where the distribution remains almost isotropic and the focusing is weak. If, additionally, momentum diffusion can be neglected then the average momentum grows exponentially,

$$\frac{1}{\langle p^* \rangle} \frac{\mathrm{d}\langle p^* \rangle}{\mathrm{d}t^*} = -\frac{H_C}{3}, \tag{6.33}$$

with the greatest acceleration rates resulting from large negative values of cross helicity ($H_C \to -1$). The corresponding parameter range where these assumptions should hold is given by (Litvinenko and Schlickeiser, 2011)

$$\frac{1}{p^*} \ll \frac{(1-\mu^2)p^*}{D^*_0} \ll 1. \tag{6.34}$$

We will proceed to determine a correction to equation (6.33) for the particular set of parameters in Section 6.2 ($q = 1$, $\sigma^+ = \sigma^- = 0$, $\varepsilon \ll 1$) using simple averaging arguments. The averaged form of equations (6.30) and (6.31) are

$$\frac{\mathrm{d}\langle \mu \rangle}{\mathrm{d}t^*} = \frac{1}{2}\left\langle p^*(1-\mu^2) \right\rangle + 2D^*_0 \left(H_C \left\langle \frac{1-\mu^2}{p^*} \right\rangle - \langle \mu \rangle \right), \tag{6.35}$$

$$\frac{\mathrm{d}\langle p^* \rangle}{\mathrm{d}t^*} = 2D^*_0 \left(\left\langle \frac{1-\mu^2}{p^*} \right\rangle - H_C \langle \mu \rangle \right), \tag{6.36}$$

where, due to them having zero mean, the terms involving Wiener processes have disappeared. We now examine this system for various values of cross helicity H_C, corresponding to momentum diffusion, focused acceleration and focused deceleration.

6.3.1 Zero cross helicity, diffusive acceleration

In the case of zero cross helicity ($H_C = 0$), equation (6.36) results in

$$\frac{\mathrm{d}\langle p^* \rangle}{\mathrm{d}t^*} = 2D^*_0 \left\langle \frac{1-\mu^2}{p^*} \right\rangle.$$

Assuming the distribution is isotropic ($f \simeq f(p^*, z^*, t^*)$) gives $\langle \mu^2 \rangle = 1/3$. Further, if we assume that $\langle (1-\mu^2)/p^* \rangle \approx \langle 1-\mu^2 \rangle \langle 1/p^* \rangle \approx 2/(3\langle p^* \rangle)$ for

small dispersion in momentum, the average momentum will evolve according to

$$\langle p^* \rangle \simeq \left(\frac{8D_0^*}{3} t^* \right)^{1/2} + \langle p^* \rangle_0 \,, \tag{6.37}$$

with $\langle p^* \rangle_0$ the initial average momentum. Physically this result represents particle diffusion in momentum space (Schlickeiser and Shalchi, 2008).

6.3.2 Positive cross helicity, focused deceleration

For a distribution with $\langle \mu \rangle \approx 0$, equation (6.36) will result in an initial acceleration phase governed by pure momentum diffusion (equation (6.37)). In the case of positive cross helicity ($H_C > 0$), focused deceleration should eventually balance momentum diffusion, leading to a finite momentum $\langle p^* \rangle$ such that the right hand side of equation (6.36) vanishes. We therefore look for an equilibrium solution of equations (6.35) and (6.36). These combine to give

$$\left\langle p^*(1-\mu^2) \right\rangle = 4D_0^* \langle \mu \rangle (1 - H_C^2).$$

If we again assume near isotropy and $\langle p^*(1-\mu^2) \rangle \approx \langle p^* \rangle \langle 1-\mu^2 \rangle \approx 2/3 \langle p^* \rangle$ then we get

$$\langle p^* \rangle = 6D_0^* \langle \mu \rangle (1 - H_C^2).$$

Now we eliminate $\langle \mu \rangle$, using equation (6.36) together with $\langle 1/p^* \rangle \approx 1/\langle p^* \rangle$, and obtain an expression for the equilibrium momentum

$$\langle p^* \rangle_e = \left(\frac{4D_0^*}{H_C} (1 - H_C^2) \right)^{1/2}. \tag{6.38}$$

A measure of the time of transition to equilibrium can be obtained by substituting equation (6.38) in equation (6.37). This results in

$$t_{tr}^* = \frac{3}{8D_0^*} \left(\langle p^* \rangle_e - \langle p^* \rangle_0 \right)^2. \tag{6.39}$$

Physically, equation (6.38) gives the steady state average momentum of a near isotropic distribution of particles that have been subject to focused deceleration. Note that large positive values of cross helicity ($H_C \to 1$) in equation (6.38) result in steady state average momentum less than the Alfvén momentum, where our assumption of $v \gg v_A$ becomes invalid.

6.3.3 Negative cross helicity, focused acceleration

If particle speed is significantly larger than the Alfvén speed then $1/p^* \to 0$ and equations (6.35) and (6.36) become

$$\frac{\mathrm{d}\langle\mu\rangle}{\mathrm{d}t^*} = \frac{1}{2}\left\langle p^*(1-\mu^2)\right\rangle - 2D_0^*\langle\mu\rangle, \tag{6.40}$$

$$\frac{\mathrm{d}\langle p^*\rangle}{\mathrm{d}t^*} = -2H_C D_0^*\langle\mu\rangle. \tag{6.41}$$

If we search for a solution of the form

$$\langle p^*\rangle = \langle p^*\rangle_0 \exp(\alpha t^*), \tag{6.42}$$

where α is a constant, we get

$$\langle\mu\rangle = -\frac{\alpha\langle p^*\rangle_0}{2H_C D_0^*}\exp(\alpha t^*) \tag{6.43}$$

from equation (6.41). For strong scattering ($D_0^* \gg 1$) an initially isotropic distribution should remain isotropic for some period. Again assuming a weakly anisotropic distribution and $\langle p^*(1-\mu^2)\rangle \approx 2/3\langle p^*\rangle$, substituting our solutions in equation (6.40) and considering the physically interesting case of acceleration (i.e. take positive root and $H_C < 0$) gives

$$\alpha = D_0^*\left(\left(1-\frac{2H_C}{3D_0^*}\right)^{1/2} - 1\right) = -\frac{H_C}{3} - \frac{H_C^2}{18D_0^*} + \ldots \tag{6.44}$$

where the terms of order H_C^2 and higher provide a correction to equation (6.33). If scattering is strong, this correction is small.

An interesting question is how long it would take for the distribution to become anisotropic and, therefore, for the exponential acceleration solution to cease. Considering the exponential in equation (6.43) gives the timescale $t_{ac}^* = 1/\alpha \simeq -3/H_C$ (assuming a large value of D_0^*), the same result as the acceleration time scale (6.32).

Equations (6.42) and (6.44) represent the focused acceleration effect in Schlickeiser and Shalchi (2008) with a small correction. However the exponential increase in average pitch angle (equation (6.43)) will result in the distribution losing its isotropy. We now consider what happens in the case of large anisotropy for $t^* > t_{ac}^* = 1/\alpha$.

6.3.4 Negative cross helicity, particle beaming

The exponential growth of $\langle p^* \rangle$ and $\langle \mu \rangle$ in the case of $H_C < 0$ cannot continue unabated; the pitch angle is bounded by $|\mu| \leq 1$ and the distribution will become strongly anisotropic. Physically, as particles are accelerated, we might expect that after time $t^*_{ac} \gtrsim -3/H_C$ the particles will have aligned to the field, $\langle \mu \rangle \simeq 1$, and $\mathrm{d}\langle \mu \rangle / \mathrm{d}t^* \simeq 0$. This gives a large time momentum evolution equation of the form

$$\langle p^* \rangle = -2H_C D^*_0 t^* + \langle p^* \rangle_0 \,, \tag{6.45}$$

resulting in linear growth in momentum.

It is important to note how an initially isotropic distribution would evolve in the case of large negative values of cross helicity ($H_C \to -1$), corresponding to the greatest acceleration rates. The majority of particles will be accelerated by the mechanism of equation (6.42), and then at some later time beam along the direction of the guide magnetic field. However, the particles initially travelling opposite to the direction of acceleration will be decelerated before their direction of propagation reverses. These particles would not satisfy the requirement of our model $v \gg v_A$ for this turn-around period. We therefore choose lower values of cross helicity ($H_C = -0.3$) in our simulations. This decreases the amount of deceleration experienced and thus simplifies comparison with the analytical predictions.

To summarise the analytical arguments, Schlickeiser and Shalchi (2008) predict exponential growth of average momentum, assuming that momentum diffusion and rate of change of average pitch angle can be neglected and that the distribution is almost isotropic. We have obtained a correction to their prediction in a particular case of isotropic scattering. However, in the case of strong scattering, this correction is small. We have also given additional solutions in the cases of momentum diffusion, deceleration and acceleration. These predictions are now examined using a stochastic numerical treatment.

6.4 Stochastic simulations of cosmic-ray particle acceleration

6.4.1 Numerical simulation

Our aim is to examine the validity of the analytical predictions of Section 6.3 by solving equations (6.29-6.31) using an explicit Euler-Maruyama integration scheme (for a discussion see Higham., 2001). The code used is the same in operation as that described in Section 5.4.2. Specifically we want to explore the stochastic system in the following three cases: diffusive acceleration ($H_C = 0$), focused deceleration ($H_C > 0$) and focused acceleration ($H_C < 0$).

The parameters of the simulation are H_C and D_0^*. A number of particles are tracked by the code, each starting with coordinates z_0^*, p_0^* and μ_0; however, as there is no z^* dependency in our equations, and we are only interested in spatially averaged quantities, we can effectively ignore z^*. The particles are assumed to have initial speed equal to the Alfvén speed ($p_0^* = 1$) and to be isotropically distributed in pitch angle. This corresponds to the initial distribution

$$f_0(z_0^*, p_0^*, \mu_0) = \delta(z_0^*)\,\delta(p_0^* - 1)\,S(1 + \mu_0)\,S(1 - \mu_0),$$

where for simplicity, due to the linearity of the Fokker-Planck equation, we have ignored the normalisation constant and we recall that S is the Heaviside step function.

We take the non-relativistic condition $v \ll c$ to correspond to a non-dimensional upper limit of $p^* = v/v_A < 1000$. For an Alfvén speed of $v_A \simeq 5 \times 10^6\,\mathrm{cm\,s^{-1}}$ this limit restricts speeds to $v \simeq c/6$, with a corresponding relativistic Lorentz factor $\gamma \simeq 1.01$. A typical simulation may run for $30 - 60$ Alfvén times without exceeding the relativistic limit, and averaged momentum is measured at regular intervals.

As in Section 5.4 the time step is chosen to obey both the standard CFL and diffusion time step restrictions (e.g. equations (5.42) and (5.43)), result-

ing in the scale $\Delta t^* \sim 1/D_0^*$. In practice the physical fidelity of the system is checked by repeating the simulation with half the original timestep, until consistency and convergence of solution is reached. We choose particle numbers to maintain an adequate description of the distribution function, with numbers of order 10^4 found to provide a satisfactory representation (see Figure 6.8). Typically we use $50,000$ particles in the simulations presented below.

The stochastic nature of the simulation means that fluctuations in the calculated temporal derivative are inevitable. To alleviate the effect of this numerical artefact, a moving average smoothing algorithm (which averages across 9 data points) is applied to the underlying stochastic data. The simulated curves in Figures 6.2, 6.3, 6.6, 6.7 and 6.9 have been "smoothed" in this manner; however, as repeating the data analysis with other filters has shown, the results obtained are insensitive to the choice of algorithm.

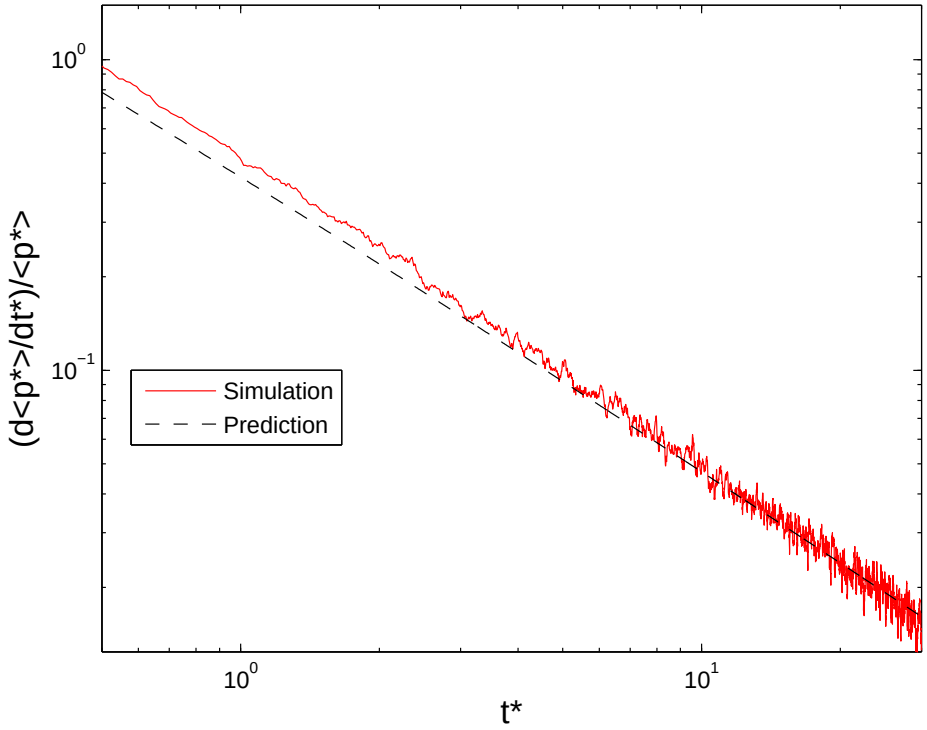

Figure 6.2: Comparison of simulation average momentum (Simulation) and the momentum diffusion solution of equation (6.37) (Prediction) versus t^*. The parameters are $H_C = 0$ and $D_0^* = 10$.

6.4.2 Zero cross helicity: momentum diffusion

Figure 6.2 shows evolution of average momentum in the case of zero cross helicity ($H_C = 0$) with the diffusion parameter value of $D_0^* = 10$, compared with the momentum diffusion theoretical prediction of equation (6.37). Note that, even with a smoothing algorithm applied to the underlying stochastic data, fluctuations in the calculated temporal derivative are apparent. However, this does not change the qualitative result: the theoretical line is followed closely despite it being based on a number of simplifying assumptions, confirming the momentum diffusion prediction (6.37).

6.4.3 Positive cross helicity: focused deceleration

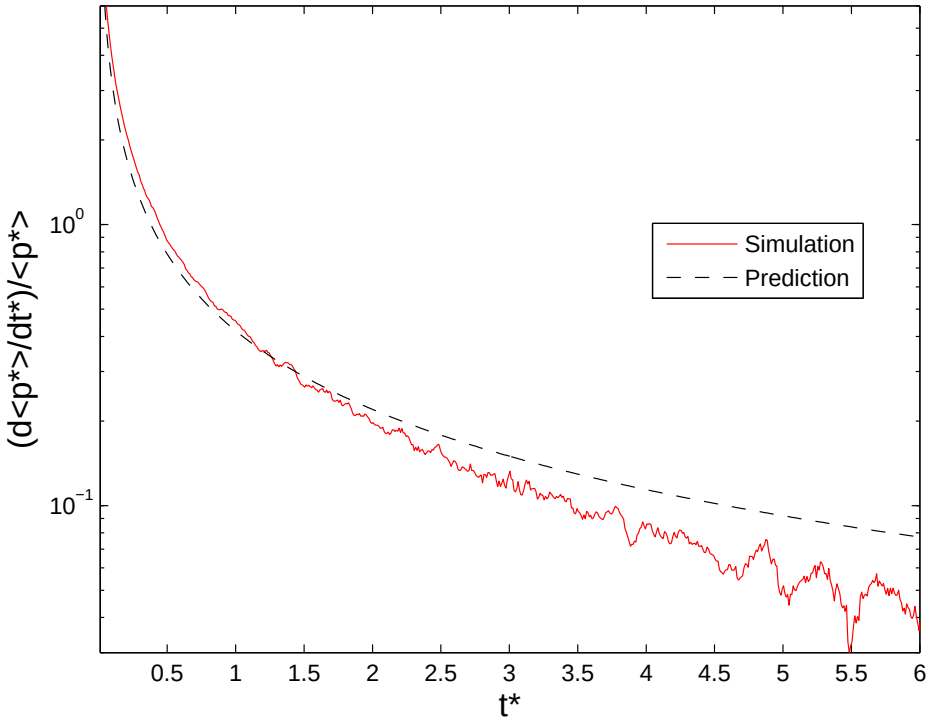

Figure 6.3: Comparison of simulation average momentum (Simulation) and the momentum diffusion solution of equation (6.37) (Prediction) versus t^*. The parameters are $H_C = 0.3$ and $D_0^* = 10$.

The case of $H_C > 0$ corresponds to focused deceleration of the particles. Figure 6.3 shows an early time comparison of a simulation run with the mo-

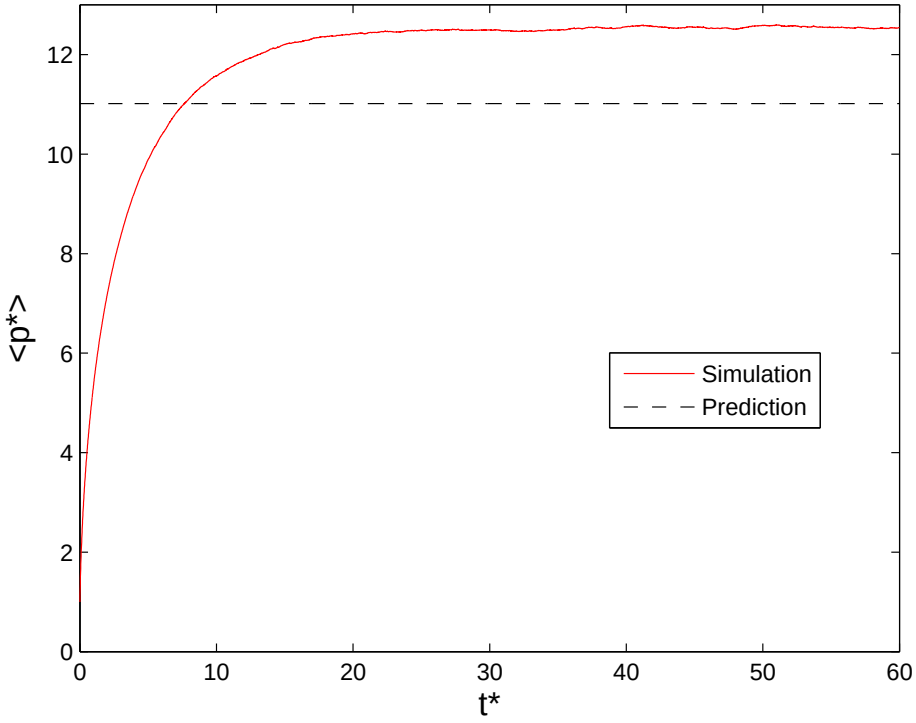

Figure 6.4: Comparison of simulation average momentum (Simulation) and the equilibrium solution of equation (6.38) (Prediction) versus t^*. The parameters are the same as in Figure 6.3.

mentum diffusion prediction of equation (6.37) for the diffusion parameter value of $D_0^* = 10$. The cross helicity parameter was chosen to be $H_C = 0.3$ for demonstrative purposes; values approaching $H_C = 1$ result in deceleration to the point where the particle speed can become lower than the Alfvén speed, which cannot be described by the model (see Section 6.3.2). While the initial ($t^* < 2$) agreement of the results with the momentum diffusion prediction is very good, non-zero positive cross helicity soon acts to decelerate the particles. This eventually results in an equilibrium state for the distribution. The close agreement of the simulation average momentum ($\langle p^* \rangle \rightarrow 12.6$) and the prediction of equation (6.38) ($\langle p^* \rangle_e \simeq 11$) is shown in Figure 6.4. The transition time scale from equation (6.39) is $t_{tr}^* \simeq 5$, at which time $\langle p^* \rangle$ (t_{tr}^*) $\simeq 10$. While this estimate is based on the additional assumption that pure momentum diffusion would continue until equilibrium is reached, it still gives a very good guide for the time of transition.

6.4.4 Negative cross helicity: focused acceleration

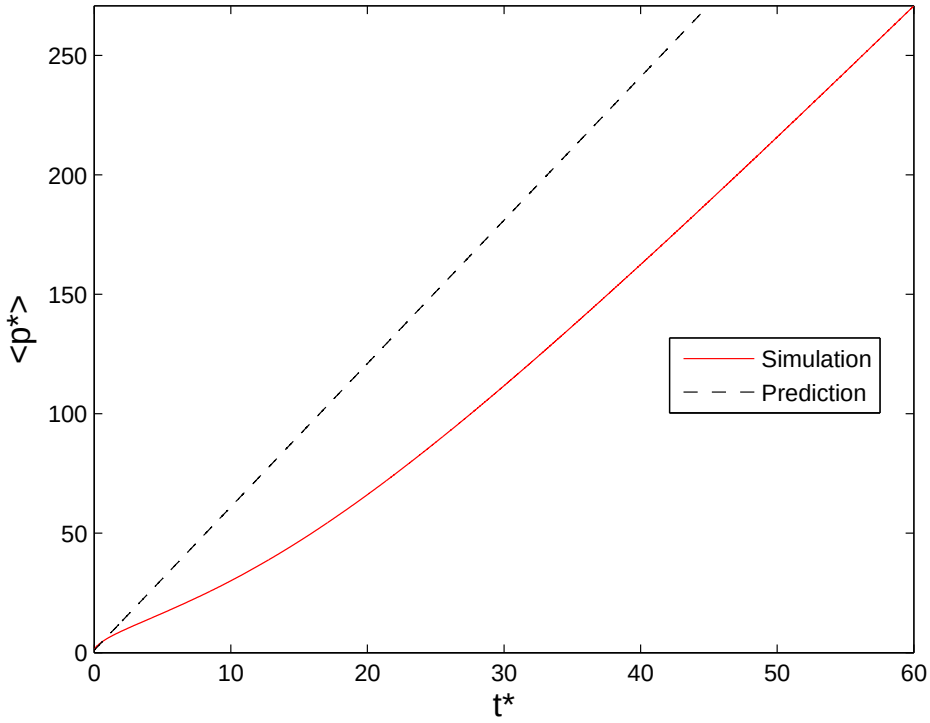

Figure 6.5: Comparison of simulated average momentum (Simulation) and the beaming solution of equation (6.45) (Prediction) versus t^*. The parameters are $H_C = -0.3$ and $D_0^* = 10$.

Simulations with values of cross helicity approaching $H_C \to -1$ resulted in a large proportion of particles being initially decelerated (see Section 6.3.4). This imposes significant restrictions on the upper limit of the time step. Additionally, the result of Schlickeiser and Shalchi assumes weak anisotropy; for these reasons $H_C = -0.3$ was chosen to provide the best opportunity to test the analytical predictions. Variation of this value only resulted in a scale factor difference, therefore we expect the behaviour for $H_C \to -1$ to be qualitatively the same.

Figure 6.5 shows the average momentum of the particle distribution as it evolves for the cross helicity value $H_C = -0.3$, compared with the particle beaming analytic prediction of equation (6.45). Note that after an initial quasi-exponential acceleration phase ($t^* \lesssim 20$) the average momentum increase

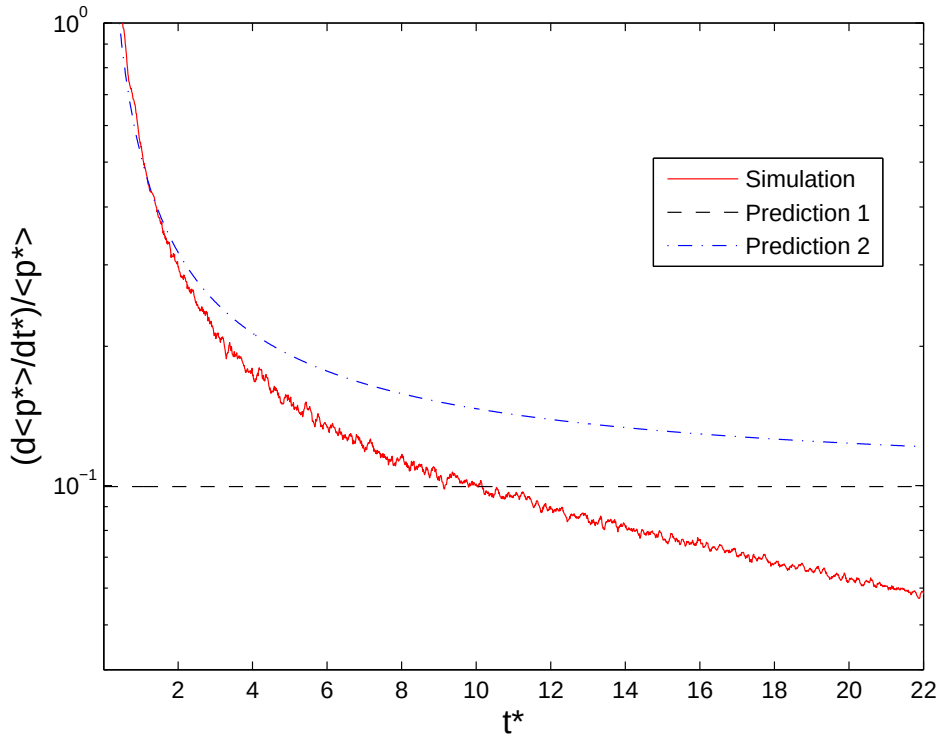

Figure 6.6: Comparison of average momentum evolution (Simulation) with the exponential focused acceleration solution of equation (6.42) (Prediction 1 - straight line) and the combined momentum diffusion and focused acceleration solutions of equations (6.37) and (6.42) (Prediction 2). The parameters are the same as in Figure 6.5.

becomes linear, with the simulation slope ($\mathrm{d}\langle p^*\rangle/\mathrm{d}t^* \simeq 5.5$) approaching the predicted slope of equation (6.45) ($\mathrm{d}\langle p^*\rangle/\mathrm{d}t^* = -2H_C D_0^* = 6$). The transition time prediction of equation (6.32) can be seen to be of the same order as the time taken for the simulation to switch to particle beaming ($t_{ac}^* = 10$ for $H_C = -0.3$). To examine the dependence on the diffusion parameter we performed a similar run with $D_0^* = 30$ and found the transition time to be insensitive to D_0^*, consistent with equation (6.32). The measured acceleration rates reinforced the beaming prediction of equation (6.45).

For the diffusion parameter value of $D_0^* = 10$ we might expect to see the exponential focused acceleration effect of equation (6.33) in the range $5 \lesssim \langle p^*\rangle \lesssim 15$. This is found, from the numerics, to roughly correspond to the time interval $1 \lesssim t^* \lesssim 5$. Figure 6.6 shows the initial acceleration phase,

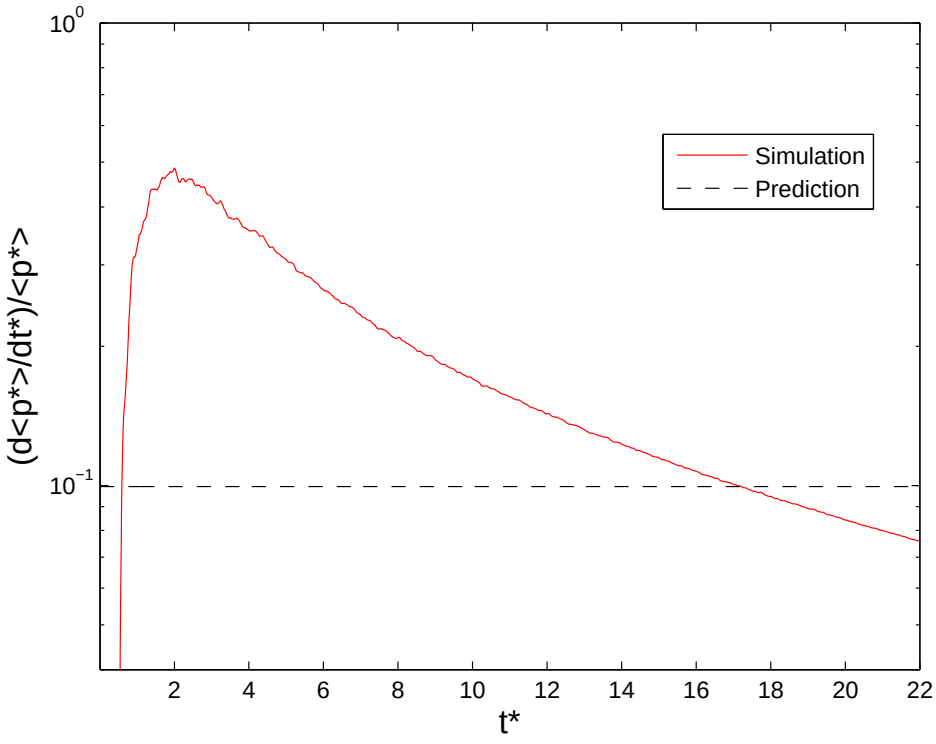

Figure 6.7: Comparison of simulated $-2H_C D_0^* \langle\mu\rangle$ (Simulation) with the exponential focused acceleration solution of equation (6.42) (Prediction). The parameters are the same as in Figure 6.5.

compared with the focused acceleration prediction of equation (6.42) and the combined results of momentum diffusion (6.37) and focused acceleration (6.42). Obviously momentum diffusion has a large effect on the distribution, with the small time ($t^* < 3$) evolution well described by the combined effects of momentum diffusion and focused acceleration. Within the approximate interval where focused acceleration should be evident it is clear that this effect alone is not sufficient to describe the behaviour.

To pin down the focused acceleration mechanism we attempted to isolate its effect. The focused acceleration term of equation (6.36), $-2H_C D_0^* \langle\mu\rangle$, is calculated independently of the momentum diffusion term (as in equation (6.41)) for the diffusion parameter value of $D_0^* = 10$, and then integrated numerically to give $\langle p^*\rangle$ (Figure 6.7). This expedient is not completely satisfactory, as removing the momentum diffusion term from the momentum equation will not stop similar effects being present in the pitch angle equation (6.35). For this

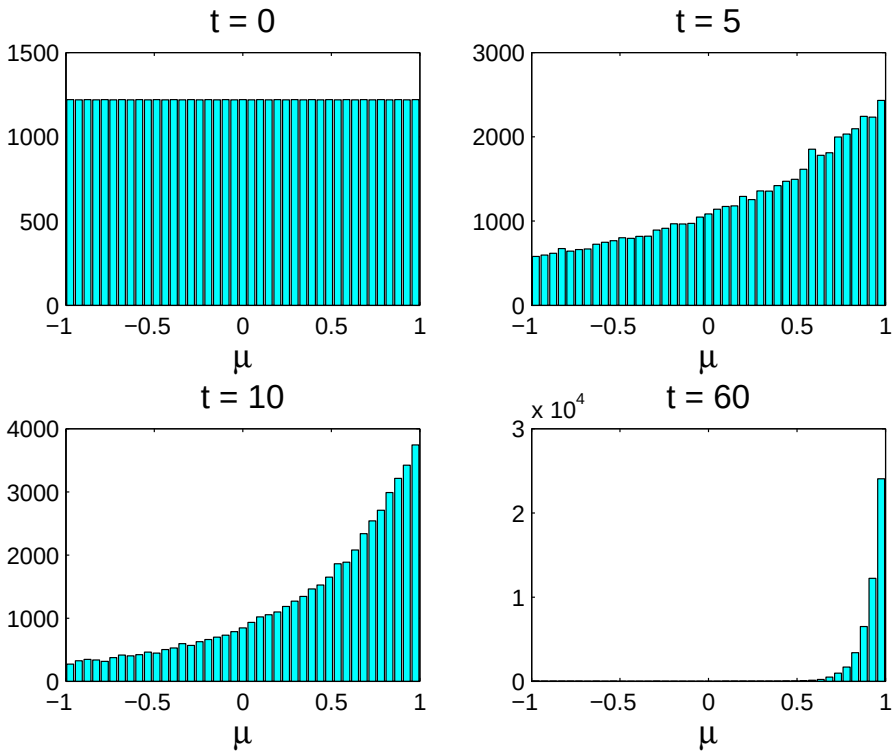

Figure 6.8: Pitch angle distribution (number of particles vs pitch angle cosine μ) at times $t = 0,\ 2,\ 4,\ 60$. The parameters are the same as in Figure 6.5 and the particles are distributed across 41 bins of uniform width.

reason we would expect the prediction of exponential growth (equation (6.42)) to be only approximately reached and indeed this appears to be the case, as evidenced by Figure 6.7.

Figure 6.8 illustrates how quickly the distribution becomes anisotropic. It shows the pitch angle distribution at times $t^* = 0,\ 5,\ 10$ and 60. By $t^* = 5$ we already have more than a factor of four difference between the number of forward and backward moving particles. By $t^* = 10$ this has grown to a factor of ten and by the end of the simulation effectively all of the particles are aligned to the positive z direction and $\langle\mu\rangle \simeq 1$.

Figure 6.9 shows the complete evolution. The initial acceleration phase ($t^* < 3$), described by the combined effects of momentum diffusion (6.37) and exponential focused acceleration (6.42), rapidly gives way to a transitional phase ($3 < t^* < 20$) as the distribution becomes anisotropic. The particles then continue to align themselves to the field, resulting in behaviour approaching

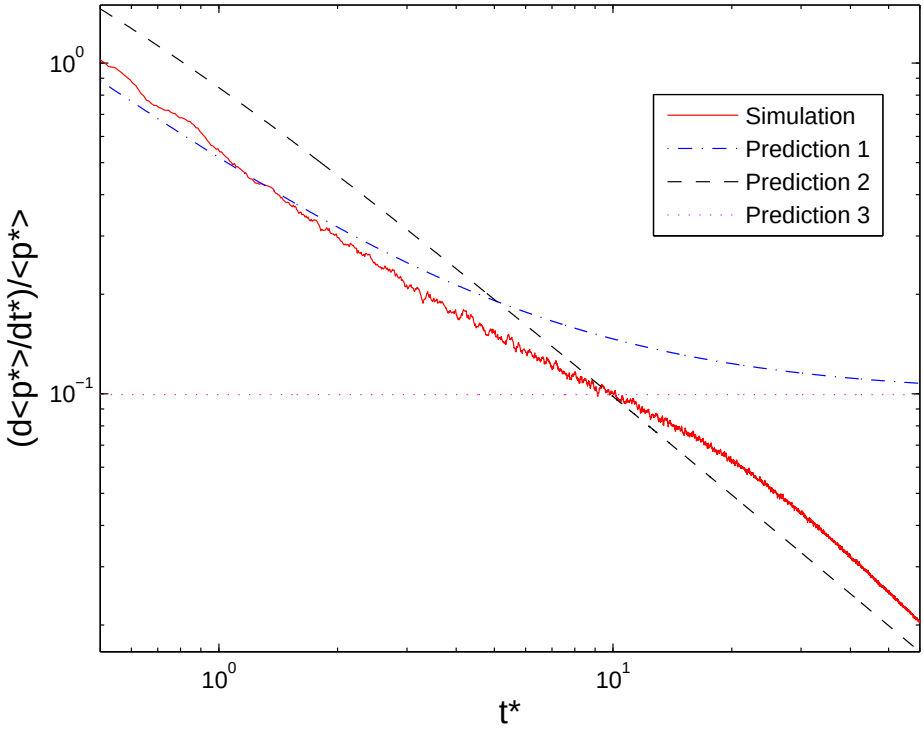

Figure 6.9: Comparison of average momentum evolution (Simulation) with the combined momentum and exponential focused acceleration solutions of equations (6.37) and (6.42) (Prediction 1), the beaming solution of equation (6.45) (Prediction 2) and the exponential focused acceleration solution of equation (6.42) (Prediction 3). The parameters are the same as in Figure 6.5.

the beaming solution of equation (6.45).

To sum up, the theory of Schlickeiser and Shalchi (2008) gives an accurate estimate for the focused acceleration rate when two conditions are satisfied. First, t^* (and hence p^*) is large enough to neglect momentum diffusion. Second, t^* is small enough to neglect anisotropy. We established that the second condition is very restrictive, since the anisotropisation time scale is of the same order as the acceleration time scale, and so the exponential growth in $\langle p^* \rangle$ can only occur for a few Alfvén times. Focused acceleration induces particles to align to the magnetic field, resulting in beaming behaviour and a much slower linear increase in average momentum. Finally, in considering the case of focused deceleration ($H_C L > 0$), we found reasonable quantitative agreement of the extended theory with the numerics. This reinforces the validity of both

our stochastic analytical and numerical treatments of the focused acceleration model.

6.5 Discussion and conclusions

The mechanism of acceleration via adiabatic focusing as described by the Fokker-Planck equation has been proposed by Schlickeiser and Shalchi (2008). In particular, the mechanism has been identified as having several potential astrophysical applications, including explaining the cosmic-ray distribution in the heliospheric termination shock region (Litvinenko and Schlickeiser, 2011) and in the interstellar medium (Schlickeiser, 2009). Notably, Schlickeiser and Shalchi (2008) derived the focused acceleration term for particle acceleration and gave a prediction for an acceleration time scale (equation (6.32)) using a diffusion approximation. In the case where momentum diffusion is neglected a simplified treatment predicts an exponential increase in average momentum (Litvinenko and Schlickeiser, 2011).

In this chapter we examined the mechanism of focused acceleration in two ways. Firstly, by using analytic arguments, based on representing the Fokker-Planck equation as a system of stochastic equations, we extended the theory of focused acceleration of cosmic-ray particles in the case of isotropic scattering and vanishing net magnetic helicity. Secondly we examined the veracity of the analytic predictions by computing the distribution function directly, using detailed numerical simulations. We again note that stochastic differential equations can be more convenient to work with than the original Fokker-Planck equation.

Our analysis shows that there is an interplay of momentum diffusion and focused acceleration, especially at small times, that cannot easily be separated (Figure 6.6). Momentum diffusion provides a significant effect over the range where focused acceleration might be expected to be the dominant mechanism.

Additionally, we demonstrated the limitations of assuming a near isotropic

pitch angle distribution (e.g. Litvinenko and Schlickeiser, 2011). Acceleration inevitably leads to strong anisotropy: the acceleration timescale of Schlickeiser and Shalchi is found to be of the same order as the timescale leading to anisotropy. Effectively this means that any exponential type growth in momentum will take place over a short period of a few Alfvén times. Later on the particle distribution will align to the guide magnetic field, resulting in a slower, linear, increase in average momentum (equation (6.45)). Within the significant limitations of the analysis presented in Section 6.3, our numerical results show reasonable quantitative agreement with the analytical predictions (e.g. Figure 6.4).

Our results lead us to speculate that, in order for the mechanism of Schlickeiser and Shalchi (2008) to be viable in astrophysical situations, some additional strong pitch angle scattering mechanism must be present to prevent the distribution from becoming anisotropic. On physical grounds it is reasonable to expect that the beamed particle distribution will quickly become unstable, creating waves that can scatter the particles. The Fokker-Planck equation would need to be supplemented with a wave equation, and the system solved self-consistently, to describe the resultant wave-particle interaction.

Chapter 7

Conclusions

7.1 Summary

In this thesis we set out to explore various physical phenomena of the solar atmosphere. In particular, we have focused our attention on the areas of solar flare energy release and particle acceleration.

Viscous energy dissipation has largely been overlooked as a substantial contributor to flare energy release. However, several studies have shown that viscous dissipation has the potential to exceed resistive dissipation in the active corona (e.g. Hollweg, 1986; Craig and Litvinenko, 2009).

An important issue with existing viscous models is that energy dissipation scalings predicted by simple, steady-state, scaling arguments are different depending on the assumed plasma flow profile. If a stagnation point flow profile is considered in Sweet-Parker style scaling arguments then, regardless of whether classical or the more physically relevant Braginskii (1965) ion parallel viscosity is included, a current sheet width scale consistent with Sweet-Parker ($x_s \simeq (\eta/B_s)^{1/2}$) is achieved (Craig and Litvinenko, 2010). Here the peak sheet magnetic field strength B_s is a parameter of order one. The above current sheet scale leads to the resistive dissipation scaling $W_\eta \simeq \eta^{1/2} B_s^{5/2}$ and, more significantly, constant (with resistivity) viscous dissipation $W_\nu \simeq \nu B_s^2$. It is important to note that optimal resistive dissipation occurs for $B_s \simeq 1$; if

the peak sheet magnetic field is allowed to build up ($B_s > 1$) then it will feed back on the plasma flow and stall the reconnection (saturation). The ratio of the dissipation rates

$$\frac{W_\nu}{W_\eta} \simeq \frac{\nu}{B_s^{1/2}\eta^{1/2}}, \tag{7.1}$$

predicts that viscous dissipation will dominate resistive dissipation for $\nu > \eta^{1/2}$. Considering that the viscous coefficient ν is up to ten orders of magnitude larger than the classical resistive coefficient η in the corona (Spitzer, 1962; Priest, 1982), equation (7.1) suggests that viscous dissipation can account for a significant fraction of the energy release of a solar flare. These scalings are backed up by existing exact solutions of the steady-state MHD equations in two and three dimensions (Sections 3.2.2 and 3.2.3) and recent 3D stagnation point time-dependent simulations (Craig and Litvinenko, 2009).

However, if a uniform Sweet-Parker style flow profile is assumed then a visco-resistive scale for the sheet width ($x_s \sim (\eta\nu)^{1/4}$) is the result. This leads to the significantly slower dissipation rates

$$W_\eta \sim W_\nu \sim \eta^{3/4}\nu^{-1/4}. \tag{7.2}$$

This visco-resistive scale has been found in time-dependent numerical simulations of tokamaks (Park *et al.*, 1984) and 2D X-point collapse (Craig *et al.*, 2005; Craig, 2010).

To clarify this issue and generally examine the properties of a viscous reconnecting current sheet, we performed a series of time-dependent planar simulations of reconnection that gave well-defined symmetric current layers in Chapter 3. A defining feature of the model is that the current sheets are supported by large scale vortical flows. Current layer thickness (x_s), inflow (v_{in}) and outflow (v_{out}) speeds, and viscous and resistive dissipation rates were calculated for simulations across a range of resistivities.

To robustly explore the significance of viscous effects, the amplitude of the magnetic disturbance was scaled to ensure optimal resistive dissipation rates ($B_s \simeq 1$). To provide a check on the results a control simulation was

performed, where the viscous parameter was scaled with resistivity to approximate a purely resistive situation. Then, for the main results, the viscous parameter was held fixed at a physically-based value using both the classical and Braginskii viscosity forms. Additionally, some exploratory runs for a sheared current layer were performed.

Our results were consistent with stagnation point flow profile scalings - we did not find any evidence of a visco-resistive scale. Somewhat surprisingly, the dissipation relation (7.1) was found to hold good regardless of the form of the viscosity used.

The scaling arguments and exact solutions detailed in Chapter 3 were derived assuming "head-on" reconnection in an "open geometry" (Craig and Litvinenko, 2010). Furthermore, the simulations of Section 3.3 were designed to give well defined, symmetrical, current layers with which the analytical models could be readily compared. In general, however, reconnecting coronal plasmas are likely to be highly non-uniform; it is not clear to what extent the relation (7.1) will hold. With this in mind, in Chapter 4, we endeavoured to explore viscous effects using a more general initial condition - a modified Orszag–Tang vortex (Orszag and Tang, 1979; Heerikhuisen *et al.*, 2000). Despite the less restrictive initial condition, the simulations produced long thin current sheets supported by stagnation point flows. To explore the applicability of relation (7.1) we performed a set of simulations where the amplitude of the magnetic disturbance was again scaled to ensure optimal resistive dissipation rates ($B_s \simeq 1$). Our results reinforced the results of the previous chapter - viscous dissipation was found to dominate resistive dissipation for $\nu \gg \eta^{1/2}$. No evidence was found of the visco-resistive scale.

We then turned to the question of the effect of saturation on dissipation scalings. Unlike our previous simulations, we no longer scaled the amplitude of the magnetic disturbance. As a result the sheet magnetic field was able to build up and feed back on the velocity field ($B_s > 1$). As realistic reconnection regions are unlikely to have their sheet strengths closely matched to the

external plasma properties, this approach provided a more physically robust test of the dissipation rate scaling (7.1).

Again, viscous dissipation was found to dominate resistive dissipation in the physically realistic limit $\nu \gg \eta^{1/2}$. While the feedback of the current sheet on the driving flow resulted in decreased resistive dissipation (and therefore small reconnection rates), the viscous dissipation rate increased. Relation (7.1) was again found to be a good predictor of energy release behaviour.

Unlike traditional models of resistive dissipation, where energy in the magnetic field can only be liberated by reconnection, our model draws significant energy from the velocity field that supports the reconnection. Overall, our results suggest that (7.1) provides a conservative limit for energy dissipation from current sheet reconnection driven by stagnation point flows. Furthermore, viscous energy dissipation is likely to make a significant contribution to the total solar flare energy budget.

Chapter 5 began our examination of plasma particle acceleration and transport. Accelerated particle distributions are common throughout the universe (e.g. Ackermann *et al.*, 2013) and are a natural consequence of solar flares (Priest and Forbes, 2000). To model particle acceleration we used the Fokker-Planck equation (Fokker, 1914), which models both particle advection and diffusion. One of the key techniques we used was the expression of the Fokker-Planck equation as an equivalent set of stochastic equations.

We numerically examined the equivalence of the Fokker-Planck and the stochastic methods in Section 5.4 using a simple turbulent particle scattering model. Using several different approaches we then examined electron transport in a coronal loop. An existing result was that particle distributions with no initial dispersion lead to a Hard X-Ray emission rate $\mathcal{R}$ with a dependence on background plasma density n of $\mathcal{R} \propto n^{2/3}$ (Conway *et al.*, 1998). We generalised this to non-zero dispersion in the initial distribution and found that Hard X-Ray emission rates are directly proportional to density ($\mathcal{R} \propto n$). Physically, this result seems to be indicative of what we would expect from

binary particle interactions - given an accelerated distribution, the emission rate should purely depend on the number of particles with which the electrons can collide.

In Chapter 6 we addressed the acceleration of anomalous cosmic-rays. In our model, ionised particles are accelerated via the dual effects of diffusive interactions with small-scale turbulent magnetic fields and adiabatic focusing due to the spatially varying guide magnetic field. The motivation for this chapter was provided by the analysis of Schlickeiser and Shalchi (2008) who gave a prediction for the (non-dimensional) acceleration timescale

$$t^*_{ac} = -\frac{3}{H_C}, \tag{7.3}$$

where the cross helicity H_C indicates the net strength and direction of the turbulent magnetic waves. If, additionally, momentum diffusion is neglected then this results in exponential growth in averaged particle momentum ($\langle p^* \rangle$)

$$\frac{1}{\langle p^* \rangle} \frac{\mathrm{d} \langle p^* \rangle}{\mathrm{d}t^*} = -\frac{H_C}{3}. \tag{7.4}$$

By expressing the Fokker-Planck equation as a system of stochastic equations we were able to give predictions for averaged momentum evolution in the cases of diffusive acceleration ($H_C = 0$), focused deceleration ($H_C > 0$) and focused acceleration ($H_C < 0$). In particular, we obtained a correction to equation (7.4)

$$\frac{1}{\langle p^* \rangle} \frac{\mathrm{d} \langle p^* \rangle}{\mathrm{d}t^*} = D^*_0 \left(\left(1 - \frac{2H_C}{3D^*_0} \right)^{1/2} - 1 \right), \tag{7.5}$$

where D^*_0 represents the scattering strength. Equation (7.4) is recovered for strong scattering (D^*_0 large). These results were then used to interpret numerical simulations of the various cases.

Two important points were evident from our study. The first was that the effect of momentum diffusion cannot be disregarded in the initial stages of acceleration - it provides a significant contribution during the times when focused acceleration might be expected to dominate. The second point was that the distribution can quickly become anisotropic. In the case of focused

acceleration this results in slower, linear, growth in momentum. For focused acceleration to be a viable particle acceleration mechanism, therefore, some additional strong scattering mechanism must be present to prevent the distribution becoming anisotropic.

7.2 Suggestions for further work

The work of this thesis could be extended in several areas. To better understand the effects of saturation it could be informative to return to the head-on simulation of Chapter 3. By allowing the sheet to saturate we could better examine the properties of the current layer, in addition to the energy dissipation rates.

The reconnection simulations could be extended to include axial fields (Craig and Litvinenko, 2007, performed this type of calculation in an X-point geometry) for both forms of the viscosity. We might expect to see significant differences in more than two dimensions due to the anisotropy of the Braginskii tensor; depending on the orientation of the merging fields, Braginskii viscosity may have a negligible effect (Craig and Litvinenko, 2009). Fully three dimensional studies are also obviously an important next step. Recent examinations of fan (Craig and Litvinenko, 2009) and spine (Craig and Lopez, 2013) reconnecting systems have shown strong viscous dissipation rates, even in the presence of weak reconnection. Some exploratory work on the effect of saturation on fully 3D current layers could be useful.

The addition of turbulent or compressible effects could have significant effect on dissipation scalings, so the inclusion of these in theory and simulations would be of interest. From an observational standpoint, identifying whether large-scale non-uniform flows are a signature of flaring plasmas would help lend weight to the idea that viscous dissipation is a significant contributor in solar flare energy release.

Finally, the work of Chapter 6 lends itself to extension in a couple of ways.

An anisotropic particle distribution may quickly become unstable, creating waves that would cause further scattering. Supplementing the Fokker-Planck equation with a wave equation and solving the system self-consistently may therefore clarify whether focused acceleration is a viable mechanism for particle acceleration. In addition, generalising to non-isotropic pitch-angle scattering, non-isotropic initial distributions, or non-vanishing net magnetic helicity may have significant impact on acceleration rates. As a general comment the expression of the Fokker-Planck equation as a series of stochastic equations is likely to be useful in many physical situations where a Fokker-Planck description is appropriate; stochastic equations allow for relatively simple calculation of moment equations that may not otherwise be obtainable from the full Fokker-Planck equation, and can be very accessible numerically.

Appendix A

Second order spherical polar partial derivatives

Second order Cartesian momentum (p_x, p_y, p_z) partial derivatives in terms of spherical polars (p, μ, ϕ) are given by

$$\begin{aligned}
\frac{\partial^2}{\partial {p_x}^2} &= (1-\mu^2)\cos^2\phi\frac{\partial^2}{\partial p^2} + \frac{\mu^2\cos^2\phi + \sin^2\phi}{p}\frac{\partial}{\partial p} \\
&+\frac{\mu^2(1-\mu^2)\cos^2\phi}{p^2}\frac{\partial^2}{\partial\mu^2} + \frac{\mu(3\cos^2\phi(1-\mu^2)-1)}{p^2}\frac{\partial}{\partial\mu} \\
&+\frac{\sin^2\phi}{p^2(1-\mu^2)}\frac{\partial^2}{\partial\phi^2} + \frac{2\sin\phi\cos\phi}{p^2(1-\mu^2)}\frac{\partial}{\partial\phi} \\
&-\frac{2\mu(1-\mu^2)\cos^2\phi}{p}\frac{\partial^2}{\partial\mu\partial p} + \frac{2\mu\sin\phi\cos\phi}{p^2}\frac{\partial^2}{\partial\phi\partial\mu} \\
&-\frac{2\sin\phi\cos\phi}{p}\frac{\partial^2}{\partial\phi\partial p}, \qquad \text{(A.1)} \\
\frac{\partial^2}{\partial {p_y}^2} &= (1-\mu^2)\sin^2\phi\frac{\partial^2}{\partial p^2} + \frac{\mu^2\sin^2\phi + \cos^2\phi}{p}\frac{\partial}{\partial p} \\
&+\frac{\mu^2(1-\mu^2)\sin^2\phi}{p^2}\frac{\partial^2}{\partial\mu^2} + \frac{\mu(3\sin^2\phi(1-\mu^2)-1)}{p^2}\frac{\partial}{\partial\mu} \\
&+\frac{\cos^2\phi}{p^2(1-\mu^2)}\frac{\partial^2}{\partial\phi^2} + \frac{2\sin\phi\cos\phi}{p^2(1-\mu^2)}\frac{\partial}{\partial\phi} \\
&-\frac{2\mu(1-\mu^2)\sin^2\phi}{p}\frac{\partial^2}{\partial\mu\partial p} - \frac{2\mu\sin\phi\cos\phi}{p^2}\frac{\partial^2}{\partial\phi\partial\mu} \\
&+\frac{2\sin\phi\cos\phi}{p}\frac{\partial^2}{\partial\phi\partial p}, \qquad \text{(A.2)} \\
\frac{\partial^2}{\partial {p_z}^2} &= \mu^2\frac{\partial^2}{\partial p^2} + \frac{1-\mu^2}{p}\frac{\partial}{\partial p} + \frac{(1-\mu^2)^2}{p^2}\frac{\partial^2}{\partial\mu^2} - \frac{3\mu(1-\mu^2)}{p^2}\frac{\partial}{\partial\mu} \\
&+\frac{2\mu(1-\mu^2)}{p}\frac{\partial^2}{\partial\mu\partial p}, \qquad \text{(A.3)}
\end{aligned}$$

$$\begin{aligned}
\frac{\partial^2}{\partial p_x \partial p_z} &= \mu\sqrt{1-\mu^2}\cos\phi\frac{\partial^2}{\partial p^2} - \frac{\mu\sqrt{1-\mu^2}\cos\phi}{p}\frac{\partial}{\partial p} \\
&\quad -\frac{\mu(1-\mu^2)^{3/2}\cos\phi}{p^2}\frac{\partial^2}{\partial\mu^2} + \frac{(3\mu^2-1)\sqrt{1-\mu^2}\cos\phi}{p^2}\frac{\partial}{\partial\mu} \\
&\quad +\frac{(1-2\mu^2)\sqrt{1-\mu^2}\cos\phi}{p}\frac{\partial^2}{\partial\mu\partial p} - \frac{\mu\sin\phi}{p\sqrt{1-\mu^2}}\frac{\partial^2}{\partial\phi\partial p} \\
&\quad -\frac{\sqrt{1-\mu^2}\sin\phi}{p^2}\frac{\partial^2}{\partial\phi\partial\mu}, \qquad \text{(A.4)} \\
\frac{\partial^2}{\partial p_y \partial p_z} &= \mu\sqrt{1-\mu^2}\sin\phi\frac{\partial^2}{\partial p^2} - \frac{\mu\sqrt{1-\mu^2}\sin\phi}{p}\frac{\partial}{\partial p} \\
&\quad -\frac{\mu(1-\mu^2)^{3/2}\sin\phi}{p^2}\frac{\partial^2}{\partial\mu^2} + \frac{(3\mu^2-1)\sqrt{1-\mu^2}\sin\phi}{p^2}\frac{\partial}{\partial\mu} \\
&\quad +\frac{(1-2\mu^2)\sqrt{1-\mu^2}\sin\phi}{p}\frac{\partial^2}{\partial\mu\partial p} + \frac{\mu\cos\phi}{p\sqrt{1-\mu^2}}\frac{\partial^2}{\partial\phi\partial p} \\
&\quad +\frac{\sqrt{1-\mu^2}\cos\phi}{p^2}\frac{\partial^2}{\partial\phi\partial\mu}, \qquad \text{(A.5)} \\
\frac{\partial^2}{\partial p_x \partial p_y} &= (1-\mu^2)\sin\phi\cos\phi\frac{\partial^2}{\partial p^2} + \frac{\mu^2\sin\phi\cos\phi - \sin^2\phi}{p}\frac{\partial}{\partial p} \\
&\quad +\frac{\mu^2(1-\mu^2)\sin\phi\cos\phi}{p^2}\frac{\partial^2}{\partial\mu^2} + \frac{3\mu(1-\mu^2)\sin\phi\cos\phi}{p^2}\frac{\partial}{\partial\mu} \\
&\quad -\frac{\sin\phi\cos\phi}{p^2(1-\mu^2)}\frac{\partial^2}{\partial\phi^2} + \frac{\sin^2\phi-\cos^2\phi}{p^2(1-\mu^2)}\frac{\partial}{\partial\phi} \\
&\quad -\frac{2\mu(1-\mu^2)\sin\phi\cos\phi}{p}\frac{\partial^2}{\partial\mu\partial p} + \frac{\mu(\sin^2\phi-\cos^2\phi)}{p^2}\frac{\partial^2}{\partial\phi\partial\mu} \\
&\quad -\frac{(\cos^2\phi-\sin^2\phi)}{p}\frac{\partial^2}{\partial\phi\partial p}. \qquad \text{(A.6)}
\end{aligned}$$

References

Ackermann, M., Ajello, M., Allafort, A., Baldini, L., Ballet, J., Barbiellini, G., Baring, M. G., and 162 coauthors (2013). Detection of the Characteristic Pion-Decay Signature in Supernova Remnants. *Science*, **339**, 807–811.

Armstrong, C. K. and Craig, I. J. D. (2013). Visco-Resistive Dissipation in Transient Reconnection Driven by the Orszag-Tang Vortex. *Solar Phys.*, **283**, 463–471.

Armstrong, C. K. and Craig, I. J. D. (2014). Visco-Resistive Dissipation in Strongly Driven Transient Reconnection. *Solar Phys.*, **289**, 869–877.

Armstrong, C. K., Craig, I. J. D., and Litvinenko, Y. E. (2011). Viscous effects in time-dependent planar reconnection. *Astron. Astrophys.*, **534**, A25.

Armstrong, C. K., Litvinenko, Y. E., and Craig, I. J. D. (2012). Modeling Focused Acceleration of Cosmic-Ray Particles by Stochastic Methods. *Astrophys. J.*, **757**, 165.

Artmann, S., Schlickeiser, R., Agueda, N., Krucker, S., and Lin, R. P. (2011). A diffusive description of the focused transport of solar energetic particles. Intensity- and anisotropy-time profiles as a powerful diagnostic tool for interplanetary particle transport conditions. *Astron. Astrophys.*, **535**, A92.

Asai, A., Yokoyama, T., Shimojo, M., and Shibata, K. (2004). Downflow Motions Associated with Impulsive Nonthermal Emissions Observed in the 2002 July 23 Solar Flare. *Astrophys. J. Lett.*, **605**, L77–L80.

Barnes, A. (1979). *Hydromagnetic waves and turbulence in the solar wind*, volume 1 of *Solar System Plasma Physics*, pages 249–319. North-Holland Publishing Co., Amsterdam.

Besser, B. P., Biernat, H. K., and Rijnbeek, R. P. (1990). Planar MHD stagnation-point flows with velocity shear. *Planet. Space Sci.*, **38**, 411–418.

Biskamp, D. (1986). Magnetic reconnection via current sheets. *Phys. Fluids*, **29**, 1520–1531.

Biskamp, D. (1993a). Current sheet profiles in two-dimensional magnetohydrodynamics. *Phys. Fluids B*, **5**, 3893–3896.

Biskamp, D. (1993b). *Nonlinear magnetohydrodynamics*. Cambridge Monographs on Plasma Physics. Cambridge University Press, Cambridge [England]; New York, NY.

Biskamp, D. (1994). Magnetic reconnection. *Phys. Rep.*, **237**, 179–247.

Biskamp, D. and Welter, H. (1980). Coalescence of magnetic islands. *Phys. Rev. Lett.*, **44**, 1069–1072.

Biskamp, D. and Welter, H. (1989). Dynamics of decaying two-dimensional magnetohydrodynamic turbulence. *Phys. Fluids B*, **1**, 1964–1979.

Biskamp, D., Schwarz, E., and Drake, J. F. (1995). Ion-controlled collisionless magnetic reconnection. *Phys. Rev. Lett.*, **75**, 3850–3853.

Blandford, R. and Eichler, D. (1987). Particle acceleration at astrophysical shocks: A theory of cosmic ray origin. *Phys. Rep.*, **154**, 1–75.

Braginskii, S. I. (1965). Transport Processes in a Plasma. *Rev. Plasma Phys.*, **1**, 205.

Burbidge, G. R. (1956). On Synchrotron Radiation from Messier 87. *Astrophys. J.*, **124**, 416.

Chandrasekhar, S. (1943). Stochastic Problems in Physics and Astronomy. *Rev. Modern Phys.*, **15**, 1–89.

Chew, G. F., Goldberger, M. L., and Low, F. E. (1956). The Boltzmann Equation and the One-Fluid Hydromagnetic Equations in the Absence of Particle Collisions. *Roy. Soc. London Proc. A*, **236**, 112–118.

Conway, A. J., MacKinnon, A. L., Brown, J. C., and McArthur, G. (1998). Analytic description of collisionally evolving fast electrons, and solar loop-top hard X-ray sources. *Astron. Astrophys.*, **331**, 1103–1107.

Courant, R., Friedrichs, K., and Lewy, H. (1928). Über die partiellen Differenzengleichungen der mathematischen Physik. *Math. Annalen*, **100**, 32–74.

Craig, I. J. D. (2008). Anisotropic viscous dissipation in compressible magnetic X-points. *Astron. Astrophys.*, **487**, 1155–1161.

Craig, I. J. D. (2010). Anisotropic viscous dissipation in transient reconnecting plasmas. *Astron. Astrophys.*, **515**, A96.

Craig, I. J. D. and Fabling, R. B. (1996). Exact Solutions for Steady State, Spine, and Fan Magnetic Reconnection. *Astrophys. J.*, **462**, 969.

Craig, I. J. D. and Henton, S. M. (1995). Exact Solutions for Steady State Incompressible Magnetic Reconnection. *Astrophys. J.*, **450**, 280.

Craig, I. J. D. and Litvinenko, Y. E. (2007). Wave Energy Dissipation by Anisotropic Viscosity in Magnetic X-Points. *Astrophys. J.*, **667**, 1235–1242.

Craig, I. J. D. and Litvinenko, Y. E. (2009). Anisotropic viscous dissipation in three-dimensional magnetic merging solutions. *Astron. Astrophys.*, **501**, 755–760.

Craig, I. J. D. and Litvinenko, Y. E. (2010). Energy Losses by Anisotropic Viscous Dissipation in Transient Magnetic Reconnection. *Astrophys. J.*, **725**, 886–893.

Craig, I. J. D. and Litvinenko, Y. E. (2012). Inflow Reconnection Solutions in Incompressible Visco-resistive Plasmas. *Astrophys. J.*, **747**, 16.

Craig, I. J. D. and Lopez, N. (2013). Viscous dissipation in 3D spine reconnection solutions. *Astron. Astrophys.*, **560**, A36.

Craig, I. J. D. and Watson, P. G. (1999). Dynamic Planar Magnetic Reconnection Solutions for Incompressible Plasmas. *Astrophys. J.*, **516**, 924–933.

Craig, I. J. D. and Watson, P. G. (2000). Optimized magnetic reconnection solutions in three dimensions. *Solar Phys.*, **194**, 251–268.

Craig, I. J. D., MacKinnon, A. L., and Vilmer, N. (1985). Solution of the electron continuity equation in an inhomogeneous medium via the method of characteristics. *Astrophys. Space Sci.*, **116**, 377–387.

Craig, I. J. D., Fabling, R. B., Henton, S. M., and Rickard, G. J. (1995). An Exact Solution for Steady State Magnetic Reconnection in Three Dimensions. *Astrophys. J. Lett.*, **455**, L197.

Craig, I. J. D., Litvinenko, Y. E., and Senanayake, T. (2005). Viscous effects in planar magnetic X-point reconnection. *Astron. Astrophys.*, **433**, 1139–1143.

Dahlburg, R. B. and Picone, J. M. (1989). Evolution of the Orszag-Tang vortex system in a compressible medium. I - Initial average subsonic flow. *Phys. Fluids B*, **1**, 2153–2171.

DeLuca, E. E. and Craig, I. J. (1992). Magnetic reconnection in incompressible fluids. *Astrophys. J.*, **390**, 679–686.

Drake, J. F., Swisdak, M., and Fermo, R. (2013). The Power-law Spectra of Energetic Particles during Multi-island Magnetic Reconnection. *Astrophys. J. Lett.*, **763**, L5.

Dung, R. and Schlickeiser, R. (1990). The role of Alfvenic magnetic and cross helicity in solar cosmic ray transport. *Astron. Astrophys.*, **237**, 504–511.

Earl, J. A. (1974). The diffusive idealization of charged-particle transport in random magnetic fields. *Astrophys. J.*, **193**, 231–242.

Earl, J. A. (1976). The effect of adiabatic focusing upon charged-particle propagation in random magnetic fields. *Astrophys. J.*, **205**, 900–919.

Earl, J. A. (1992). Effect of magnetic helicity upon rectilinear propagation of charged particles in random magnetic fields. *Astrophys. J.*, **395**, 185–191.

Earl, J. A., Ruffolo, D., Pauls, H. L., and Bieber, J. W. (1995). Comparison of Three Numerical Treatments of Charged Particle Transport. *Astrophys. J.*, **454**, 749.

Einstein, A. (1905). Über die von der molekularkinetischen Theorie der Wärme geforderte Bewegung von in ruhenden Flüssigkeiten suspendierten Teilchen. *Annalen der Physik*, **322**, 549–560.

Fabling, R. B. and Craig, I. J. D. (1996). Exact solutions for steady-state, planar, magnetic reconnection in an incompressible viscous plasma. *Phys. Plasmas*, **3**, 2243–2247.

Fermi, E. (1949). On the Origin of the Cosmic Radiation. *Phys. Rev.*, **75**, 1169–1174.

Fletcher, L. and Martens, P. C. H. (1998). A Model for Hard X-Ray Emission from the Top of Flaring Loops. *Astrophys. J.*, **505**, 418–431.

Fokker, A. D. (1914). Die mittlere Energie rotierender elektrischer Dipole im Strahlungsfeld. *Annalen der Physik*, **348**, 810–820.

Friedrich, R., Peinke, J., and Renner, C. (2000). How to Quantify Deterministic and Random Influences on the Statistics of the Foreign Exchange Market. *Phys. Rev. Lett.*, **84**, 5224–5227.

Gardiner, C. W. (2004). *Handbook of stochastic methods for physics, chemistry and the natural sciences*, volume 13 of *Springer Series in Synergetics*. Springer-Verlag, Berlin, third edition.

Goudon, T. and Saad, M. (1998). On a fokker-planck equation arising in population dynamics. *Revista Matemtica Complutense*, **11**(2), 353–372.

Hassam, A. B. and Lambert, R. P. (1996). Shear Alfvenic Disturbances in the Vicinity of Magnetic Null X-Points. *Astrophys. J.*, **472**, 832.

Hasselmann, K. and Wibberenz, G. (1970). A Note on the Parallel Diffusion Coefficient. *Astrophys. J.*, **162**, 1049.

Heerikhuisen, J. and Craig, I. J. D. (2004). Magnetic Reconnection in Three Dimensions - Spine, Fan and Separator Solutions. *Solar Phys.*, **222**, 95–114.

Heerikhuisen, J., Craig, I. J. D., and Watson, P. G. (2000). Time-dependent magnetic reconnection in two-dimensional periodic geometry. *Geophys. Astrophys. Fluid Dyn.*, **93**, 115–142.

Heerikhuisen, J., Litvinenko, Y. E., and Craig, I. J. D. (2002). Proton Acceleration in Analytic Reconnecting Current Sheets. *Astrophys. J.*, **566**, 512–520.

Heyn, M. F. and Semenov, V. S. (1996). Rapid reconnection in compressible plasma. *Phys. Plasmas*, **3**, 2725–2741.

Higham., D. J. (2001). An algorithmic introduction to numerical simulation of stochastic differential equations. *SIAM Rev.*, **43**(3), 525–546.

Hollweg, J. V. (1985). Viscosity in a magnetized plasma - Physical interpretation. *J. Geophys. Res.*, **90**, 7620–7622.

Hollweg, J. V. (1986). Viscosity and the Chew-Goldberger-Low equations in the solar corona. *Astrophys. J.*, **306**, 730–739.

Holman, G. D., Sui, L., Schwartz, R. A., and Emslie, A. G. (2003). Electron Bremsstrahlung Hard X-Ray Spectra, Electron Distributions, and Energetics in the 2002 July 23 Solar Flare. *Astrophys. J. Lett.*, **595**, L97–L101.

Holman, G. D., Aschwanden, M. J., Aurass, H., Battaglia, M., Grigis, P. C., Kontar, E. P., Liu, W., Saint-Hilaire, P., and Zharkova, V. V. (2011). Implications of X-ray Observations for Electron Acceleration and Propagation in Solar Flares. *Space Sci. Rev.*, **159**, 107–166.

Hopf, E. and Wiener, N. (1932). *Über eine Klasse singulärer Integralgleichungen*. Sitzungsberichte der Preuß. Akademie der Wissenschaften.

Hosking, R. J. and Marinoff, G. M. (1973). Magneto-viscous effects on the ideal and resistive gravitational instabilities in Cartesian geometry. *J. Plasma Phys.*, **15**, 327–341.

Huba, J., of Naval Research, U. S. O., and (U.S.), N. R. L. (2009). *2009 NRL Plasma Formulary*. NRL publication. Naval Research Laboratory.

Isenberg, P. A. (1997). A hemispherical model of anisotropic interstellar pickup ions. *J. Geophys. Res.*, **102**, 4719–4724.

Itô, K. (1944). Stochastic integral. *Proc. Imp. Acad. Tokyo*, **20**, 519–524.

Itô, K. (1951). *On Stochastic Differential Equations*. American Mathematical Society. Memoirs Series. Books on Demand.

Jardine, M., Allen, H. R., Grundy, R. E., and Priest, E. R. (1992). A family of two-dimensional nonlinear solutions for magnetic field annihilation. *J. Geophys. Res.*, **97**, 4199–4207.

Jokipii, J. R. (1966). Cosmic-Ray Propagation. I. Charged Particles in a Random Magnetic Field. *Astrophys. J.*, **146**, 480.

Kallenrode, M. (2004). *Space Physics: An Introduction to Plasmas and Particles in the Heliosphere and Magnetospheres*. Advanced Texts in Physics. Springer.

Kappenman, J. G. (2004). Historically Large Geomagnetic Storms and Potential Electric Power Grid Impacts. *AGU Spring Meeting Abstracts*, page B2.

Kennel, C. F. and Engelmann, F. (1966). Velocity Space Diffusion from Weak Plasma Turbulence in a Magnetic Field. *Phys. Fluids*, **9**, 2377–2388.

Knoll, D. A. and Chacón, L. (2006). Coalescence of Magnetic Islands in the Low-Resistivity, Hall-MHD Regime. *Phys. Rev. Lett.*, **96**(13), 135001.

Kowal, G., Lazarian, A., Vishniac, E. T., and Otmianowska-Mazur, K. (2009). Numerical Tests of Fast Reconnection in Weakly Stochastic Magnetic Fields. *Astrophys. J.*, **700**, 63–85.

Krucker, S., Battaglia, M., Cargill, P. J., Fletcher, L., Hudson, H. S., MacKinnon, A. L., Masuda, S., Sui, L., Tomczak, M., Veronig, A. L., Vlahos, L., and White, S. M. (2008). Hard X-ray emission from the solar corona. *Astron. Astrophys. Rev.*, **16**, 155–208.

Landau, L. D. (1946). On the vibrations of the electronic plasma. *J. Phys. USSR*, **10**, 25.

Lemons, D. S. (2002). *An Introduction to Stochastic Processes in Physics*. The Johns Hopkins University Press, Baltimore, MD.

Li, H., Wang, C., and Richardson, J. D. (2008). Properties of the termination shock observed by Voyager 2. *Geophys. Res. Lett.*, **35**, 19107.

Lifshitz, E. M. and Pitaevskii, L. P. (1981). *Physical kinetics*. Course of theoretical physics. Pergamon Press, Oxford [England].

Lin, R. P., Mewaldt, R. A., and Van Hollebeke, M. A. I. (1982). The energy spectrum of 20 keV-20 MeV electrons accelerated in large solar flares. *Astrophys. J.*, **253**, 949–962.

Litvinenko, Y. E. (2005). Viscous Energy Dissipation by Flux Pile-Up Merging in the Solar Corona. *Solar Phys.*, **229**, 203–212.

Litvinenko, Y. E. (2012a). Effects of Non-isotropic Scattering, Magnetic Helicity, and Adiabatic Focusing on Diffusive Transport of Solar Energetic Particles. *Astrophys. J.*, **752**, 16.

Litvinenko, Y. E. (2012b). The Parallel Diffusion Coefficient and Adiabatic Focusing of Cosmic-Ray Particles. *Astrophys. J.*, **745**, 62.

Litvinenko, Y. E. and Craig, I. J. D. (2000). Flare Energy Release by Flux Pile-up Magnetic Reconnection in a Turbulent Current Sheet. *Astrophys. J.*, **544**, 1101–1107.

Litvinenko, Y. E. and Craig, I. J. D. (2003). Robust Scalings in Compressible Flux Pile-Up Reconnection. *Solar Phys.*, **218**, 173–181.

Litvinenko, Y. E. and Schlickeiser, R. (2011). Focused Acceleration of Cosmic-ray Particles in Non-uniform Magnetic Fields. *Astrophys. J. Lett.*, **732**, L31.

Ljepojevic, N. N. and Burgess, A. (1990). Calculation of the electron velocity distribution function in a plasma slab with large temperature and density gradients. *Roy. Soc. London Proc. A*, **428**, 71–111.

Luhmann, J. G. (1976). A quasi-linear kinetic equation for cosmic rays in the interplanetary medium. *J. Geophys. Res.*, **81**, 2089–2093.

MacKinnon, A. L. and Craig, I. J. D. (1991). Stochastic simulation of fast particle diffusive transport. *Astron. Astrophys.*, **251**, 693–699.

Masuda, S., Kosugi, T., Hara, H., Sakao, T., Shibata, K., and Tsuneta, S. (1995). Hard X-Ray Sources and the Primary Energy-Release Site in Solar Flares. *Pub. Astron. Soc. Japan*, **47**, 677–689.

Matthaeus, W. H. and Goldstein, M. L. (1982). Measurement of the rugged invariants of magnetohydrodynamic turbulence in the solar wind. *J. Geophys. Res.*, **87**, 6011–6028.

McKenzie, D. E. (2000). Supra-arcade Downflows in Long-Duration Solar Flare Events. *Solar Phys.*, **195**, 381–399.

McKenzie, D. E. and Hudson, H. S. (1999). X-Ray Observations of Motions and Structure above a Solar Flare Arcade. *Astrophys. J. Lett.*, **519**, L93–L96.

Miller, J. A., Cargill, P. J., Emslie, A. G., Holman, G. D., Dennis, B. R., LaRosa, T. N., Winglee, R. M., Benka, S. G., and Tsuneta, S. (1997). Critical issues for understanding particle acceleration in impulsive solar flares. *J. Geophys. Res.*, **102**, 14631–14660.

NASA (2013a). NASA Solar and heliospheric observatory (SOHO) homepage. `http://sohowww.nascom.nasa.gov/`. [Online; accessed 29-May-2013].

NASA (2013b). NASA Sun fact sheet. `http://nssdc.gsfc.nasa.gov/planetary/factsheet/sunfact.html`. [Online; accessed 3-Oct-2013].

Olver, F., Lozier, D., Boisvert, R., and Clark, C. (2010). *NIST Handbook of Mathematical Functions*. Cambridge University Press.

Orszag, S. A. and Tang, C.-M. (1979). Small-scale structure of two-dimensional magnetohydrodynamic turbulence. *J. Fluid Mech.*, **90**, 129–143.

Parashar, T. N., Shay, M. A., Cassak, P. A., and Matthaeus, W. H. (2009). Kinetic dissipation and anisotropic heating in a turbulent collisionless plasma. *Phys. Plasmas*, **16**(3), 032310.

Park, W., Monticello, D. A., and White, R. B. (1984). Reconnection rates of magnetic fields including the effects of viscosity. *Phys. Fluids*, **27**, 137–149.

Parker, E. N. (1957). Sweet's Mechanism for Merging Magnetic Fields in Conducting Fluids. *J. Geophys. Res.*, **62**, 509–520.

Parker, E. N. (1958). Dynamics of the Interplanetary Gas and Magnetic Fields. *Astrophys. J.*, **128**, 664.

Parker, E. N. (1963). The Solar-Flare Phenomenon and the Theory of Reconnection and Annihiliation of Magnetic Fields. *Astrophys. J. Supp. Ser.*, **8**, 177.

Parker, E. N. (1996). The alternative paradigm for magnetospheric physics. *J. Geophys. Res.*, **101**, 10587.

Petschek, H. E. (1964). Magnetic Field Annihilation. *NASA Spec. Pub.*, **50**, 425.

Pickel, J. C. and Blandford, Jr., J. T. (1980). Cosmic-ray-induced errors in MOS devices. *IEEE Transactions on Nuclear Science*, **27**, 1006–1015.

Priest, E. R. (1982). *Solar magneto-hydrodynamics*. D. Reidel Publishing Company, Dordrecht, Holland.

Priest, E. R. and Forbes, T. (2000). *Magnetic reconnection : MHD theory and applications*. Cambridge University Press, Cambridge [England]; New York, NY.

Reames, D. V. (1999). Particle acceleration at the Sun and in the heliosphere. *Space Sci. Rev.*, **90**, 413–491.

Rickard, G. J. and Craig, I. J. D. (1993). Fast magnetic reconnection and the coalescence instability. *Phys. Fluids B*, **5**, 956–964.

Roberts, P. H. (1967). *An Introduction to Magnetohydrodynamics*. Longmans.

Roelof, E. C. (1969). Propagation of Solar Cosmic Rays in the Interplanetary Magnetic Field. In H. Ögelman and J. R. Wayland, editors, *Lectures in High-Energy Astrophysics*, page 111.

Rosenbluth, M. N., MacDonald, W. M., and Judd, D. L. (1957). Fokker-Planck Equation for an Inverse-Square Force. *Phys. Rev.*, **107**, 1–6.

Ryu, D., Jones, T. W., and Frank, A. (1995). Numerical Magnetohydrodynamics in Astrophysics: Algorithm and Tests for Multidimensional Flow. *Astrophys. J.*, **452**, 785.

Schlickeiser, R. (1989). Cosmic-ray transport and acceleration. I - Derivation of the kinetic equation and application to cosmic rays in static cold media.

II - Cosmic rays in moving cold media with application to diffusive shock wave acceleration. *Astrophys. J.*, **336**, 243–293.

Schlickeiser, R. (2002). *Cosmic Ray Astrophysics*. Springer, Berlin.

Schlickeiser, R. (2009). First-Order Distributed Fermi Acceleration of Cosmic Ray Hadrons in Non-Uniform Magnetic Fields. *Mod. Phys. Lett. A*, **24**, 1461–1472.

Schlickeiser, R. (2011). A New Cosmic Ray Transport Theory in Partially Turbulent Space Plasmas: Extending the Quasilinear Approach. *Astrophys. J.*, **732**, 96.

Schlickeiser, R. and Jenko, F. (2010). Cosmic ray transport in non-uniform magnetic fields: consequences of gradient and curvature drifts. *J. Plasma Phys.*, **76**, 317–327.

Schlickeiser, R. and Shalchi, A. (2008). Cosmic-Ray Diffusion Approximation with Weak Adiabatic Focusing. *Astrophys. J.*, **686**, 292–302.

Schulman, L. (1996). *Techniques and Applications of Path Integration*. A Wiley interscience publication. Wiley.

Schwenn, R. (2006). Space Weather: The Solar Perspective. *Living Reviews in Solar Physics*, **3**, 2.

Shalchi, A., Koda, T. Å., Tautz, R. C., and Schlickeiser, R. (2009). Analytical description of nonlinear cosmic ray scattering: isotropic and quasilinear regimes of pitch-angle diffusion. *Astron. Astrophys.*, **507**, 589–597.

Smith, G. (1985). *Numerical Solution of Partial Differential Equations: Finite Difference Methods*. Oxford applied mathematics and computing science series. Clarendon Press.

Sofue, Y., Fujimoto, M., and Wielebinski, R. (1986). Global structure of magnetic fields in spiral galaxies. *Ann. Rev. Astron. Astrophys.*, **24**, 459–497.

Sonnerup, B. U. O. and Priest, E. R. (1975). Resistive MHD stagnation-point flows at a current sheet. *J. Plasma Phys.*, **14**, 283–294.

Spitzer, L. (1962). *Physics of Fully Ionized Gases*. Interscience Monograph Series. Wiley & Sons, New York, NY.

Stone, E. C., Cummings, A. C., McDonald, F. B., Heikkila, B. C., Lal, N., and Webber, W. R. (2008). An asymmetric solar wind termination shock. *Nature*, **454**, 71–74.

Strauss, R. D., Potgieter, M. S., Büsching, I., and Kopp, A. (2011). Modeling the Modulation of Galactic and Jovian Electrons by Stochastic Processes. *Astrophys. J.*, **735**, 83.

Sweet, P. A. (1958). The Neutral Point Theory of Solar Flares. In B. Lehnert, editor, *Electromagnetic Phenomena in Cosmical Physics*, volume 6 of *IAU Symposium*, page 123.

Titov, V. S. and Priest, E. R. (1997). Visco-resistive magnetic reconnection due to steady inertialess flows. Part 1. Exact analytical solutions. *J. Fluid Mech.*, **348**, 327–347.

Von Neumann, J. and Richtmyer, R. D. (1950). A Method for the Numerical Calculation of Hydrodynamic Shocks. *J. App. Phys.*, **21**, 232–237.

Wheatland, M. S. and Melrose, D. B. (1995). Interpreting YOHKOH hard and soft X-ray flare observations. *Solar Phys.*, **158**, 283–299.

Wood, P. and Neukirch, T. (2005). Electron Acceleration in Reconnecting Current Sheets. *Solar Phys.*, **226**, 73–95.

Woolfson, M. (2000). The origin and evolution of the solar system. *Astron. Geophys.*, **41**(1), 010000.

Zachary, A. L., Malagoli, A., and Colella, P. (1994). A higher-order godunov method for multidimensional ideal magnetohydrodynamics. *SIAM J. Sci. Stat. Comp.*, **15**(2), 263–284.

Zhang, M. (1999). A Markov Stochastic Process Theory of Cosmic-Ray Modulation. *Astrophys. J.*, **513**, 409–420.